Title

Magnetoresistive Devices for Biosensing Applications

Author

Huang, Chih-Cheng

Publication Date

2020

UNIVERSITY OF CALIFORNIA SAN DIEGO

Magnetoresistive Devices for Biosensing Applications

A dissertation submitted in partial satisfaction of the
requirements for the degree Doctor of Philosophy

in

Materials Science and Engineering

by

Chih-Cheng Huang

Committee in charge:

Professor Drew A. Hall, Chair
Professor Shadi A. Dayeh
Professor Eric E. Fullerton
Professor Darren J. Lipomi
Professor Yu-Hwa Lo

2020

The Dissertation of Chih-Cheng Huang is approved, and it is acceptable in quality and form for publication on microfilm and electronically:

Chair

University of California San Diego

2020

DEDICATION

To Zai-Li

Without your love and support, I cannot walk through this adventure.

I love you, dad.

TABLE OF CONTENTS

LIST OF FIGURES

LIST OF TABLES

ACKNOWLEDGEMENTS

Over my years at UCSD, I have received support and encouragement from a great number of individuals. I would like to first acknowledge my advisor, Professor Drew Hall, for providing me the opportunity to do research. It is Prof. Hall who guided me into this exciting magnetic research area with his sharp insight. He has not only offered numerous comments on my research but also helped me keep the research work toward the right track. His broad and deep knowledge has greatly impressed me, and his enthusiasm for research and optimistic charisma have been encouraging to me in the pursuance of my PhD degree. Prof. Hall is such a nice person that I can always get his advice and support not only on my research work but also on my personal issues. He has been a wonderful advisor to me. I am grateful to have had the opportunity to work with Prof. Hall on my PhD projects and sincerely appreciate all the guidance he gave me, academically and mentally.

I also owe many thanks to my partners in magnetic projects, especially Xiahan Zhou who has been working with me closely for the past five years and Matthew Chan who helped with signal processing. I would like to thank my fellow colleagues in the BioEE Group for their help, advice, and friendship. I would like to thank Da Ying, Dr. Haowei Jiang, Dr. Edwin Hsu, Dr. Alex Sun, Dr. Somok Mondal for their great friendship and immense assistance during the early years. I would also like to express my gratitude to group alumni and members, Dr. Venkatesh Alagarswamy, Chengyang Yao, Tianlei Sun, Tom Phelps, Corentin Pochet, Saurabh Kulkarni, Sandeep Adem, Sonal Jain, Omid Ghadami, Michael Sveiven, Enhan Mak, Aditi Jain, Dr. Saeromi Chung, and Dr. Naveen Kumar Singh for their help and support.

I would like to thank all my friends for making my time here so memorable – the hardship of pursuing a PhD can only be understood when one is involved in this cyclic journey. I would also like to thank someone I used to know, Juya: the road to PhD would not be initiated without your encouragement, and the light you left me will never quench.

Last, but absolutely not least, I would like to thank my parents for their endless support and unconditional love. Especially my father, Zai-Li, this dissertation is dedicated to you, hopefully you are doing well in Heaven. I love you.

Portions of this dissertation have been published previously as a result of several collaborations. I must again acknowledge each of the authors for their tremendous contributions.

Chapter 2, 3, and 4, are, in part, based on material from Chih-Cheng Huang, Xiahan Zhou, Da Ying, and Drew A. Hall, "A GMR-Based Magnetic Flow Cytometer Using Matched Filtering," in *Proceedings of IEEE Sensors 2017*, Glasgow, Scotland, Oct. 30 – Nov. 1, 2017; and a manuscript currently being prepared for submission for publication by Chih-Cheng Huang, Partha Ray, Matthew Chan, Xiahan Zhou, and Drew A. Hall. The dissertation author was the primary investigator and author of these papers.

Chapter 5 is a reprint of the material as it appears in *Scientific Reports* **7**, 45493 (2017), "Giant Magnetoresistive Biosensors for Time-Domain Magnetorelaxometry: A Theoretical Investigation and Progress Toward an Immunoassay," from Chih-Cheng Huang, Xiahan Zhou, and Drew A. Hall. The dissertation author was the primary investigator and author of these papers.

Chih-Cheng Huang

La Jolla, CA

June 2020

VITA

EDUCATION

2010	Bachelor of Science in Materials Science and Engineering, National Taiwan University, Taipei, Taiwan
2012	Master of Science in NanoEngineering and MicroSystems, National Tsing Hua University, Hsinchu, Taiwan
2020	Doctor of Philosophy in Materials Science and Engineering, University of California San Diego, La Jolla, USA

PUBLICATIONS

Chih-Cheng Huang, P. Ray, M. Chan, X. Zhou, and D.A. Hall, “An Aptamer-based Magnetic Flow Cytometer using Matched Filtering,” *Biosensors and Bioelectronics*, submitted.

Haowei Jiang, **C-C. Huang**, M. Chan and D. A. Hall, " A 2-in-1 Temperature and Humidity Sensor with a Single FLL Wheatstone-Bridge Front-End," *IEEE Journal of Solid-State Circuits (JSSC)*, in press.

Haowei Jiang, **C-C. Huang**, M. Chan and D. A. Hall, "A 2-in-1 Temperature and Humidity Sensor Achieving 62 fJ·K^2 and 0.83 pJ·(%RH)^2," *2019 IEEE Custom Integrated Circuits Conference (CICC)*, Austin, TX, USA, 2019.

Xiahan Zhou, **C-C. Huang**, and D.A. Hall, “Giant Magnetoresistive Biosensor Array for Detecting Magnetorelaxation,” *IEEE Transaction on Biomedical Circuits and Systems* **11**(4), 755 – 764.

Chih-Cheng Huang, X. Zhou, D. Ying, and D.A. Hall, "A GMR-Based Magnetic Flow Cytometer Using Matched Filtering," *Proceedings of IEEE Sensors 2017*, Glasgow, Scotland, Oct. 30 – Nov. 1, 2017.

Xiahan Zhou, **C-C. Huang**, and D.A. Hall, "Magnetoresistive Biosensors for Quantitative Proteomics," *Proceedings of SPIE Optics + Photonics*, San Diego, CA, Aug. 6-10, 2017.

Chih-Cheng Huang, X. Zhou, and D.A. Hall, "Giant Magnetoresistive Biosensors for Time-Domain Magnetorelaxometry: A Theoretical Investigation and Progress Toward an Immunoassay," *Scientific Reports* **7**, 45493 (2017).

ABSTRACT OF THE DISSERTATION

Magnetoresistive Devices for Biosensing Applications

by

Chih-Cheng Huang

Doctor of Philosophy in Materials Science and Engineering

University of California San Diego, 2020

Professor Drew A. Hall, Chair

Facing unprecedented population-ageing, noncommunicable diseases (NCDs) have become the primary risk of death. According to the World Health Organization (WHO), more than 80% of deaths are caused by NCDs in countries where at least 20% of

the population is over 60 years old. Inevitably, the growing impact of NCDs necessitates changes to the contemporary healthcare system that was designed many decades ago. One of the key factors of NCD management is to transition diagnostics from centralized laboratories closer to the patient in point-of-care (PoC) settings. PoC settings provide high effectiveness, low cost, easy access, and fast turnaround, PoC diagnostics exhibits timely detection and treatment monitoring of cancers where early detection has a huge impact on the treatment outcome and survival rate while simultaneously reducing the economic burden. Optical-based instrumentation is still the workhorse in clinical diagnostics, however, such instrumentation requires complex optics, lasers, and photodetectors making it hard to translate to the PoC. To address cancerous detection for NCD control, a magnetic biosensor provides an alternative platform for PoC-friendly settings like rapid turnaround time and miniaturization without the loss of sensitivity.

In this dissertation, magneto-biosensing techniques for cellular and molecular assays are presented. We developed a magnetic flow cytometer (MFC) using a giant magnetoresistive (GMR) biosensor and matched filtering to perform aptamer-based cellular assays. This work established the strategy of system design for dynamic throughputs and improved the accuracy to 95%. We extended the results to detect pancreatic cancer cells with over-expressed epidermal growth factor receptor (EGFR). The magnetic measurements were highly correlated with optical signal, revealing the future clinical potential. In terms of molecular detection, we implemented time-domain magnetorelaxometry (MRX) on GMR devices. An ultrafast electromagnet was designed to minimize the deadzone and allow the investigation of Néel relaxation. The effect of the applied magnetic field and magnetization time were explored to understand the relaxation process. The results showed excellent agreement with the empirical trend describing the relaxation based on natural-log behavior. We used these findings to optimize the system and perform a proof-of-principle magnetic immunoassay, the first time that GMR sensors have been reported for an MRX bioassay.

Chapter 1. INTRODUCTION

1.1 Transformation of Healthcare

Dramatic improvements in medicine and the healthcare system over the past century have increased the average life expectancy worldwide as a result of better understanding of disease processes, new treatments, and advances in pharmaceuticals. However, most healthcare systems globally are a sick-care system which was designed in the post-World War 2 era[1]. The sick-care system was not designed to prevent disease but instead to diagnose and treat illness, hence the reactive action only after a patient becomes sick. The reactive approach is expensive and ineffective to meet the needs of the contemporary healthcare system, especially the management of noncommunicable diseases (NCDs), which have become the primary risk of death with unprecedented population-ageing[2]. As a result, transformation of healthcare can be summarized with five major shifts (Figure 1.1) from: 1) reactive care to proactive care, 2) one-size-fits-all to personalized care, 3) institution-centered healthcare to decentralized healthcare, 4) paternalistic to patient empowerment, and 5) volume-based healthcare to value-based healthcare.

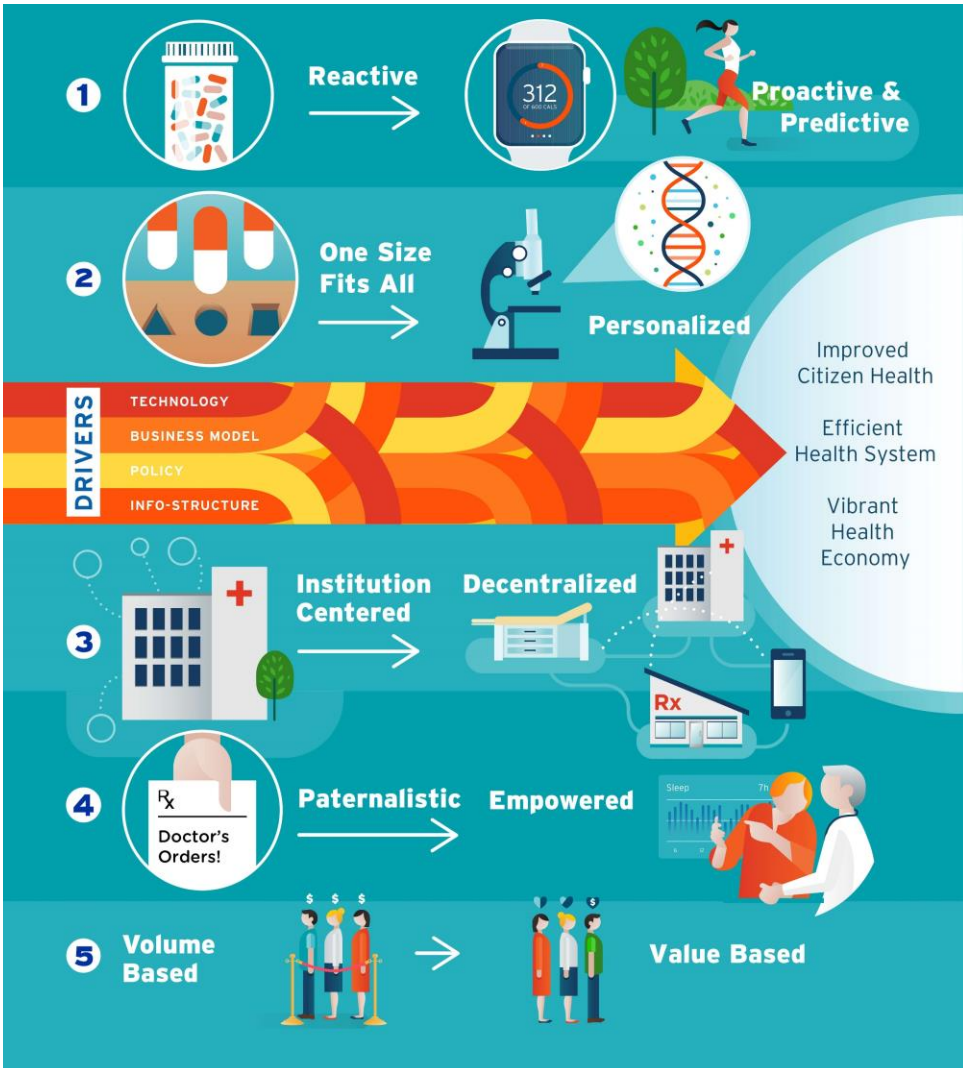

Figure 1.1 Illustration of transforming healthcare from Ref. 1

To address the need during the transformation, one of the enablers is the global deployment of point-of-care (PoC) detection that can improve disease management while reducing cost and increasing accessibility. PoC technologies have the potential to improve the management of various diseases and conditions, especially in resource-limited settings where healthcare infrastructure is weak and access to quality and timely medical care is a challenge. These tests offer rapid results, allowing for timely initiation of appropriate therapy and/or facilitation of linkages to care and referral. Most importantly, PoC devices can be simple enough to be used at the primary care level and in remote settings with no laboratory infrastructure.

1.2 Magnetoresistive Biosensors

Many technologies have improved the feasibility of PoC testing using optical biosensors[3,4], field effect transistor (FET)-based biosensors[5–7], electrochemical biosensors[8–10], and magnetic biosensors[11–17], amongst many others. Optical-based instrumentation is still the workhorse in clinical diagnostics where techniques such as fluorescence-activated cell sorting (FACS) and enzyme-linked-immunosorbent assays (ELISA) that offer multi-parameter and quantitative analysis for cellular and molecular analysis, respectively. However, such instrumentation requires complex optics, lasers, and photodetectors making it hard to translate to the PoC. Complementary metal-oxide-semiconductor (CMOS)-based optical biosensors have integrated the necessary components into portable formats[4,18,19]; however, the devices still fall short of the PoC promise due to the need for extensive sample pretreatment and bulky optics that require sophisticated operation and long turn-around.

For the past two decades, magnetic biosensors have received considerable attention as they offer several key advantages, *e.g.*, fast turn-around, ease of pre-treatment, matrix-insensitivity, and portability, over conventional and competing sensing methods[20–34]. Like an ELISA, a magnetic immunoassay (MIA) relies on two antibodies that form a sandwich structure around the biomarker of interest to achieve high specificity. However, the optical label in an ELISA is replaced with a 10 – 50 nm magnetic nanoparticle (MNP) in the MIA. This switch of label has been shown to retain sensitivity in unprocessed samples due to the lack of magnetic background signal[22], reduces the need for tedious sample preparation[35], allows for sample manipulation with magnetic fields[36,37], and enables real-time monitoring of the binding kinetics[23].

Early work developing magnetic biosensors can be traced back to 1990's, and since then researchers have demonstrated biosensing using a host of different magnetic sensors ranging from superconducting quantum interference device (SQUIDs)[38], inductive sensors[39], hall effect[36,37], flux-gate magnetometers[40], to magnetoresistive (MR)-based sensors[31,41–43]. Among the many magnetic sensors available today, MR-based devices standout for PoC applications. In addition to the inherent advantages of magnetic biosensing, MR biosensors can be operated at room temperature, have high low-field sensitivity, and have comparably high transduction efficiency. To address the need for NCD management and PoC deployment, the application of MR biosensors can be considered in two aspects: cellular diagnostics and molecular diagnostics.

1.3 Cellular Diagnostics using Magnetoresistive Biosensors

For cellular detection, MR-based magnetic flow cytometers (MFCs) have evolved over several decades[11,15,35,44–50]. To enable high throughput applications, most MFC works exploited high area-ratio microfluidics ($\frac{Cross-sectional\ Area_{\mu fludics}}{Surface\ Area_{sensor}} > 10$) to facilitate detection and accommodate a large amount of sample[35,44,48,49,51–54]. While the magnetic signal relies on the proximity sensing that is inversely proportional to the distance cubed between the MNP and the sensor[55]. As such, high area-ratio microfluidics would lose most signals when MNP-decorated analytes flow through. Some MFC works exploited magnetic chevrons[35,44,49] or electrical current lines[56] to guide the MNPs, which are close to the bottom of the channel, concentrated over the patterns and jetted successively to roll over the designated sensor area. This kind of design improved the detection efficiency when more analytes were coming onto the area, while it needed relatively slow linear flow to ensure the surficial contiguousness of MNP-decorated analytes. Furthermore, the system using magnetic guides not only limited the throughput but also brought about the issue of sample clogging (which is knottier). Another approach applied a strong field to magnetically attract MNP-decorated analytes down onto sensor surface, but the trajectory path made signal modelling hard to translate into multi-parametric information and only allowed a yes/no test. As a result, conventional MFCs barely take advantages of high throughput detection while maintaining the detection efficiency simultaneously, the significant loss of targets has hindered MFC from rare-cell detection *e.g.*, circulating tumor cells (CTCs). To address these concerns, the innovation of MFC must be developed to overcome the above challenges.

1.4 Molecular Diagnostics using Magnetoresistive Biosensors

Traditional MIA has gained a great success with excellent sensitivity and limit of detection (LOD) for molecular measurements[22,23,25,26]. A MIA conventionally relies on magnetometry to capture the tiny signal from the stray field among the strong baseline signal. However, this technique requires a homogeneous magnetic field, complex readout electronics, and substantial signal processing to extract the minute signal of interest, all of which are challenging to do in a power constrained, remote PoC environment. An alternative approach is based on magnetorelaxometry (MRX) where one detects the relaxation signature in response to a pulsed magnetic field. This technique removes the need for a homogenous magnetic field and requires comparably simpler readout electronics and signal processing. In the absence of an external magnetic field, the magnetic moment of the superparamagnetic MNPs tethered to the surface of the sensor are randomly oriented resulting in zero net field. Then, a magnetic field is applied that magnetizes and aligns all the MNPs. The stray field from the MNP opposes the applied field resulting in a small change in resistance in the underlying MR sensor. In MRX, the applied magnetic field is then switched off and the sensors monitored as the MNPs gradually relax to their equilibrium state. This relaxation signal can be either measured in the frequency- or time-domain. The frequency-domain technique uses a continuous AC magnetic field to measure the in-phase and out-of-phase component of the susceptibility whereas the time-domain technique measures the temporal response due to a pulsed magnetic field. In a PoC setting, the time-domain technique generally leads to a simpler implementation however requires careful understanding of the factors that influence the signal, which has limited progress in the past.

1.5 Scope of Dissertation

To address the mentioned challenges, this dissertation presents the developments and innovations of the MR biosensors for cellular measurement as well as molecular detection. In Chapter 2, magnetic modelling is presented to lay the foundation for mathematical simulation for both MFC and MRX. This establishes the design consideration of the experimental setup. In Chapter 3, the giant magnetoresistive (GMR)-based MFC is presented where the microfluidics and signal processing were co-optimized to improve the accuracy over previous MFC approaches. In Chapter 4, the established

MFC technique is expanded to detect aptamer-decorated cancer cells. Chapter 5 presents the progress toward immunoassay using time-domain MRX, with both the theoretical investigation and experimental considerations. Finally, Chapter 6 summarizes this work and remarks on future research directions.

Chapter 2. MAGNETIC MODELLING

This chapter is presented to calculate the magnetic field which is later taken account for the design consideration and signal modelling in our magnetic system. It begins with the GMR biochips used in our setup. The focus is then narrowed to the interaction between the magnetic nanoparticles and sensors using the Stoner–Wohlfarth model. Lastly, signal modelling is carried out with the both in-plane and out-of-plane field prior to the experimental design presented with the applications in MFC and MRX, respectively.

2.1 GMR Biochips

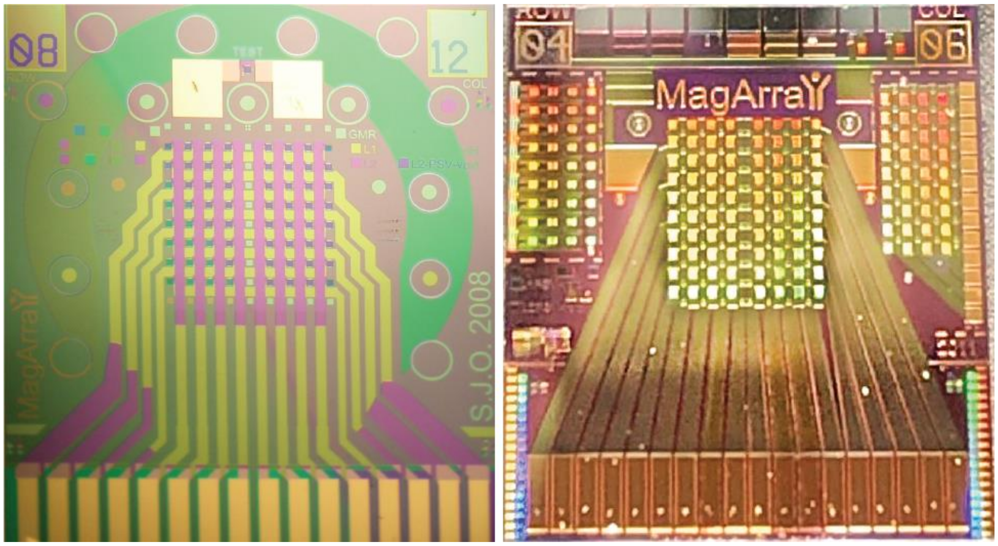

Figure 2.1 GMR biochips purchased from MagArray Inc.

The GMR biochips used throughout the dissertation were purchased from MagArray, Inc. The first (Figure 2.1, left) and second (Figure 2.1, right) generation versions of the GMR biochips used in this work have an 8×8 and 8×10 array of GMR sensors, respectively. Each GMR chip has 64 (or 80) individually addressable sensors arranged in a matrix with a nominal resistance (R_0) between 1450 – 1729 Ω and a magnetoresistance (MR) ratio of 8 – 11.5%, as measured and shown in Figure 2.2.

The GMR operation can be described by examining the two extreme cases: the parallel and anti-parallel states[57] of the free layer, as shown in Figure 2.3. In the antiparallel state, an electron in a different spin state will scatter when it travels through each ferromagnetic layer and the resistance increases. In contrast, in the parallel state, the electron in the same spin state passes through the first layer and the second layer with relatively few scattering events and thus has a lower path resistance because the spin of the electron is always in the same direction as the majority spin of the layers. For

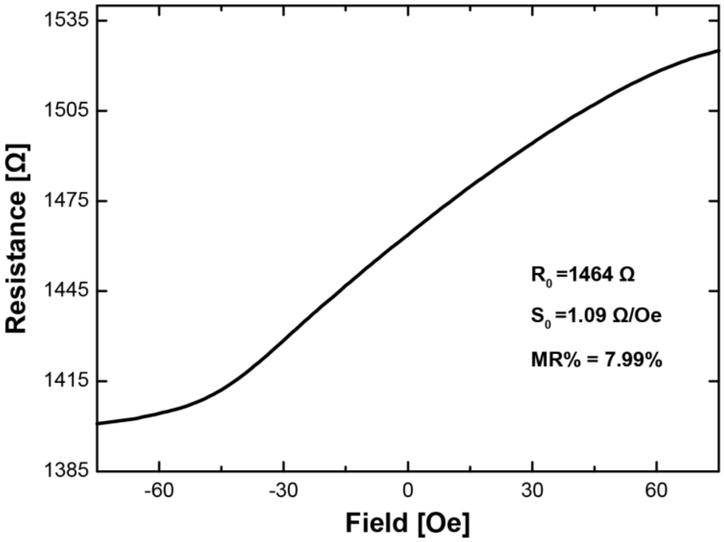

Figure 2.2 MR measurement of a GMR biochip

The tested GMR biochip owns the R_0 of 1464 Ω and a mean MR ratio of 7.99%.

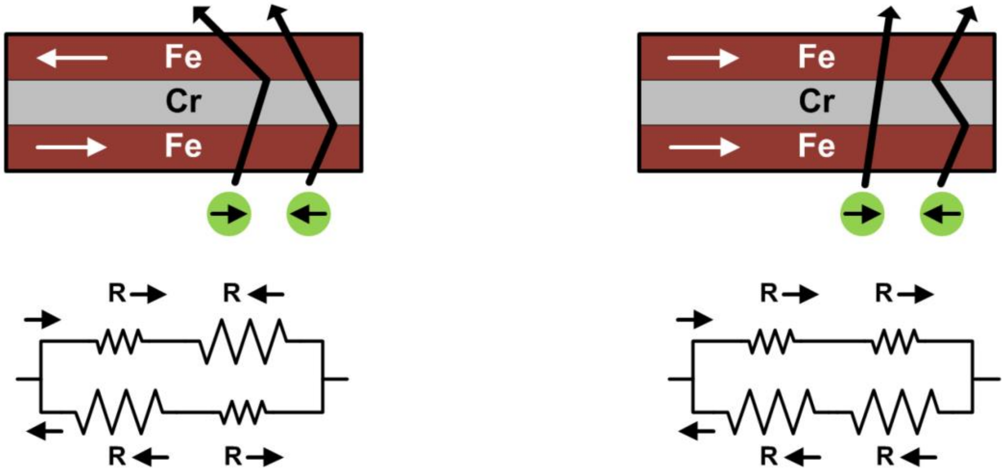

Figure 2.3 Operation of GMR devices from Ref. 57

biosensing, the GMR biochips were operated in the linear region around 50 Oe which is induced along the short axis in plane.

2.2 Stoner–Wohlfarth Model

The Stoner–Wohlfarth model was adopted for magnetic modelling[58]. MNPs are assumed to be Langevin spheres in the field, have a linear, superparamagnetic response, and give rise to dipole fields. It is assumed that the anisotropy of the free layer is strong enough to be stabilized during the measurement. We considered only the spatially averaged magnetic field emanated from a single MNP being magnetized by the applied field $\langle \boldsymbol{H_A} \rangle$. Thus, the average field that works on the free layer $\langle \overline{\boldsymbol{H_s}} \rangle$ is:

$$\overline{\boldsymbol{H_s}} = \frac{1}{l\cdot w\cdot th}\int_{\frac{-t}{2}}^{\frac{t}{2}}\int_{\frac{-w}{2}}^{\frac{w}{2}}\int_{\frac{-l}{2}}^{\frac{l}{2}}\frac{\chi {R_p}^3}{3}\cdot\left[\frac{3(\boldsymbol{H_A}\cdot\boldsymbol{r})\boldsymbol{r}}{r^5}-\frac{\boldsymbol{H_A}}{r^3}\right]dxdydz, \qquad 2.1$$

with

$$\boldsymbol{r} = (x - x_0, y - y_0, z - z_0), \qquad 2.2$$

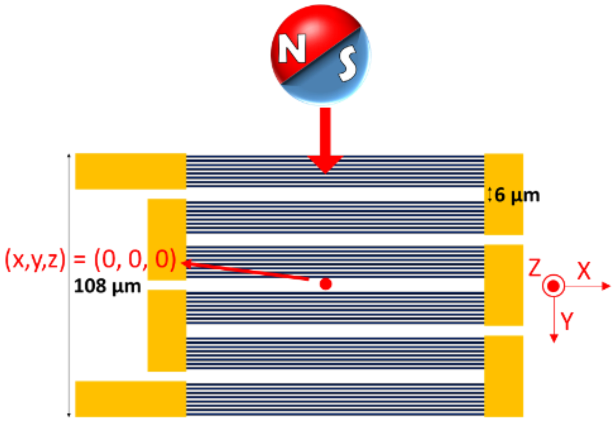

Figure 2.4 Sketch of system geometry when modelling signal

where l is the sensor length, w is the sensor width, th is the free layer thickness, χ is the volume susceptibility (dimensionless), R_p is the MNP radius, $\boldsymbol{r}$ is the distance between MNP (x_0, y_0, z_0) and the point of free layer (x, y, z), $\boldsymbol{x}$ and $\boldsymbol{y}$ are in-plane axes, and $\boldsymbol{z}$ is the out-of-plane axis, as Figure 2.4.

Two external field are considered, one applied along the in-plane axis and the other along the out-of-plane axis. Assuming that $\boldsymbol{H_A}$ points towards the $\boldsymbol{z}$ direction without divergence of the in-plane component (*i.e.* $\boldsymbol{H_A} = (0, 0, H_A)$) and the $\overline{\boldsymbol{H_s}}$ component along long-axis ($\boldsymbol{x}$) is neglected due to the insensitivity of long-axis field, the average field along the short-axis ($\boldsymbol{y}$) is the only component being considered:

$$\langle \boldsymbol{H_s} \rangle_{y,out} = \frac{\chi H_A {R_p}^3}{lwt} \int_{\frac{-t}{2}}^{\frac{t}{2}} \int_{\frac{-w}{2}}^{\frac{w}{2}} \int_{\frac{-l}{2}}^{\frac{l}{2}} \left[\frac{(y-y_0)(z-z_0)}{r^5} \right] dxdydz. \qquad 2.3$$

In the other case, $\boldsymbol{H_A} = (0, H_A, 0)$, and the resulting average field along its short axis is:

$$\langle \boldsymbol{H_s} \rangle_{y,in} = \frac{\chi H_A {R_p}^3}{3lwt} \int_{\frac{-t}{2}}^{\frac{t}{2}} \int_{\frac{-w}{2}}^{\frac{w}{2}} \int_{\frac{-l}{2}}^{\frac{l}{2}} \left[\frac{3(y-y_0)^2}{r^5} - \frac{1}{r^3} \right] dxdydz. \qquad 2.4$$

2.3 Magnetic Modelling for Magnetic Flow Cytometry

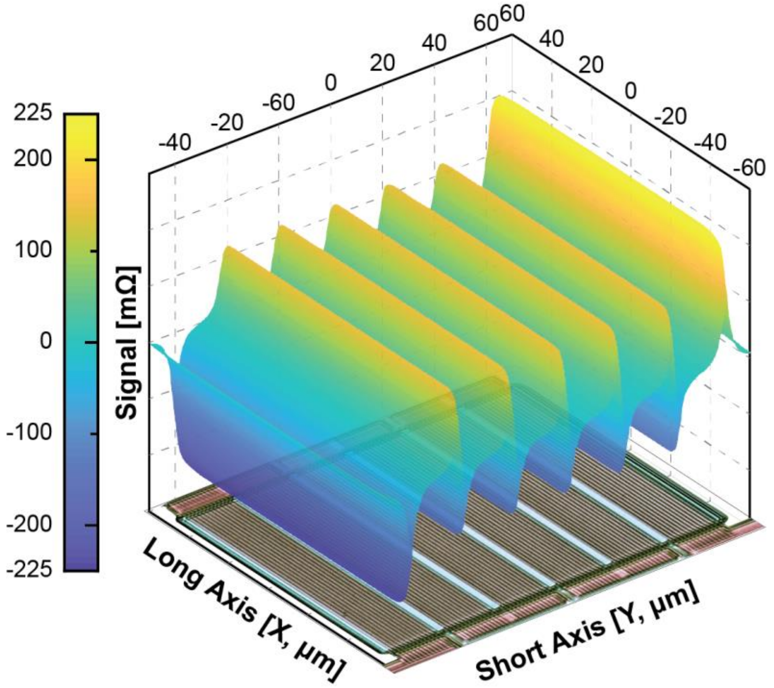

Figure 2.5 3D Simulation of MFC signal

To maximize the stray field and avoid saturating the GMR sensors, the out-of-plane field was applied for MFC. Prior to implementing the microfluidics and experimental setup, the signal simulation was conducted to optimize the MFC detection. Based on the average field exerted on a sensor (Eq. 2.3), the position-dependent signal can be simulated and illustrated in 3-D, as shown in Figure 2.5. The unique signature, generated from the multi-stripe layout, varies when using different MNPs. Here, we present the signature of the 4.5-µm magnetic beads (Dynabeads M-450, Invitrogen, #14011) located at the sensor surface that were simulated based on the model mentioned in the previous section. The profile of the MR signal (Figure 2.6) shows major dependence of $\boldsymbol{y}$-position, while it is rather insensitive to $\boldsymbol{x}$-position and the local maximum in amplitude occurs at the edge of each sensor unit (blue line). The multi-peak signature (bottom right subfigure in Figure 2.6) provides better resolution for signal processing and the ratio between inner-peak and

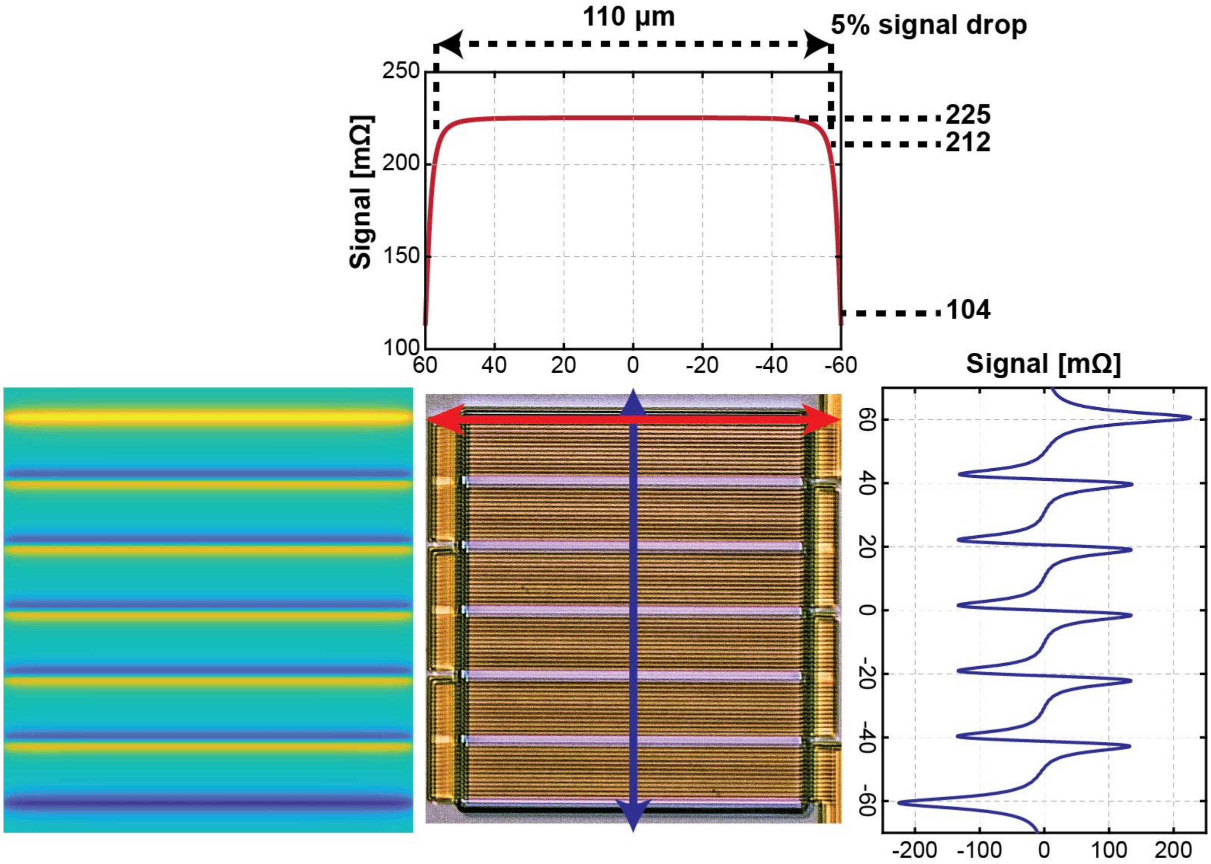

Figure 2.6 2D profile of positional dependence

edge-peak also changes when increasing the flow height. The x-profiling (red line with arrows) indicates that the signal only drops from 224 to 212 mΩ when moving from sensor center to x=±55 µm, *i.e.* 92% movement along x-axis gives rise to <5% signal variation. While the signal drops by up to 50% (from 212 to 104 mΩ) when moving from x=±55 µm to x=±60 µm (sensor edge along the long axis).

2.4 Magnetic Modelling for Magnetorelaxometry

Compared to MFC, which utilizes a static magnetic field to generate a stray field from the MNPs, magnetic modelling for MRX is relatively different due to the relaxation mechanism. Instead of monitoring a static field, MRX detects the decay in the magnetization of MNPs temporally. The relaxation mechanisms are based on the models proposed by Debye in 1929[59], Néel in 1950[60], and Brown[61] in 1963. After applying a magnetic pulse, the MNPs relax back to an equilibrium state by two mechanisms:

1) **Néel Relaxation:** The magnetization vectors of MNPs undergo internal rotation and gradually randomize to equilibrium. The Néel relaxation time (τ_N) can be described as:

$$\tau_N = \tau_0 \, exp\left(\frac{KV_c}{k_B T}\right), \qquad 2.5$$

where τ_0 is the attempt time (usually approximated as 10^{-9} sec), K is the MNP anisotropy constant, V_c is the MNP core volume, k_B is Boltzmann's constant, and T is the temperature in Kelvin.

2) **Brownian Relaxation:** The magnetization vectors of the MNPs undergo rigid rotation of the whole particle due to Brownian motion. The Brownian relaxation time (τ_B) can be described as:

$$\tau_B = \frac{3\eta V_h}{k_B T}, \qquad 2.6$$

where η is the dynamic viscosity of the liquid and V_h is the hydrodynamic volume of the MNP.

MRX can be measured in time-domain and frequency-domain. In the time-domain MRX, MNPs are magnetized and aligned with the external pulse of magnetic field, then gradually relax to the equilibrium state. The time-dependent magnetization can be described as[38,62,63]:

$$M_N(t) = M_0 \ln\left(1 + \frac{t_c}{t}\right), \qquad 2.7$$

and

$$M_B(t) = M_0 \exp\left(\frac{-t}{\tau_B}\right), \qquad 2.8$$

where M_N and M_B are the magnetization of the MNPs due to Néel relaxation and Brownian relaxation, respectively, M_0 is the magnetization of the MNPs at the time when turning off the external magnetic field, t is the time after turning off the field, and t_c is the characteristic time which depends on the magnetization time and external field.

In frequency-domain MRX, relaxation of MNPs can be measured by complex magnetic susceptibility with an alternating magnetic field. The frequency-dependent susceptibility can be described as[38,59,64,65]:

$$\chi_c(f) = \chi' - j\chi'' = \frac{\chi_0 - \chi_\infty}{1 + \left(\frac{jf}{f_B}\right)} + \chi_\infty, \qquad 2.9$$

where χ_c is the complex susceptibility, χ' is the in-phase susceptibility, χ'' is the out-of-phase susceptibility, χ_0 is the DC susceptibility, χ_∞ is the susceptibility at high frequency, $j \equiv \sqrt{-1}$, f is the frequency of the alternating magnetic field, and f_B is the Brownian frequency which is defined as:

$$f_B = \frac{1}{2\pi\tau_B}. \qquad 2.10$$

When MNPs are immobilized on the surface or dispersed in a freeze-dried solution, Brownian motion is inhibited. In contrast, Néel relaxation and Brownian relaxation simultaneously contribute to MRX when MNPs are freely dispersed in solution. The faster relaxation mechanism is dominant in MRX, thus the time-dependent magnetization can be described as:

$$M(t) = M_0 \exp\left(\frac{-t}{\tau_{eff}}\right), \tag{2.11}$$

where τ_{eff} is the effective relaxation time defined as:

$$\frac{1}{\tau_{eff}} = \frac{1}{\tau_B} + \frac{1}{\tau_N}. \tag{2.12}$$

To analyze MRX in magnetoresistive devices, we apply a current and measure the voltage variation due to the stray field generated by MNPs. Followed by Eq. 2.4, the average field from all the MNPs should be[66,67]:

$$\langle \boldsymbol{H_s} \rangle_{y,in,total} = \sum_{i=1}^{n} \langle \boldsymbol{H_s} \rangle_{y,in,i}. \tag{2.13}$$

In terms of signal output, we measured voltage change under constant applied current:

$$\Delta V_N = IS_0 H_{MNP}(t) = IS_0 H_0 \ln\left(1 + \frac{t_c}{t}\right), \tag{2.14}$$

$$\Delta V_B = I\Delta R = IS_0 H_{MNP}(t) = IS_0 H_0 \exp\left(\frac{-t}{\tau_B}\right), \tag{2.15}$$

and

$$H_0 = \left(\frac{\chi V_h}{4\pi z^3}\right) H_A, \tag{2.16}$$

where ΔV_N, ΔV_B are the signal (voltage variation) of the MNPs due to Néel relaxation and Brownian relaxation, respectively; I is the input current, S_0 is the sensitivity defined as $\partial R/\partial H$ (Ω/Oe), and H_0 is the stray field generated by MNPs at the time when turning off the external field. As a result, we expect to observe MRX signal by choosing the appropriate time window for specific MNPs.

Chapter 2, in part, is currently being prepared for submission for publication of the material from Chih-Cheng Huang, Partha Ray, Matthew Chan, Xiahan Zhou, and Drew A. Hall. The dissertation author was the primary investigator and author of these papers.

Chapter 3. A MAGNETIC FLOW CYTOMETER USING MATCHED FILTERING

3.1 Flow Cytometry

A flow cytometer (FCM) is an essential tool in hematology for quantitative analysis of cells with applications including identifying prognostic indicators for cancer, HIV, and other time-dependent biomarkers of disease activity[68–70]. Optical measurement techniques, such as forward scatter (FSC), side scatter (SSC), and fluorescence are currently considered the gold standard for multi-parametric analysis of heterogeneous cell populations[71]. However, such instrumentation requires complex optics, lasers, and photodetectors making it hard to translate to the PoC. Furthermore, optical FCMs require extensive sample preparation which involves cell lysis or matrix purification to properly detect cells/cell surface receptors (*e.g.*, CD4) from crude samples with a substantial optical background. As such, optical FCMs remain grounded in centralized laboratories with well-trained personnel resulting in long turnaround times and out of reach for routine monitoring by individuals or in office check-ups.

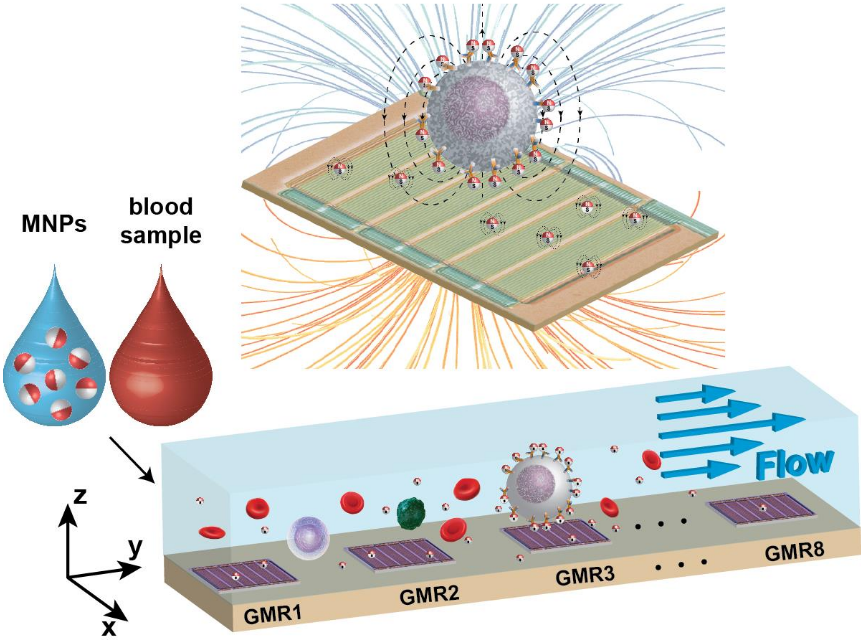

Figure 3.1 Schematic illustration of MFC

Operation of a GMR-based MFC where MNP-decorated analytes flow over GMR sensors and signals are activated by external field.

An alternative approach involves substituting the optical label with a magnetic tag and using a magnetic sensor instead of an optical detector[72]. This configuration has many benefits: 1) biological samples have no magnetic background eliminating problems such as photobleaching and auto-fluorescence commonly encountered in optical measurements, 2) the sample preparation can largely be eliminated, and 3) magnetic biosensors can be miniaturized, which also improves their sensitivity[73]. As such, magnetic FCMs have been of keen interest to the community for PoC measurements[35,45,48].

3.2 System Overview

In this chapter, a GMR-based MFC using matched filtering (MF) is presented to improve the signal-to-noise ratio (SNR) and allow detection of different types of magnetic labels, as shown in Figure 3.1. As the magnetic label flows over the sensor, a change in resistance is induced. The carefully designed sensor layout creates a characteristic signature from the MNPs, as shown in Figure 3.2, thus enabling multi-parametric labeling like optical FCMs. Furthermore, the array of sensors can extract the time-of-flight (ToF), which can be used as a proxy for the size and hydrodynamic volume of the cell and discussed in later section.

The measurement setup is shown in Figure 3.3 where a MFC was assembled with a GMR chip (MagArray, Inc.), a NdFeB permanent magnet, a microfluidic channel, and electrical readout. Each chip has 80 individually addressable sensors arranged in an 8×10 matrix, each sensor is 120×120 μm^2 with the R_0 of 1464 Ω and a mean MR ratio of 7.99% measured in Figure 2.2. The NdFeB permanent magnets (K&J Magnetics, Inc., #B881, B882, B882-N52, BCC2, BCC2-N52) were mounted horizontally below the sensor chip with out-of-plane field from 0.06 T to 0.13 T measured by a gaussmeter (Lake Shore Cryotronics, Inc., #475DSP).

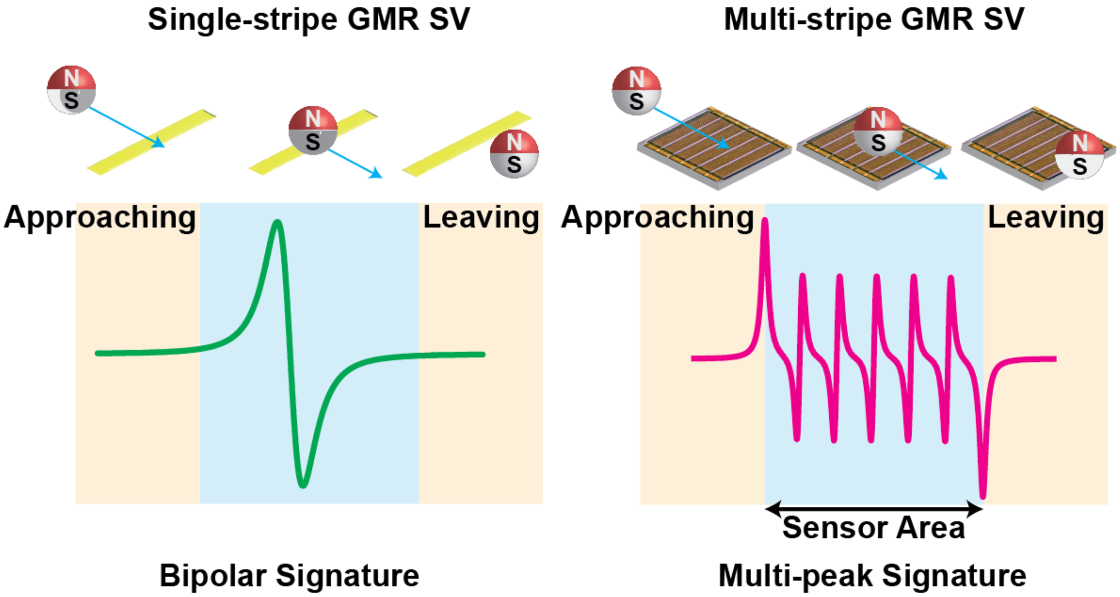

Figure 3.2 Layout-dependent signatures

Conventional single-stripe MFCs offer simple bipolar-peak readout which increases the false detections, while the multi-stripe configuration enhances the signal differentiation by unique magnetic signature.

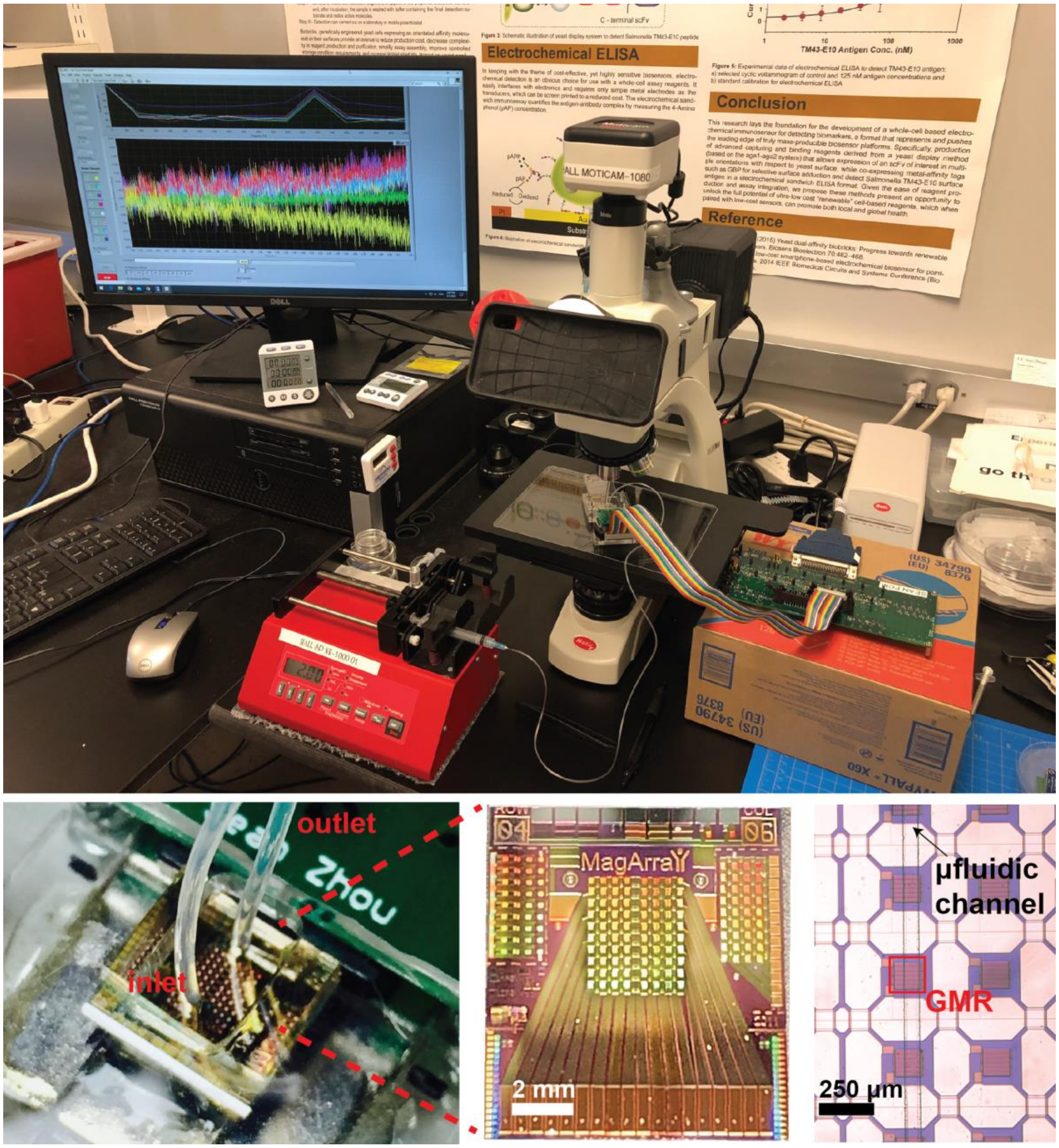

Figure 3.3 Testing bench of MFC

Photographs of the system (top) and zoomed-in view (from bottom left to right) of the sensor setup, a sensor chip, and the microfluidic channel. The desktop-based testing setup shows the MFC system and all components. Measurements were recorded through a custom written LabVIEW interface (as shown on PC screen).

Microfluidic channels were fabricated using a standard poly(dimethylsiloxane) (PDMS) process with SU-8 molding and PDMS curing with channel widths ranging from 90 to 120 µm and heights ranging from 14 to 40 µm. GMR chips were placed in a UV-ozone chamber (HELIOS-500, UVOTECH) for 15 minutes prior to bonding with the PDMS microfluidic channels. The microfluidic chips were subsequently aligned and cured for 1 hour at 75°C. The inlet and outlet of the PDMS channel were mechanically drilled and connected to a syringe pump (NE-300, New Era Pump Systems) with poly(tetrafluoroethylene) (PTFE) tubing.

3.3 Magnetic Nanoparticles and Polymer Microspheres

Superparamagnetic MNPs, Dynabeads M-450, Dynabeads M-280 (Invitrogen, #11205D), Bio-Adembeads (Ademtech, #03121), and SHS-30 (Ocean NanoTech, #SHS-30-01), were used in all experiments with hydrodynamic diameters of 4.5 µm, 2.8 µm, 200 nm, and 40 nm, respectively. Dynabeads M-450 and Dynabeads M-280 with a core particle size of 7.7 nm were washed 3× with 0.1× PBS before diluting to 1:400 and 1:650, respectively. A nonionic surfactant, Tween 20 (Sigma-Aldrich, #P1379), was added to the diluted Dynabeads solution at a dilution of 0.05%. Streptavidin-coated Bio-Adembeads and SHS-30 were centrifuged each time before the washing step (the same procedure as the Dynabeads); the final dilution ratios were 1:20 and 1:1, respectively.

Biotin-coated 10-µm polymer microspheres, ProActive CP10N (Bangs Laboratories, #CP10000), were conjugated with Bio-Adembeads to create a biomimetic construct used during algorithm development and evaluation. To build such construct, an aliquot of ProActive CP10N was washed with 10× volume of wash buffer (0.1× PBS + 0.05%Tween20, pH=7.4) three times. The pellet in the wash buffer was resuspended to 1:20 dilution. The diluted Bio-Adembeads (1:20) were added to this solution. The magnetic conjugates were formed and incubated at room temperature (18 – 25 °C) for 30 minutes with gentle mixing. The sample was resuspended in 20× volume of wash buffer prior to injecting into the microfluidic channel using a syringe pump (New Era Pump Systems, NE-1000).

3.4 Readout Circuitry and Signal Processing

The GMR sensors were read out using lock-in detection excited by a 1 V_{pp} sinusoidal source at 7 kHz generated by a data acquisition card (National Instruments, PCIe-6361), as shown in Figure 3.4. The resulting current was amplified by a transimpedance amplifier (TIA) implemented using an OpAmp (Analog Devices, AD8655) with resistive feedback (R_F=42.2 kΩ). A bleed resistor (R_B=1.5 kΩ) was used to cancel the

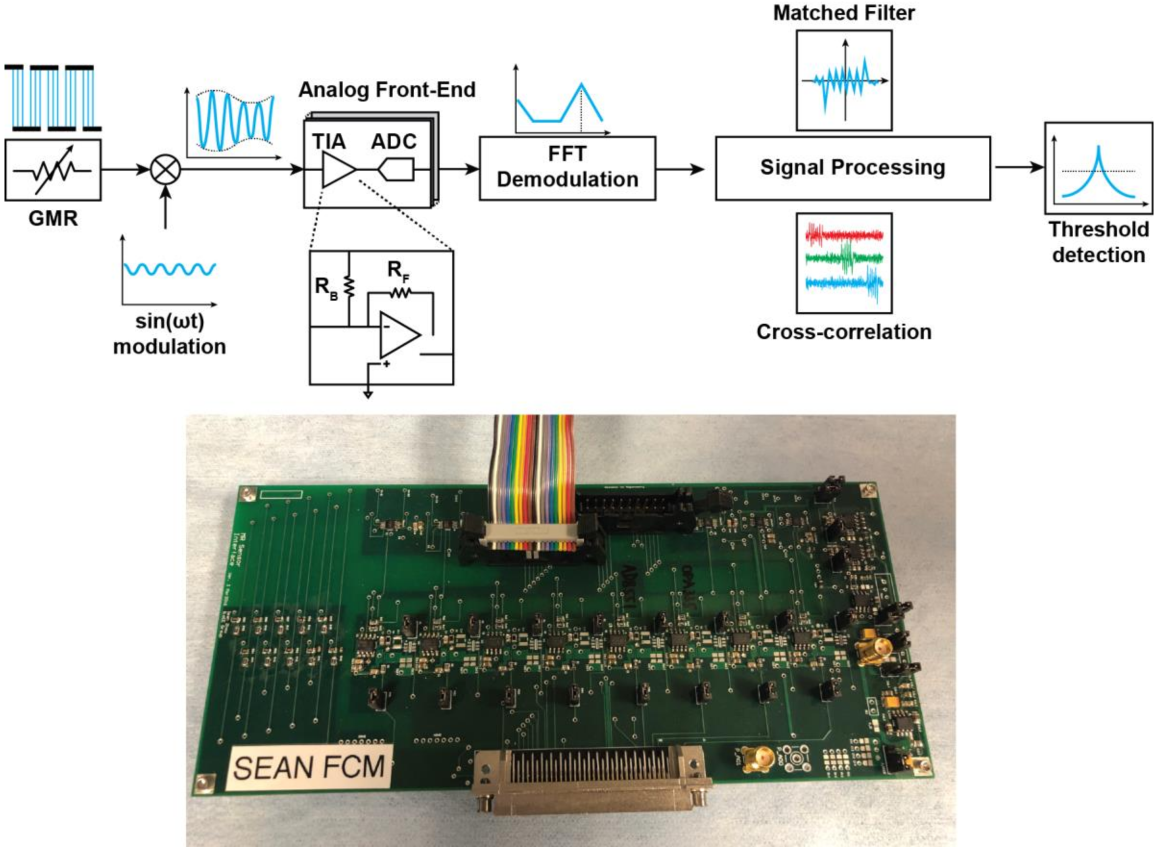

Figure 3.4 Block diagram of the electronics and photograph of the PCB

The GMR sensors are modulated by a sinusoidal voltage and the resulting currents are quantized by a TIA and an analog-to-digital converter (ADC). A R_B removes part of the sensor baseline current. Digital signal processing performs demodulation then applies MF and cross-sensor correlation to enables high SNR signal detection.

non-MR portion of the current and avoid saturating the TIA, thus enabling the gain to be increased by 28 dB. Eight parallel channels of this circuit were assembled on a custom printed circuit board (PCB). The TIA outputs were sampled at 125 kSps/ch. and processed in LabVIEW using a fast Fourier transform (FFT) to demodulate the signal (125-point FFT, 1 ms acquisition time). The input-referred noise of the system was measured to be 4.2 $m\Omega_{RMS}$ and spectrally white.

Cross-sensor correlation and MF were applied on the acquired data to calculate the ToF across the sensor array and improve the SNR, respectively. Cross-sensor correlation involves convolving a signal segment from a detected event with the signal measured on a subsequent sensor (*i.e.* using the signature observed on Sensor 1 and Sensor 2). The resulting signal is thresholded to find the delay between the two events and the ToF is calculated based on the known sensor-sensor spacing and time difference. MF convolves the measured signal with a template. Three different templates were evaluated with MF: simulation-based matched filters (SMF), energy-detection matched filters (EDMF), and previous-event matched filters (PEMF). The SMF utilizes Eq. 2.3 and other parameters, *e.g.* size of MNPs, velocity, number of MNPs, and vertical distance, to generate a library of templates. The EDMF template quantizes the expected signature into a tertiary square waveform. Lastly, the PEMF relies on the signature detected at a previous sensor. SMF and EDMF templates are illustrated in Figure 3.5, PEMF templates will be presented in Chapter 3.6. All signal processing was performed in MATLAB using custom written code. The implementation and efficacy of MFs will be discussed in Chapter 3.6.

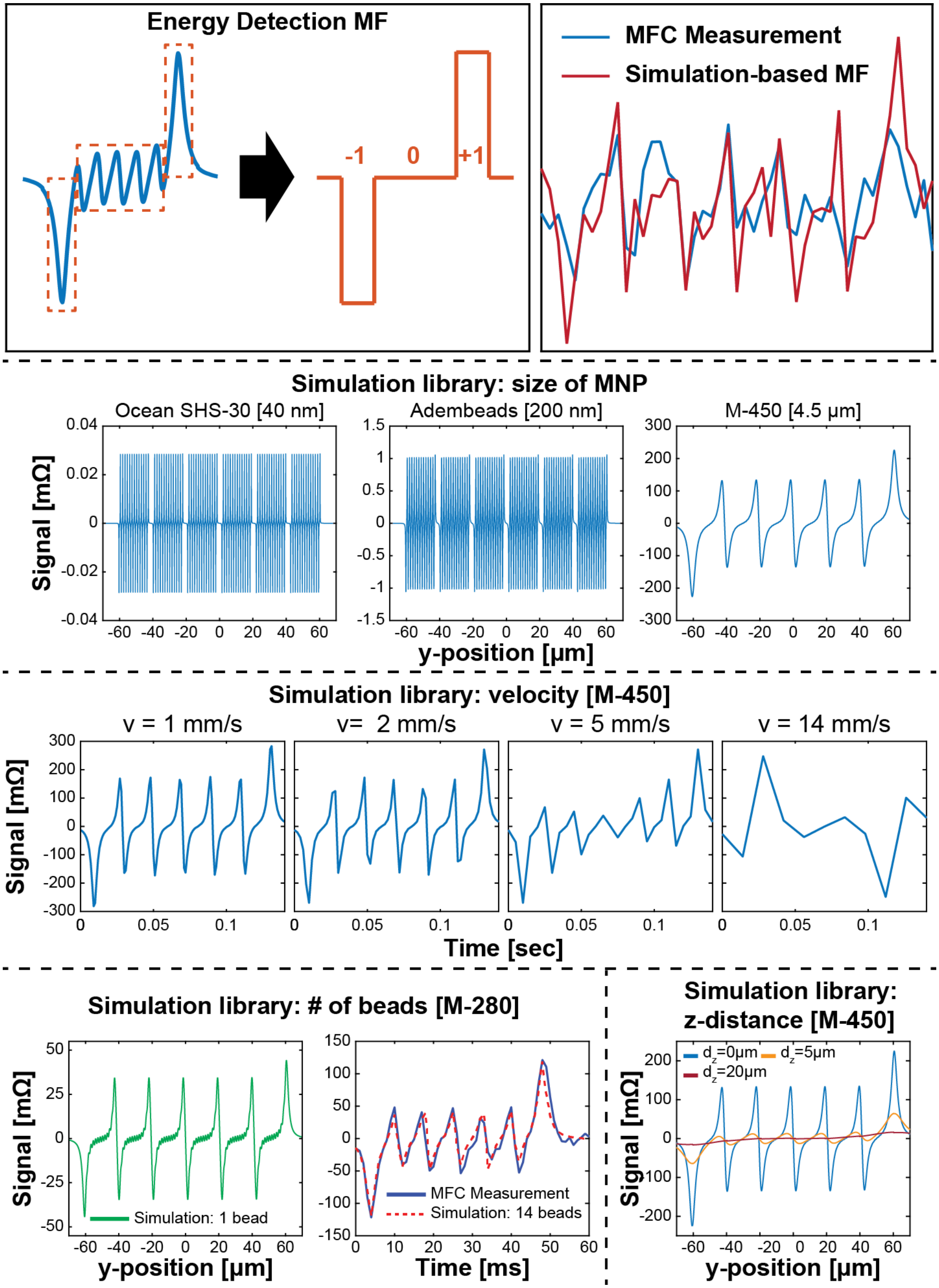

Figure 3.5 EDMF and SMF templates

3.5 Characteristics of Magnetic Flow Cytometry

Several limitations today restrict the portability of FCMs. First, conventional optical-based FCMs require extensive sample preparation, such as cell lysis and/or matrix purification to properly detect cells/cell surface receptors (*e.g.*, CD4, EpCAM) from crude samples due to the substantial optical background that the matrix presents[35,45]. Second, FCMs often use sheath fluid to center the analytes in the middle of the channel with laminar flow and hydrodynamic focusing. Lastly, the readout instrumentation requires complex optics, lasers, and photodetectors making it hard to directly translate to PoC settings. To enable PoC, sample-to-answer operation, we minimized the amount of sample preparation required without significantly affecting the throughput or sensitivity. We accomplished this objective using two techniques: 1) switching from an optical-based to a magnetic-based readout, and 2) co-optimizing the size of the sensor to remove the need for sheath fluid while generating a complex signature that enables advanced signal processing techniques to improve the SNR.

The background signal in a MFC is near zero as biological samples intrinsically lack magnetic material[22,23] thus removing the need for purification steps. Rather than using magnetic guides to focus the cells over a small sensor[35,44,72], we use the microfluidic channel to confine the cells over a much larger sensor. Using a large sensor negatively impacts the sensitivity, but, more importantly, ensures that the flowing analytes always travel across the active sensing area removing the need for sheath flow and minimizing false negative events. As will be described later, the larger sensor enables a complex signature to be generated rather than a simple bipolar peak, as shown in Figure 3.2.

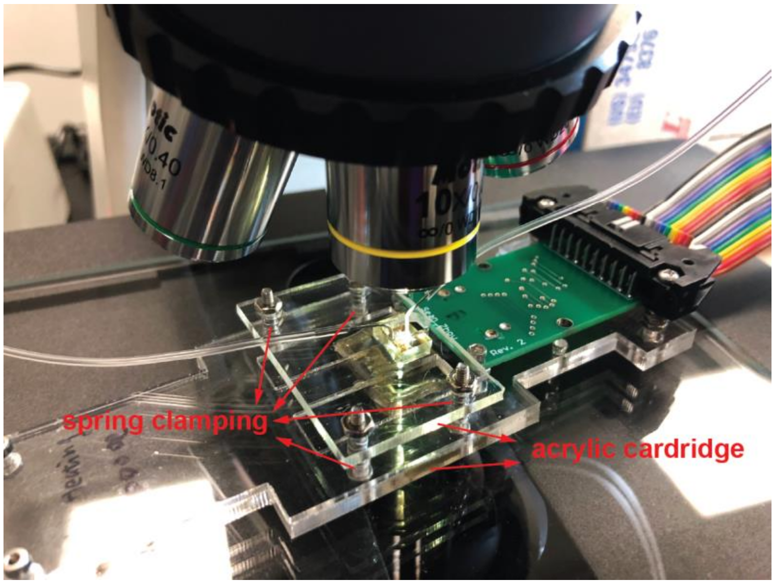

Figure 3.6 Holder showing spring-clamping

Acrylic plates with spring clamping enhance the sealing and prevent the system from leaking.

To enable high throughput detection in this relatively small channel (120 µm) compared with other MFCs[35,44,48–50], the seal between the sensor and the microfluidic channel needed to be improved to increase the flow rate and subsequently pressure. We achieved good sealing by applying UV-ozone treatment prior to bonding the sensor chip with the PDMS, post-curing to improve the contact, and spring-clamping to mechanically intensify the sealing while maintaining the sensor reusability, as shown in Figure 3.6. We performed hydrodynamic analysis for several different sized MNPs to determine the optimal flow rate and magnetic field strength to balance the MNP in the middle of the channel height. Many forces were considered, including the drag force, magnetic force, gravitation, DLVO forces, and Langevin force as shown in Figure 3.7. Drag force ($\boldsymbol{F_D}$) is the major contribution to MNP's movement in microfluidic channel among these forces, it is caused by the relative motion to the surrounding medium and can be expressed as:

$$\boldsymbol{F_D} = -6\pi\eta C_D R_p(\boldsymbol{v_p} - \boldsymbol{v_m}), \tag{3.1}$$

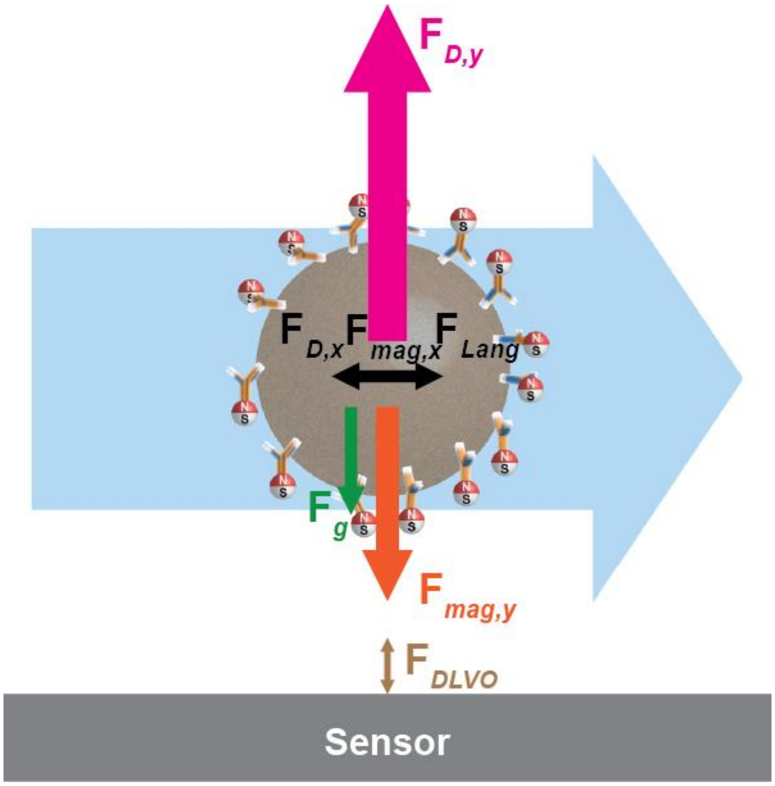

Figure 3.7 Illustration of forces acting on a MNP-labelled analyte

Pumping rate and corresponding flow velocity fast enough to keep drag force dominant over other forces.

where C_D is the drag coefficient defined by the size and shape of MNP, $\boldsymbol{v_p}$ is the MNP's velocity, and $\boldsymbol{v_m}$ is the medium velocity. Magnetic force ($\boldsymbol{F_M}$) is considered when a MNP is regarded as a magnetic dipole and locates in the applied static magnetic field:

$$\boldsymbol{F_M} = \frac{(\chi - \chi_m)V_p(\boldsymbol{B}\cdot\nabla\boldsymbol{B})}{\mu_0}, \tag{3.2}$$

where χ_m is the volume susceptibility of medium, V_p is the MNP's volume, and $\boldsymbol{B}$ is the magnetic flux density, and μ_0 is the permeability of free space. Gravity ($\boldsymbol{F_G}$) is considered with buoyancy:

$$\boldsymbol{F_G} = (\rho_p - \rho_m)V_p\boldsymbol{g}, \tag{3.3}$$

where ρ_p is the density of the MNP, ρ_m is the density of the medium, and $\boldsymbol{g}$ is the gravitational acceleration. Particle-particle and particle-substrate interaction can be described by Van der Waals force ($\boldsymbol{F_{VDW}}$), electro-repulsive force ($\boldsymbol{F_{el}}$) and Langevin force ($\boldsymbol{F_{lang}}$):

$$\boldsymbol{F_{VDW}} = -\frac{AR_p}{6d^2}, \tag{3.4}$$

$$\boldsymbol{F_{el}} = \frac{2\pi\varepsilon_0\varepsilon_r}{1-e^{-2\kappa d}}\left[2\psi_p\psi_s e^{-\lambda d} + \left({\psi_p}^2 + {\psi_s}^2\right)e^{-2\lambda d}\right], \tag{3.5}$$

$$\langle {\boldsymbol{F_{lang}}}^2(f)\rangle = 6\pi K_B T\eta C_D R_p, \tag{3.6}$$

where A is the Hamaker constant, d is the distance between the MNPs or between the MNP and the sensor substrate, ε_0 is the permittivity of free space, ε_r the relative permittivity, ψ_p is the surface potential of the MNP, ψ_s is the surface potential of the sensor substrate, λ is the Debye–Hückel length.

After careful analysis, it was determined that drag force is the major contributor to the MNP's movement in the microfluidic channel. A plot showing these forces as a function of MNP size is shown in Figure 3.8. The drag force is at least one order of magnitude larger than magnetic force for the largest MNP (M-450, 4.5 µm) with our pumping setup. When sub-micron-sized MNPs (Adembeads, 200 nm; Nanomag-D, 130 nm; and SHS-30, 40 nm) are considered, magnetic force becomes comparable to DLVO forces and Langevin force. Drag force was kept dominant over other forces to allow the sample to flow in the middle of the channel and thus extract multi-parametric information.

To evaluate and characterize the GMR-based MFC, we measured commercial MNPs with hydrodynamic sizes varying from 30 nm to 4.5 µm. The pumping rate for all

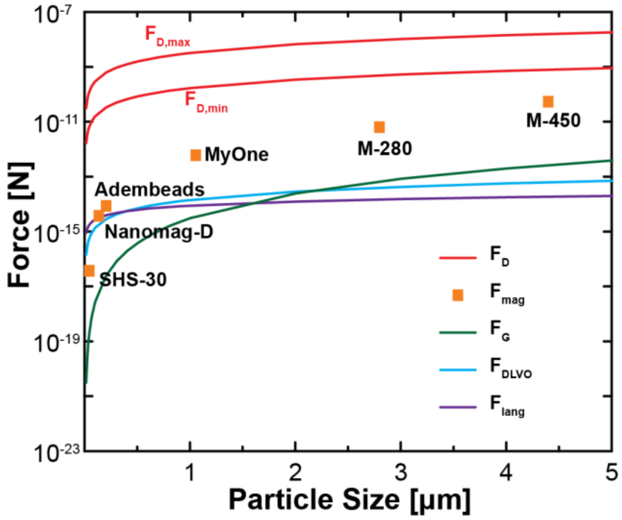

Figure 3.8 Hydrodynamic analysis

For sub-micron-sized MNPs (Adembeads, 200 nm; Nanomag-D, 130 nm; and SHS-30, 40 nm), the magnetic force is comparable to DLVO forces and Langevin force. While Drag force was kept dominant over other forces in the setup to allow samples flowing at middle of the channel and thus extract the multi-parametric information, as shown in the figure, drag force is at least one decade larger than magnetic force even flowing the largest MNP (M-450, 4.5 µm).

MNP was 10 µL/min through a 120×25 µm^2 channel. The smallest MNP, SHS-30, had no distinguishable signal (Figure 3.9a), as expected from simulation, due to its small magnetic moment and the strong particle-particle repulsion that prevents aggregation. While we did see occasional signatures from the other sub-micron MNP, Bio-Adembead, these were

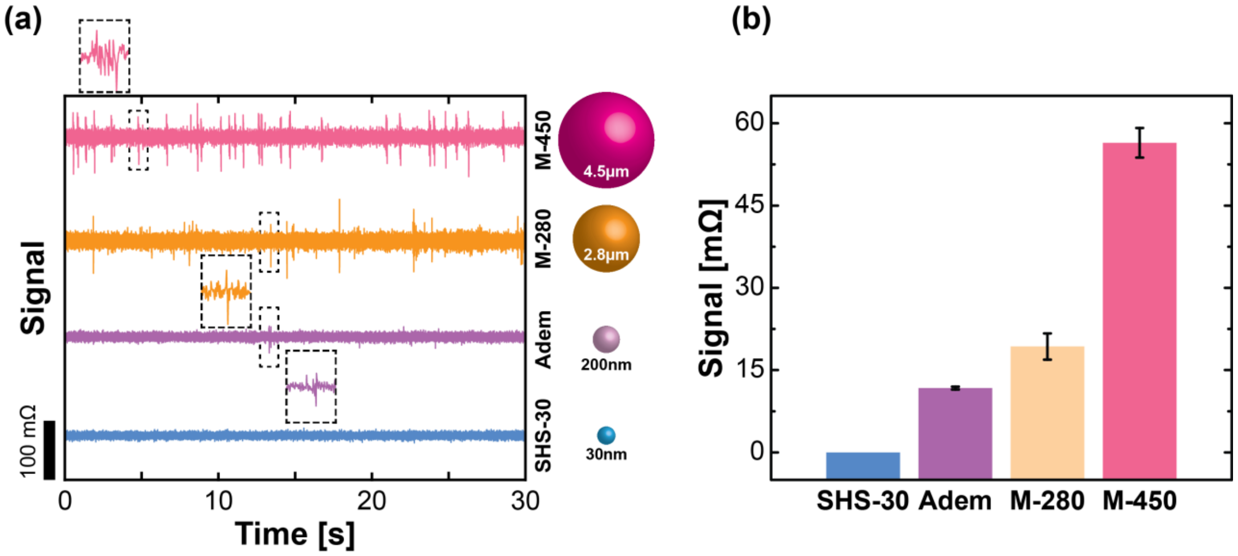

Figure 3.9 Bead-only assays

(a) Measurement of different MNPs and their magnetic signatures under the same flow rate. (b) Plot of measured signal amplitude vs. MNP size.

likely aggregates – not signal from individual particles. On the other hand, the M-280 and M-450 MNPs induced many signals. The velocity of the M-280 is faster (due to using the same pumping rate) and the signature degrades into a bipolar peak while the M-450 demonstrates the complete signature due to the slower velocity. It should be noted that the M-280 does show the full characteristic signature at slower pumping rates, but this pumping rate was chosen to allow all particles to use the same magnetic field for fair comparison. Figure 3.9b shows the average signal amplitude where an event is counted as anything larger than 5σ the noise level of a negative control (0.1× PBS) experiment. As expected, the smaller MNPs generated a smaller signal. It should be noted that while the out-of-plane magnetic field can be increased further to improve the amplitude, it is a delicate balance because as little as a 5-degree tilt between the sensor and a magnet can saturate the sensors. Furthermore, the divergence of the magnetic field modulates the amplitude across the sensor array. As a result, only the sensors located in the middle of the array were used for this comparison.

We also varied the channel height and the out-of-plane field to balance the magnetic force to study the effect of flowing height on signal. For example, a 130 mT field was used for tall channels (40-µm) while 60 mT was used for 19-µm channels. The measured data from the M-450 MNPs is in excellent agreement with simulation (Figure 3.10), while the M-280 data deviated from the simulated values, likely due to aggregation and/or chaining. As expected, small channels ensure the close proximity of the MNPs; however, aggregation and clogging were issues for channel heights of less than 12 µm and widths less than 50 µm. As such, we implemented the taller channel for rigid analytes

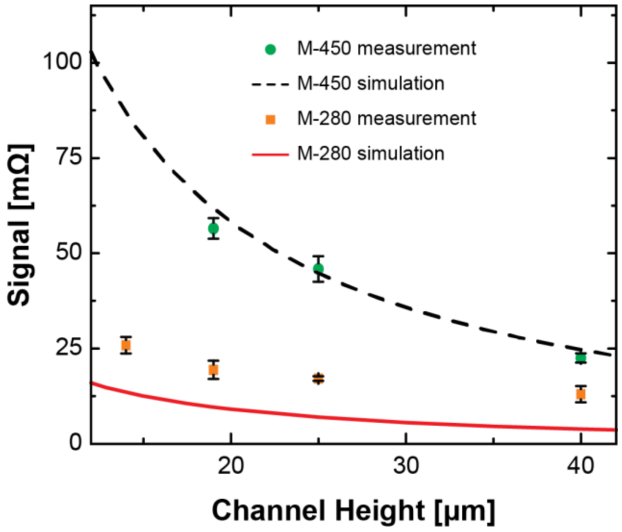

Figure 3.10 Comparison of measured results and simulations using Dynabeads

The experimental result of M-450 is in excellent agreement with the simulation, while the average signal amplitude of M-280 deviated from the theoretical prediction owing to the aggregation and/or chaining.

where the channel height is at least 2× larger than the MNPs or biomimetic constructs, and comparable channel height for cells that have more shape flexibility.

3.6 Time-of-flight and Implementation of Signal Processing

Raw data with no signal processing was collected while flowing 4.5 μm MNPs. As can be seen in Figure 3.11, each sensor in the linearly spaced array shows a time-sequenced response as the MNPs pass over the sensors. From these data, both the intra-sensor ToF (time between peaks within a signature) and the cross-sensor ToF (time between signatures on adjacent sensors) can be calculated. The ToF data directly measures the analyte velocity and serves as a proxy of its size, and the amplitude of the signature can be used to retrieve the vertical position of the analyte from the simulation library (Figure 3.5). At the current sampling rate, this system can handle velocities up to 7 mm/s without distorting the signature shape. Thus, the ToF data enables the MFC to have

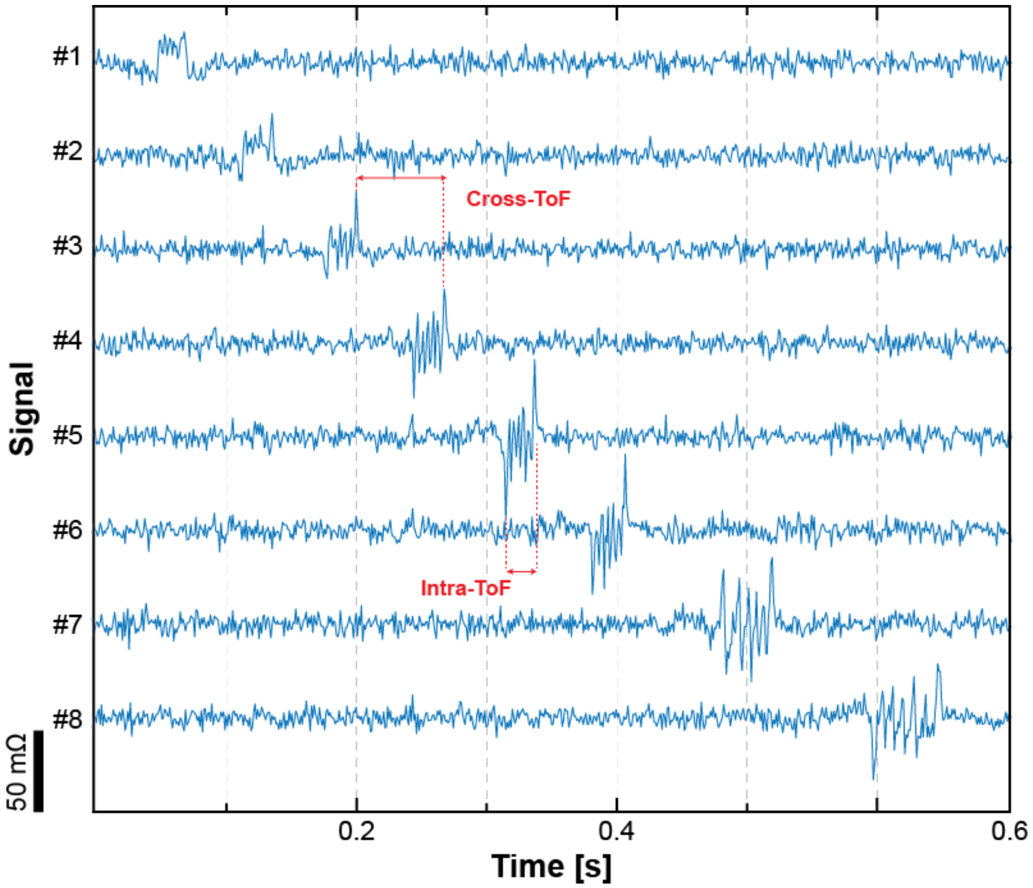

Figure 3.11 ToF measurement

Measured data from the 1×8 sensor array exhibiting sequential signaling which enable ToF calculations and subsequent signal processing.

multi-parameter analysis (*e.g.*, height, velocity, # of MNPs) of the analyte to further aid in discrimination and reduce false positives by signal processing.

MF was applied on the acquired data to improve the SNR and improve the detection efficiency. By using a multi-stripe GMR configuration that creates a more complex signal, the benefit of MF becomes more significant compared to many previous designs that used only a single stripe sensor resulting in a simple bipolar signature[72]. The complicated multi-peak signature here provides a more reliable and robust matching sequence reducing the minimum detectable SNR from 14 to 2.5 dB. Figure 3.12 shows a snippet of measured data where simple thresholding at 5σ (SNR=14 dB) results in missing the event; however,

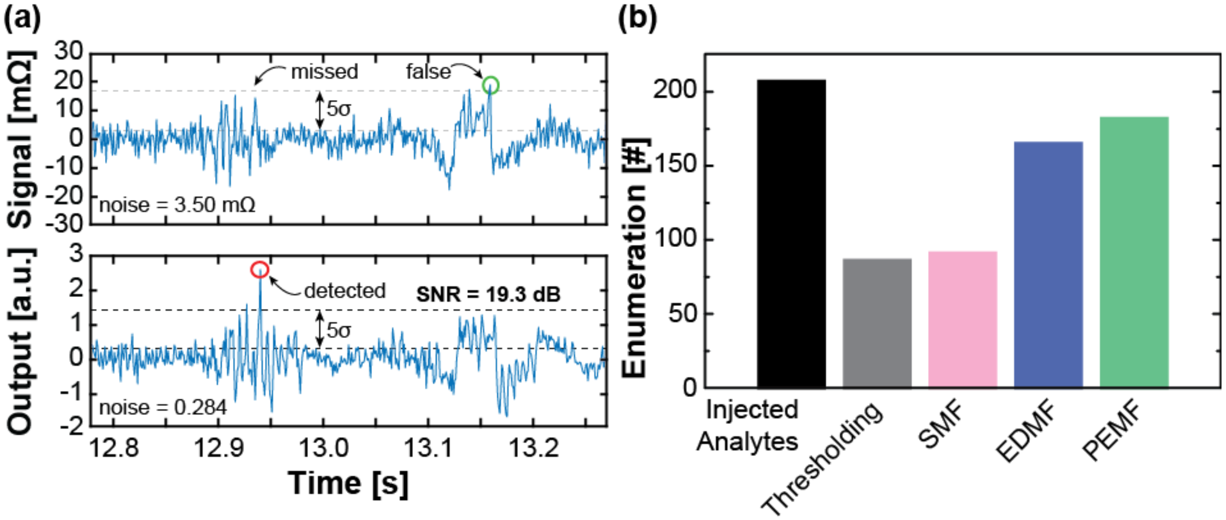

Figure 3.12 Demonstration and comparison of signal processing

(a) Measured data showing missed detection using only raw-data thresholding and correct detection using matched filtering (PEMF). (b) Comparison of enumeration using different signal processing techniques.

when applying MF, the event is clearly visible at 12.95 s. Also shown is a motion artifact caused by a large impulse response at 13.15 s that would be counted as a false detection with thresholding. However, since this impulse does not possess a signal-like signature, the matched filtered output is kept within the 5σ threshold and it is correctly rejected.

Three types of matched filters were evaluated: SMF, EDMF, and PEMF. The SMF looks for measured data with a similar pattern to those in a pre-computed simulation library based on Eq. 2.3. The EDMF template quantizes the expected signature into a tertiary square waveform: a positive level, a zero level, and a negative level. The tertiary template created rectangular notches in a range where peaks were expected to be, roughly matching the waveform in a low-resolution fashion and allowing for tolerance in peak position. By arranging the levels in a pattern that corresponded to the expected pattern, the filter finds expected peaks while normalizing the expected peak values to minimize that degree of uncertainty. The PEMF uses signatures from upstream (*i.e.* a previous sensor) recorded events. After finding the signal sequence on any of the other sensors, the detected signature is used as a template to compare against all other sensors for correlation within a time window based on the flow rate. In a relatively short time window, the flow rate, MNP distance to the sensor, and other slowly changing environmental parameters can be regarded as constant. Therefore, each of the sensors produces their own signature but delayed in time based on the velocity. An event was claimed if the MF output exceeds the threshold which was set as 5σ from the noise. A majority voting algorithm with the eight sensors is used to reduce uncorrelated noise and declare a detection event.

Each of these MF templates has advantages and disadvantages. For example, owing to variations in particle size, even with the same pumping rate, particles can move at varying speeds, creating variations in the length of the target event waveform. The SMF struggles with intricate time warping between the measured signal and the template signal. In this case each peak start and end time could be slightly off from the template waveform, creating a complex warp from target to template where some areas of the signal are stretched and compressed at different rates. To deal with general differences in waveform size, we expanded the SMF library with a linear succession of filter lengths to discover each specific time variation. Stretching to different times required down-sampling or up-sampling. However, this increases the computation time significantly as the library expands. Alternatively, some advanced signal processing techniques, such as dynamic time warping (DTW)[74–76], could be explored to improve the system in the future. The EDMF is elegant in that it is essentially just looking for the coarse pattern but does not have as significant improvement in the counting efficiency. Time variations were much easier to tolerate because waveform integrity was not as important for what is essentially a complex square signal. Since peaks were already being detected in a range of times rather than at a specific time, the malleability of the template proved to be much more useful than using a simulated template. Though EDMF has more flexibility in time warping and shape distortion than SMF, the velocity must be restricted to keep the intact or semi-intact complex signature. The PEMF is much more tolerant of dynamic changes in velocity. The enumeration efficacy using different signal processing techniques can be seen in Figure 3.12. The PEMF outperforms the other techniques and was used for the remainder of this work.

3.7 Correlation with Optical Microscopy

To evaluate the efficacy and quantify the accuracy, we correlated the measured electrical signal with video recorded by an optical microscope (OM) while flowing biomimetic complexes (10-µm polystyrene spheres decorated with Adembeads) and M-

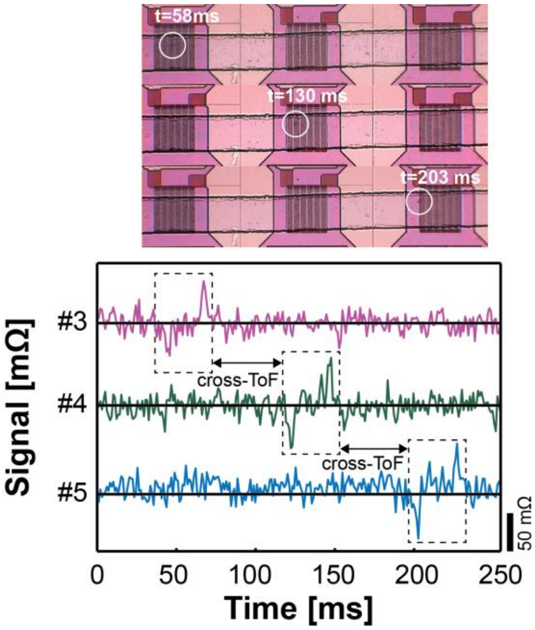

Figure 3.13 OM correlation

Measured real-time data of OM-monitored sensors which enable ToF measurements.

450 MNPs over the sensors. The Adembeads were chosen because they did not produce significant signal when not aggregated allowing differentiation between analytes bound with MNPs and unbound MNPs. Figure 3.13 shows the recorded electrical signal alongside the optical images at the same timestamps. The cross-ToF was 79 ms while travelling from sensor 3 to 4 and 78 ms from sensor 4 to 5. The intra-sensor ToF can also be extracted from the time span between two edge-peaks within a sensor, resulting in a velocity of 5.09 mm/s. The PEMF excluded the fast-flowing Adembeads and clusters based on their velocity and magnetic signature. The counting efficiency was compared between thresholding (5σ) and the PEMF using the optical counting as the ground truth (Figure 3.14). For M-450, both techniques have similar efficacy with detection rates of 80.62% and 92.25% for thresholding and the PEMF, respectively. However, for biomimetic MNP-decorated polymer spheres, thresholding only achieves a detection rate of 43.35% compared to the 88.18% with MF. This is likely due to the complex sample which contains both biomimetic spheres, individual MNPs, and clusters of MNPs. The MF correctly rejects the latter two whereas thresholding cannot differentiate. The OM correlation reinforces the results shown in Figure 3.12 that MF exhibits strong reliability when introducing a complicated matrix.

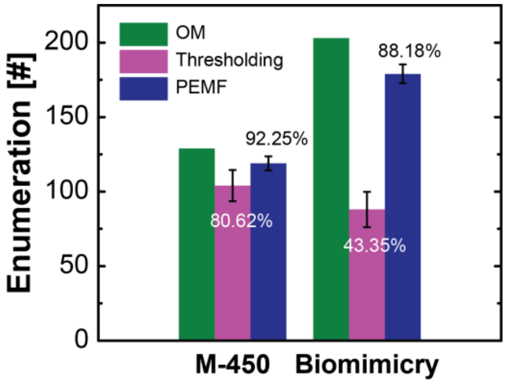

Figure 3.14 Compiled event-counting data

Receiver operator characteristic (ROC) curves were generated by sweeping the MF detection threshold to quantify the sensitivity and specificity of the proposed system. To establish ground truth, the flowing particles were analyzed frame-by-frame in ImageJ with size-based discrimination. Using just thresholding, the ROC curve lies very close to the random guess/chance curve, as shown in Figure 3.15. Applying the PEMF, the detection accuracy (=$\frac{true\ positive + true\ negative}{number\ of\ events}$) improved significantly, up to 83.68% for M-450 and 95.26% for biomimetic complexes clearly demonstrating the benefit of the MF. Different from the correlation rate in Figure 3.14, which was only considered the positive

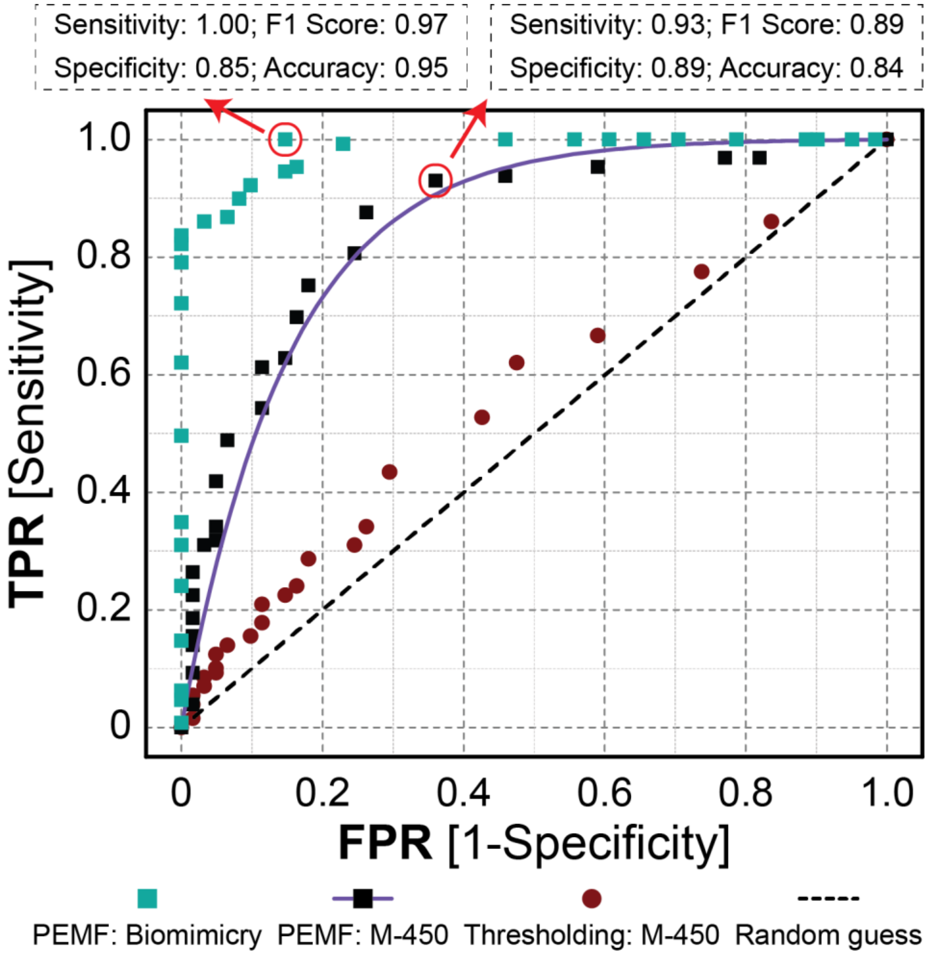
Sensitivity: 1.00; F1 Score: 0.97
Specificity: 0.85; Accuracy: 0.95

Sensitivity: 0.93; F1 Score: 0.89
Specificity: 0.89; Accuracy: 0.84

Figure 3.15 ROC curve

ROC curve of the selected sensor where green dots are the biomimicry data analyzed by matched filter, square dots with the asymptote (purple curve) are the M-450 data analyzed by matched filter, red dots are analyzed by thresholding from real-time data, and the grey dashed line is the reference of random guess.

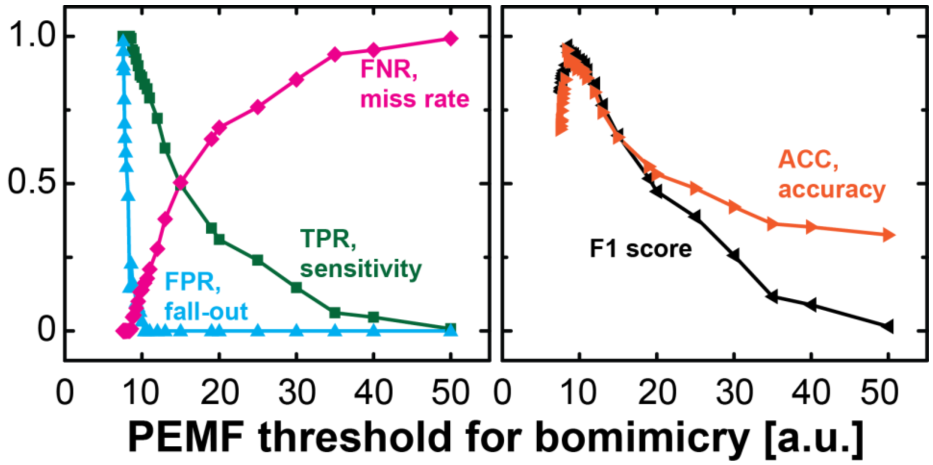

Figure 3.16 Tradeoff between detection and thresholds

The highest accuracy happened when threshold was set at 8.4

samples with rigid thresholds (5σ), the ROC curve reveals the tradeoff between sensitivity and specificity for a system. As shown in Figure 3.16, increasing the PEMF threshold improves the false negatives, while the sensitivity and false positives were reduced simultaneously. The system reached the best accuracy with a PEMF threshold of 8.4 compared to the 5σ (=9.6) used in thresholding. This threshold strikes a balance between positive samples and negative samples but can be tuned based on the application.

3.8 Development and Comparison of Magnetic Flow Cytometers

There has been significant interest in MFCs over the past decade, as shown in Table 3.1. Most prior MFCs have used high cross-sectional area to surface area ratio microfluidics ($\frac{Cross\text{−}sectional\ Area_{\mu fludics}}{Surface\ Area_{sensor}} > 10$) to achieve high throughput[35,44,48,49,51–54]. However, since the magnetic signal relies on the proximity to the sensing region (inversely proportional to the distance cubed), this is not typically a favorable design decision. As such, high area-ratio microfluidic setups lose most signals when MNP-decorated analytes flow near the middle of channel height compared to near the sensor surface. Some prior work have used magnetic chevrons[35,44,49] or electrical current lines[56] to guide the MNPs, which are close to the bottom of the channel, over the sensors and jetted successively to roll over the designated sensor area. Magnetic guides do improve the detection efficiency by focusing the analytes, however, they typically need slower flow rates which decreases the throughput and is prone to clogging. Another approach uses a strong magnetic field to attract the flowing MNP-decorated analytes near to the sensor surface, but the trajectory path makes signal modelling hard to translate into multi-parametric information and only allows binary outcomes. Furthermore, the tradeoff between forces acting in the microfluidics is complicated when using high throughput, and this kind of force analysis was mostly done for magnetic sorting[77–79]. As such, prior MFCs have not had high detection efficiency and high throughput as needed for rare-cell detection (*e.g.*, circulating tumor cells). Considering the sensor design, miniaturization improves the sensor sensitivity, but the traditional single-stripe sensor geometry gives rise to the simple bipolar peak which is hard to differentiate signals from the noise in low SNR settings. To address this, we developed a GMR SV-based MFC with a large sensor, the size of the microfluidics, and used MF to recover the sensitivity and improve the specificity. This platform uses a multi-stripe GMR SV sensor with a large active area and serpentine geometry that results in a unique signature. Our work demonstrates that the accuracy can be up to 95% in complex sample while the throughput strides across two decades that fits the clinical needs.

Table 3.1 The development and comparison of MFCs

		Lab Chip '11	***Sci. Transl. Med. '12***	***Lab Chip '13***	***SREP '16***	***JSSC '17***	***Biosens. Bioe.'18***	***CICC '19***	**This work**
Device & System	sensor	GMR	μHall	GMR	GMR	spiral transformer	GMR	LC oscillators	**GMR SV**
	sensor size (w*l, μm^2)	3x40	8x8	2x30	2x30	~ 35x50	2x30	160 (diameter)	**120x120**
	sensor configuration	single-stripe	cross	Wheatstone bridge	Wheatstone bridge	planar coil	Wheatstone bridge	planar coil	**multi-stripe**
	sensor array	1x3	2x4	1x4	single sensor	1x4	single sensor	7x7	**1x8**
	magnetic bead size	50 nm	10, 12, 16 nm 3, 8 μm	200 nm 12 μm	50, 200 nm 4, 6, 8, 12 μm	1, 4.5 μm	6, 8, 12 μm	2.8, 3 μm	**200 nm** **1, 2.8, 4.5 μm**
Microfluidics	dimension (w*h, μm^2)	150x14	125x25	700x200	700x150	200x100	1500x150 1500x300	60000	**90x14 – 250x25**
	focusing technique	sheath	sheath	magnetic	magnetic	sheath	magnetic	--	**laminar**
	throughput (μL/min)	1.26	1.67 – 16.67	24 – 60	60	2.5	72 – 90	36	**0.5 – 50**
Signal	Signal Processing	peak thresholding	N/A	peak thresholding	peak integral	matched filter	peak integral	cross-correlation	**matched filter** **cross-correlation**
Outcome	OM correlation	--	--	Yes	Yes	--	Yes	Yes	**Yes**
	detection efficiency[1]	N/A	N/A	N/A	N/A	74% – 87%	N/A	N/A	***92.25%** ****88.18%**
	accuracy	N/A	0.96	N/A	N/A	N/A	N/A	N/A	***0.84** ****0.95**

[1] detection efficiency is defined as the correlation rate in our *measured with Dynabeads M-450 **measured with CP10N-Adembeads complex

3.9 Summary

In this work, we developed a GMR-based MFC to leverage the best scenario for future cancerous detection, the multi-stripe layout generates a characteristic signature that is detected using MF and allowed discrimination between different types of magnetic labels. We characterized the system operation by microfluidic dimension and hydrodynamic force study with both computational simulation and experimental measurements. Couple tactics of signal processing were deployed to evaluate and improve the credibility of detection efficiency, the MF validifies the more than 5-fold improvement in minimum SRN requirement. Coupled with cross-sensor correlation technique, the enumeration between optical observation and filtered electrical readout can be up to around 90% correlation with 5σ thresholding. Furthermore, the ROC curve reinforces the potential for future application with 95% accuracy in biomimetic model. In brief, this GMR-based MFC offers an alternative to optical FCM with increased portability and rapid "*sample-to-answer*" measurement capability.

Chapter 3, in part, is based on materials from Chih-Cheng Huang, Xiahan Zhou, Da Ying, and Drew A. Hall, "A GMR-Based Magnetic Flow Cytometer Using Matched Filtering," in *Proceedings of IEEE Sensors 2017*, Glasgow, Scotland, Oct. 30 – Nov. 1, 2017; and a manuscript currently being prepared for submission for publication by Chih-Cheng Huang, Matthew Chan, Xiahan Zhou, and Drew A. Hall. The dissertation author was the primary investigator and author of these papers.

Chapter 4. AN APTAMER-BASED MAGNETIC FLOW CYTOMETER

4.1 Pancreatic Cancer and Aptasensors

In the US, approximately 57,600 people will be diagnosed with pancreatic cancer in 2020 and around 47,050 people will die of it, pancreatic cancer stands for ~3% of all cancers and ~7% of all cancer deaths[80]. The extremely low survival rate of pancreatic cancer stems from late diagnosis and that the symptoms are obscure, *e.g.* pain (usually in the abdomen or back), loss of appetite, jaundice, weight loss, nausea, and change in stool. Therefore, people have difficultly relating these symptoms to pancreatic cancer and do not seek timely treatment before it is too late. Detecting cancer early enables more treatment options and benefits the prognosis. For the major types of pancreatic cancer, the 5-year survival rate can be improved from 5% to 20% with early diagnosis. Therefore, there is an urgent need to develop a rapid diagnostic for pancreatic cancer. Epidermal growth factor receptor (EGFR), a transmembrane receptor tyrosine kinase, are overexpressed in up to 90% of pancreatic tumors. As a result, EGFR serves as a candidate biomarker for the early detection of pancreatic cancer and the inhibition of it can provide a possible treatment to improve the survival rate[81].

Aptasensors[82–89], constructed by combining an aptamer with highly sensitive transducers, have recently drawn attention for cancer diagnostics. Aptamers are a class of oligonucleotide (RNA or DNA), peptide or peptide nucleic acid that owns high affinity for the target analytes. Compared with antibodies, aptamers have several advantages: 1) small size, aptamers are usually 10-fold smaller than antibodies and exhibit better access to their target; 2) temperature-insensitivity, aptamers have longer shelf time and their denaturization is reversible; 3) fast and batch production, aptamers can be chemically synthesized without immune response, reducing the development time and cost. Consequently, aptamers are a strong candidate for the rapid cancer diagnosis in the early stages, and magneto-aptasensors owning the benefits mentioned in the previous chapters have emerged as an interesting avenue towards this goal.

In this chapter, we present the validation of cancerous diagnostics using MFC and its application on aptamer-based cellular detection, as shown in Figure 4.1. The cellular characteristics, measured by optical microscopy and Coulter Counter, establish the microfluidics design and correlate with MFC revealing the immunophenotyping of the pancreatic cancer cell lines (Panc-1 and MiaPaCa-2). The controlled experiments were performed to lay the foundation for the reliability of the technique. Two pancreatic cancer cell lines with over-expressed EGFR were discussed, the results of aptamer-based and antibody-based detection were compared. The outcome indicates the high correlation

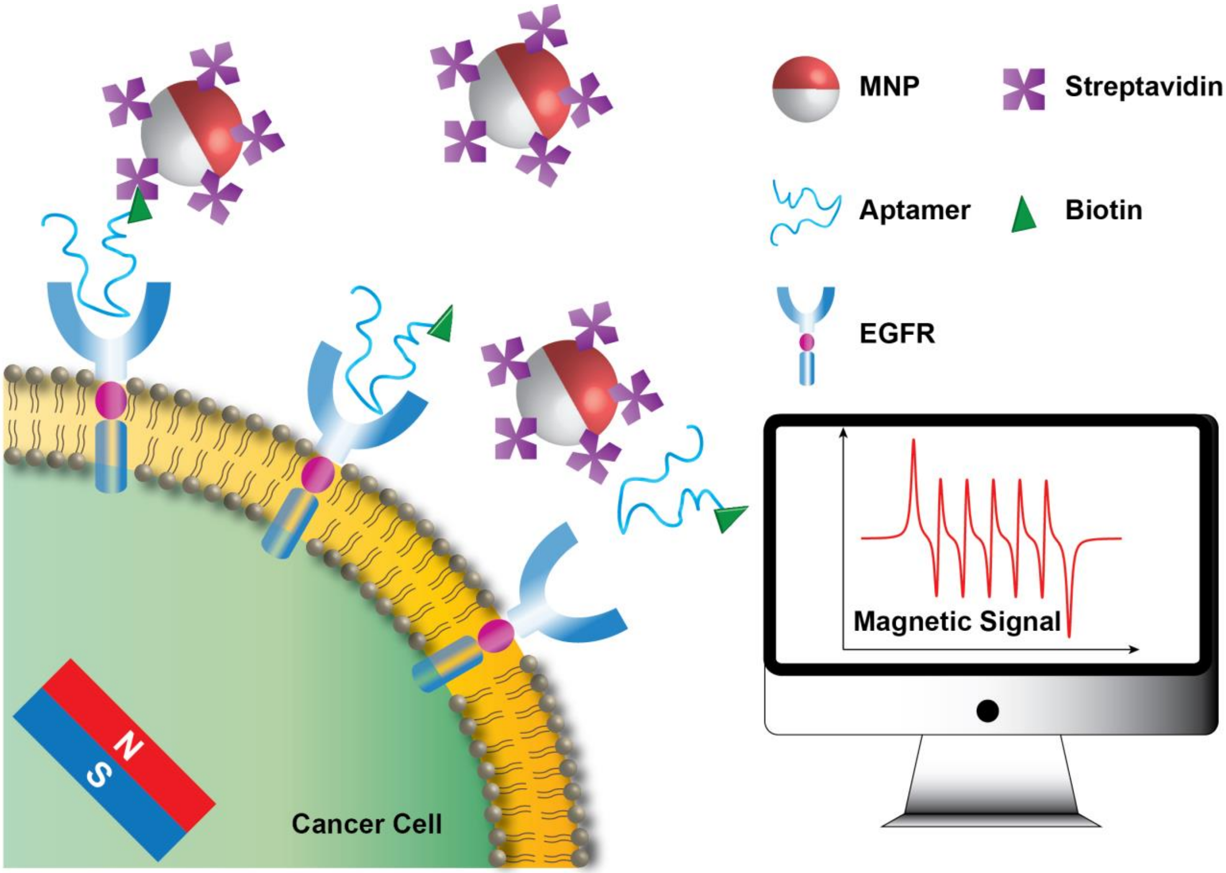

Figure 4.1 Schematic illustration of aptamer-based MFC

between MFC and conventional flow cytometry (FCM) (R^2=0.98) while MFC provides much less turnaround time and matrix insensitivity.

4.2 Materials and Methods

The MFC embedded with matched-filtering technique was utilized to conduct cellular measurements. We follow the protocol established in Chapter 3 and extend it to cellular measurements.

4.2.1 Western Blot

Panc-1 and MiaPaCa-2 cells were homogenized in a radioimmunoprecipitation assay (RIPA) buffer (Thermo Fisher Scientific, #89901) containing protease and phosphatase inhibitors (Thermo Fisher Scientific, #A32959). The total protein concentration was estimated and 30 µL (10 ng/µL) of the of the cell lysate were loaded and separated by sodium dodecyl sulfate-polyacrylamide gel electrophoresis (SDS-PAGE) before transfer to a nitrocellulose membrane (BioRad, #1620177). Membranes were incubated with primary mouse anti-EGFR antibody (BioLegend, #933901) at 1:1000 dilution and a secondary antibody, horseradish peroxidase-conjugated goat anti-mouse IgG at 1:1000 dilution (Thermo Fisher Scientific, #31430). As a protein loading control, a primary rabbit anti-Glyceraldehyde-3-phosphate dehydrogenase (anti-GAPDH) antibody at 1:1000 dilution (Abcam, #ab181602) and a secondary antibody, horseradish peroxidase-conjugated goat anti-rabbit IgG 1:1000 dilution (Thermo Fisher Scientific, #31460) was used. The antigen-antibody complexes were detected by the enhanced chemiluminescence (ECL) system (Thermo Fisher Scientific, #32106). A pre-stained molecular weight marker was run in parallel to determine the molecular weight of the proteins (BioRad, #1610375).

4.2.2 Optical Flow Cytometry

Panc-1 and MiaPaCa-2 cells were grown to 80% confluence and treated with Trypsin to detach them from the tissue culture flask. The cell number and viability were counted as described previously. A streptavidin-phycoerythrin (SA-PE, Prozyme) fluorophore was used to label the biotinylated anti-EGFR aptamer and the antibody. Cells (~1×10^6) were first incubated with the fluorophore labeled aptamer (100 nM final concentration) or the antibody (1:20 dilution) in 100 µL PBS/$MgCl_2$/$CaCl_2$ for 30 minutes at room temperature. The stained cells were subsequently washed 3 times with 200 µL of PBS/$MgCl_2$/$CaCl_2$, resuspended in 500 µL of the same buffer and analyzed using

FACSCalibur (BD Biosciences). The FCM data was analyzed by using FlowJo software (BD Biosciences).

4.2.3 Aptamer-based Magnetic Flow Cytometry

Panc-1 and MiaPaCa-2 pancreatic cancer cell lines were grown to 80% confluence in Dulbecco's modified Eagle medium (DMEM) (Gibco, #11965084) with 10% fetal bovine serum (FBS) (Gibco, #26140079) and 1% penicillin/streptomycin (Gibco, #15070063). The adherent cells were treated with Trypsin (Gibco, #25300062) to detach them from the tissue culture flask using standard cell culture techniques. The cell viability and the size were calculated using a Vi-CELL XR Cell Viability Analyzer (Beckman Coulter). The cells were finally washed and resuspended in PBS/$MgCl_2$/$CaCl_2$ (Gibco, #14040133) for the assay.

The 5′-biotinylated-E07 (anti-EGFR aptamer) was generated by performing an *in vitro* transcription reaction (DuraScribe T7 Transcription Kit, Lucigen, #DS010925), as described previously[81]. 5′-Biotin-G-Monophosphate (TriLink, #N-6003) at a 20 mM (final concentration) was also added to the reaction mixture for the incorporation of 5′-biotin to the E07 aptamer[90]. The transcribed 5′-biotinylated E07 aptamer was purified by denaturing polyacrylamide gel electrophoresis (PAGE). A biotinylated anti-EGFR antibody (R&D systems, #FAB9577B-100) was also used for comparison.

The cells (~3×10^5) were incubated with the 5′-biotinylated E07 aptamer at a final concentration of 100 nM in 100 µL PBS/$MgCl_2$/$CaCl_2$ buffer at room temperature for 30 minutes with gentle mixing. The biotinylated anti-EGFR antibody was used at a 1:20 dilution ratio under similar reaction condition. Streptavidin-coated Bio-Adembeads were

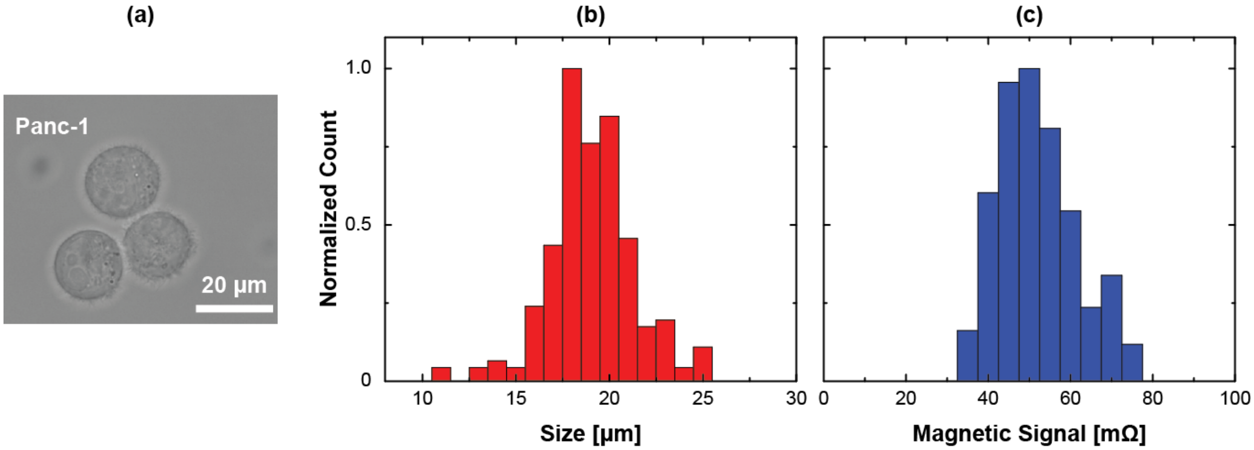

Figure 4.2 Cell phenotyping: size and size distribution of Panc-1

(a) The visualized Panc-1 cells captured by microscope. (b) Size distribution of Panc-1 cancer cells. (c) Magnetic signal distribution of Panc-1 cancer cells.

used in all the cellular detection assays. The beads were centrifuged/washed 3 times in 1× PBS/$MgCl_2$/$CaCl_2$ and diluted with DI water to 1:10 ratio. 40 µL of the diluted Adembeads were added to 90 µL of anti-EGFR aptamer or antibody-bound cells and incubated at room temperature for an additional 30 minutes with gentle mixing. The samples with ~1.68×10^9 Adembeads and ~2.4×10^5 cancer cells were finally resuspended in 1 mL buffer prior to injecting into the microfluidics.

4.3 Cellular Characteristics

To establish the utility of the MFC in a cell detection assay, we used pancreatic cancer cell lines, Panc-1 and MiaPaca-2, that overexpress EGFR on the cell surface. We started with cell phenotyping to set up the experimental design accordingly, the Panc-1 cells had a 19.51±0.83 µm mean diameter (Figure 4.2a,b) calculated using a Vi-CELL XR Cell Viability Analyzer (Beckman Coulter). Therefore, we used the 20-µm-microfluidics channel height that is close to the size of the Panc-1 cells, and the magnetic signal distribution (Figure 4.2c) was also highly correlated with size distribution, electrically

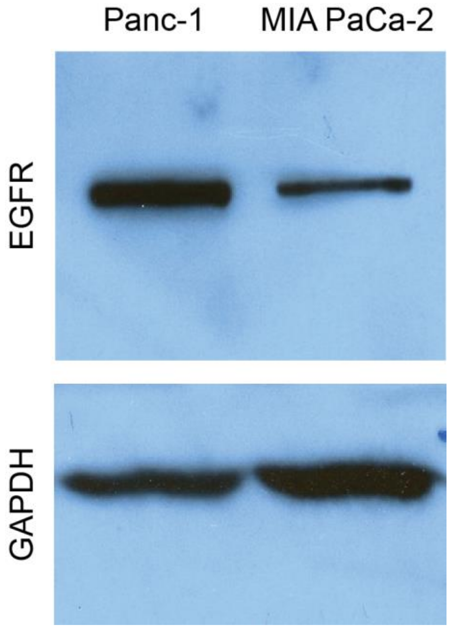

Figure 4.3 Western blot analysis

measured by the Coulter counter (Figure 4.2b). The magnetic signal also included the effect of bound MNPs with the pre-restricted flowing height, compared with the result from Coulter counter which only considered size, it shared the same trend but had a slight difference in distribution.

A 5′-biotinylated 2′-fluropyrimidine modified RNA aptamer (E07) that binds to EGFR with high affinity and specificity was used for the cell-labeling reaction[81]. We also used, a biotinylated anti-EGFR antibody as an additional cancer cell staining reagent. Western blot and optical FCM were used to verify the surface expression of EGFR on the pancreatic cancer cell lines. Panc-1 and MiaPaCa-2 cell lysates were subjected to Western blot analysis using anti-EGFR antibody. GAPDH, a house keeping protein, was used as the loading control. Panc-1 cells expressed more EGFR as compared to the MiaPaca-2 cells as shown in Figure 4.3. Optical FCM analyses of anti-EGFR aptamer (E07) and antibody binding to the Panc-1 and MiaPaCa-2 cells were performed by treating the cells with the fluorophore phycoerythrin (PE)-conjugated 5´Biotin-E07 aptamer (blue) or PE-conjugated

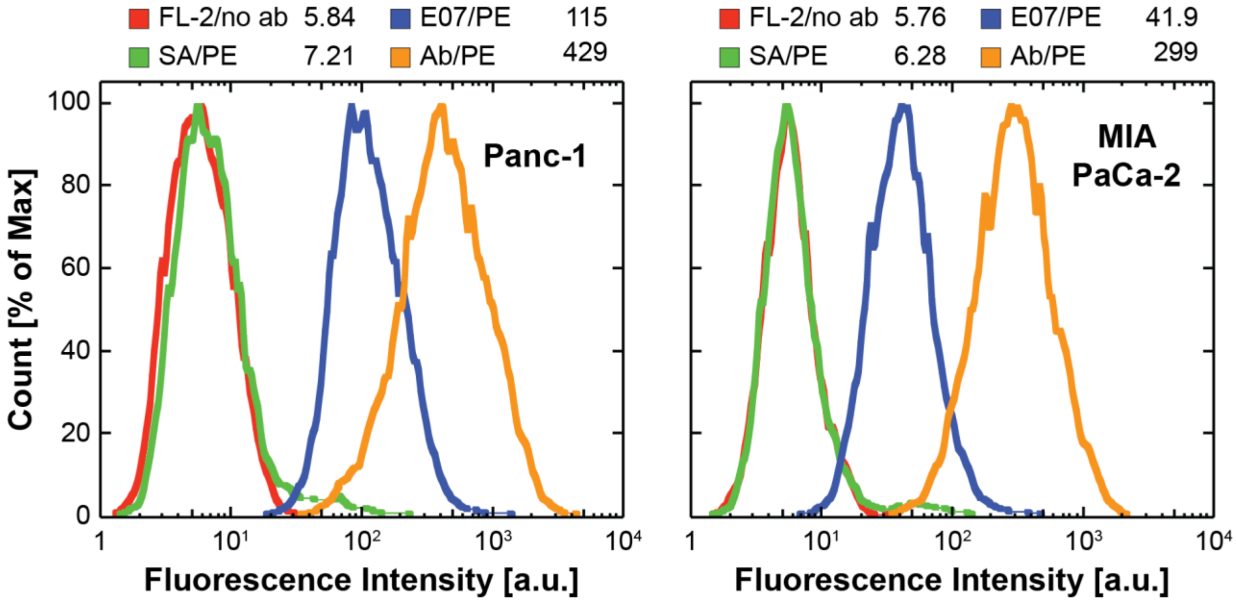

Figure 4.4 Optical FCM data for Panc-1 and MiaPaCa-2

Biotin-anti-EGFR antibody (orange) as shown in Figure 4.4. Streptavidin-PE was used as the negative binding control (green). The data was analyzed, and the mean fluorescence intensity (MFI) was calculated from the histogram plots.

4.4 Assay for Aptamer-decorated Pancreatic Cancer Cells

The MFC technique has demonstrated the validity and exhibited the excellent accuracy (95%) among high-throughput samples of the magnetic beads and biomimetic conjugates as presented in Chapter 3. To establish the aptamer-based cellular detection, we began with human pancreatic cancer cell line Panc-1. In addition, the microfluidic design followed the method mentioned in the literature[91] using the comparable dimension of analytes. Here, we utilize 20-μm-height channel which is close to the size of Panc-1 cell as shown in Chapter 4.3.

Panc-1 cells were conjugated with the biotinylated anti-EGFR aptamer and subsequently with the streptavidin-coated MNPs. This complex was then injected into the

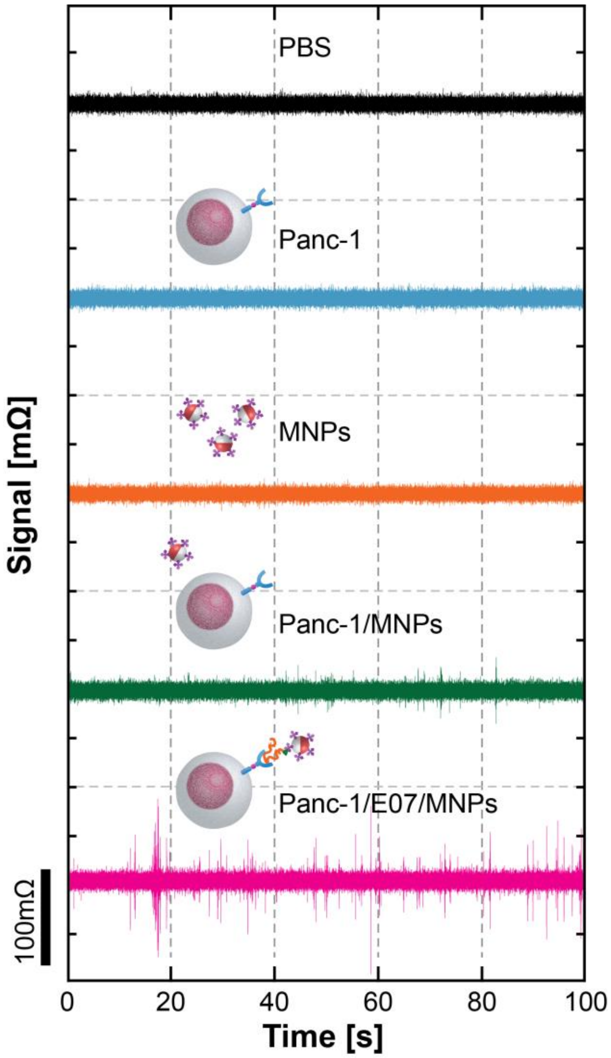

Figure 4.5 Real-time measurement of aptamer-based MFC

microfluidic channel and measurements were collected at 0.1 µL/min of throughput. As a negative control, we also injected PBS buffer, the MNPs alone, Panc-1 cells, and a mixture of MNPs and Panc-1 cells (without the aptamer linkers). In Figure 4.5 and Figure 4.6, little to no counted events were detected in the PBS buffer (*n*=0), the Panc-1 cells (*n*=0), or MNPs (*n*=38) using the PEMF described in Chapter 3. A small number of counted events (*n*=769) were detected in the Panc-1 and MNP mixture (without the biotinylated E07 aptamer linker), likely due to nonspecific binding on the cell surface from extremely excessive MNPs. However, in the presence of biotinylated E07 aptamer linker, the counted

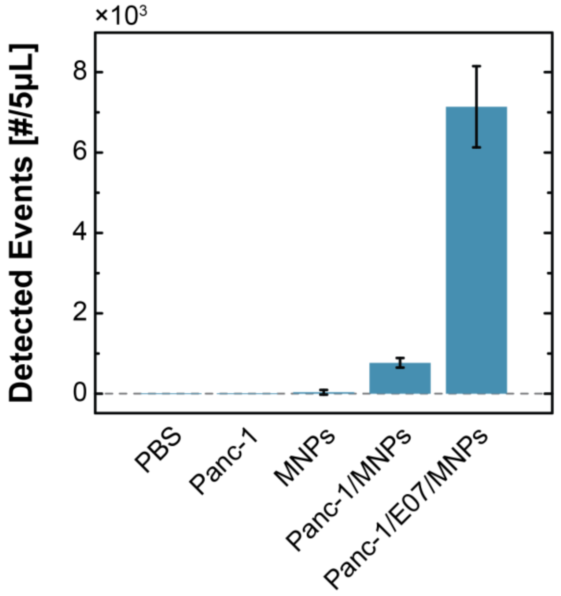

Figure 4.6 Enumeration plot derived from Figure 4.5

events increased nearly tenfold up to 7,140 per 5 μL in the Panc-1-E07-MNP mixture. The error bars represent the counting difference throughout the measurements across 8 addressable sensors.

To assess MFC performance in future applications, we further employed varying throughputs to detect Panc-1 with biotinylated E07 aptamer using the same procedure but switched the buffer to culture media (Figure 4.7). The data shows successful enumeration across two decades of throughput, ranging from 0.1 to 50 μL/min. Due to the viscosity[92], the enumeration (*n*=2711) and the best throughput (0.25 μL/min) for measurements were different from what was measured in Figure 4.5 (*n*=7140 under 0.1 μL/min). The distorted signal and sample aggregation occurred more frequently when throughput was increased, while Panc-1 cells were still also measurable (*n*=273) under 50 μL/min of throughput. Matrix insensitivity makes magnetic biosensors promisingly compelling over other medical devices since it can tremendously reduce the sample preparation and benefit the timely screening/monitoring of cancer diagnosis. We preliminarily investigated the matrix effect

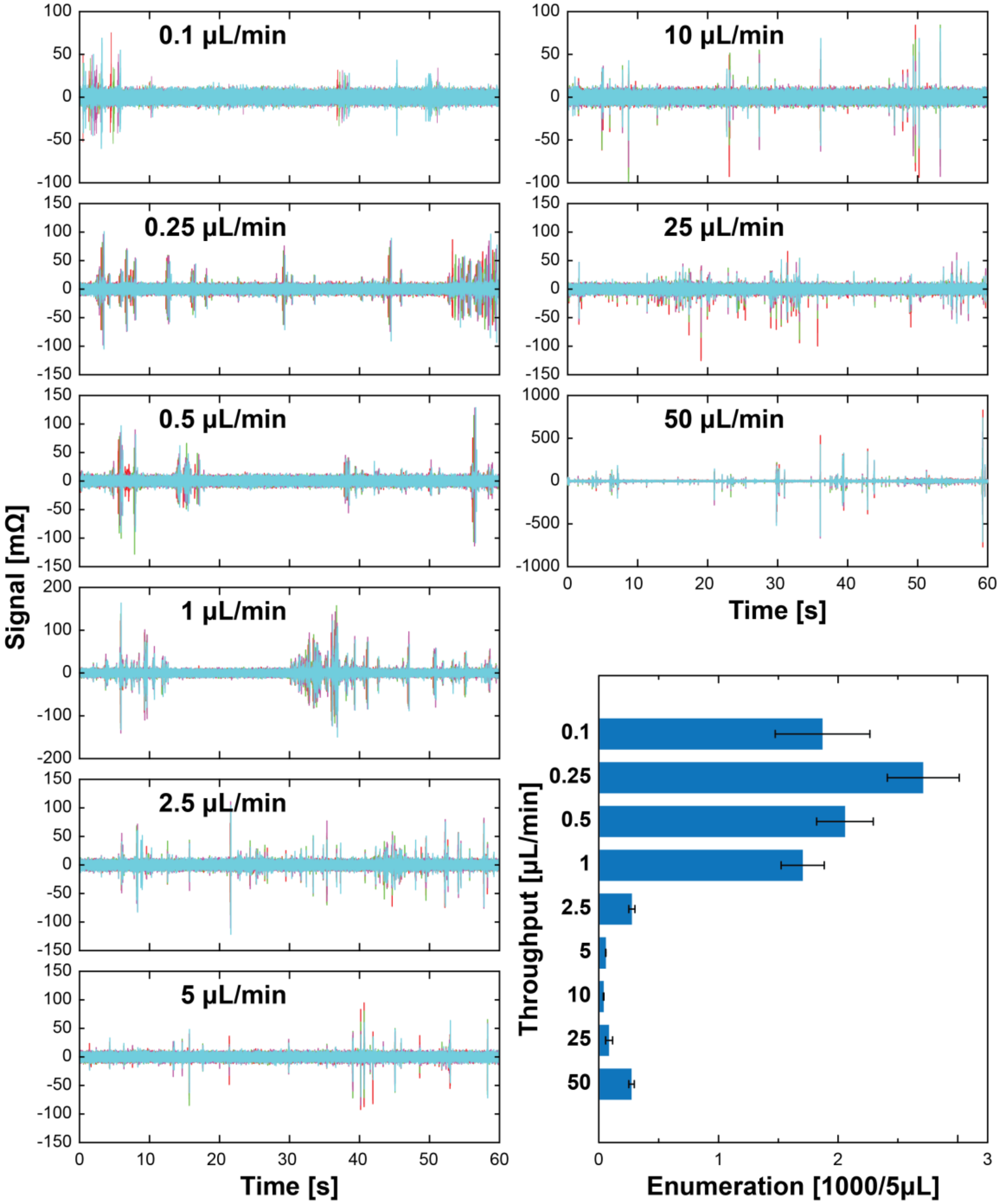

Figure 4.7 MFC measurements through varying throughputs across four sensors

with the MFC by comparing the results of MiaPaCa-2 in PBS and culture media, respectively, after 6 hours of incubation. The magnetic signal distribution of MiaPaCa-2 is presented, as shown in Figure 4.8. The MiaPaCa-2 shared the same trend of magnetic signal in PBS and culture media, respectively, while the mean value horizontally shifted

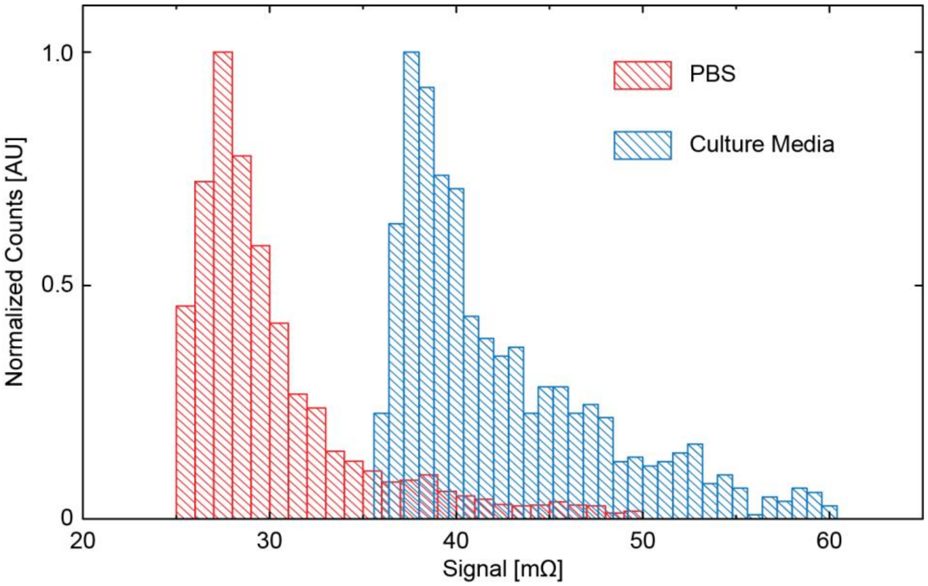

Figure 4.8 Signal distribution of MiaPaCa-2 after 6 hours of incubation

and increased around 10 mΩ. One suspicious cause of this signal increment lies in the difference of MiaPaCa-2 healthiness, since the culture media provided more necessary nutrients to cells and prolongs their lifetime. The hypothesis will be explored and verified in the future by designing the controlled experiments for varying incubation time in different matrix. In addition, the signal distribution of MiaPaCa-2 (Figure 4.8) is wider than what we found in Panc-1 (Figure 4.2), it can be attributed to an unexpected turbulent flow and smaller cell size in which the MiaPaCa-2 owned 16.71±0.89 µm while travelling in the 20-µm channel.

4.5 Correlation with Optical Flow Cytometry

Lastly, we compared the MFC and optical FCM data as shown in Figure 4.9. MFI was calculated from the histogram plots of the optical FCM data (Figure 4.4), and plotted against the mean magnetic intensity (MMI) values that were measured from the peak amplitudes of MFC data in each detected event. A very high correlation was obtained

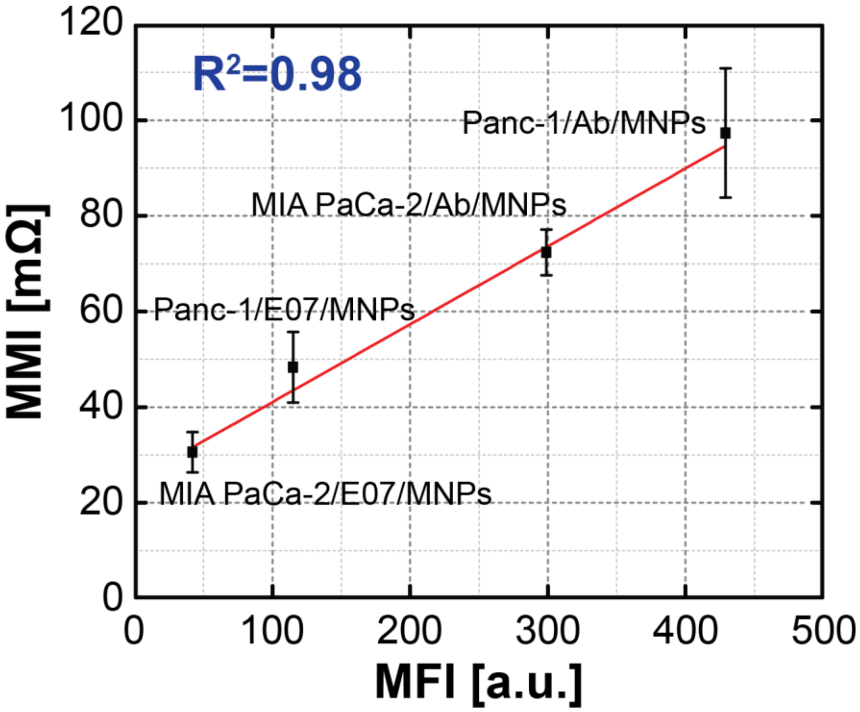

Figure 4.9 MMI vs. MFI

between the two FCM sensing modalities (R^2=0.98). To aid in the characterization, we constructed a numerical model that describes the magnetic response of MNP loading on a Panc-1 cell, as shown in Figure 4.10a. In the simulation, the cell was regarded as a sphere with random distribution of surface EGFR, and each EGFR can be bound with one MNP. Surface quantification of the bound MNPs can be derived as shown in Figure 4.10b. Due to the smaller size of MiaPaCa-2 (*i.e.* higher density of MNPs) and proximity sensing, MiaPaCa-2's signal would be larger than Panc-1's if both have the same amount of bound MNPs. The average magnetic signal in Panc-1/E07/MNPs is ~50 mΩ (Figure 4.9), and it indicates around 10,000 MNPs per Panc-1. While this is lower than the number of available EGFR binding sites (usually ~40,000)[93–95], it is likely due to weaker affinity of the aptamer (compared to antibody) and steric hindrance from the MNP (200 nm). Notably, the difference in the protein expression of EGFR on the cell surface of these two cell lines, Panc-1 and MiaPaca-2, were also reflected in the MFC data obtained by using two

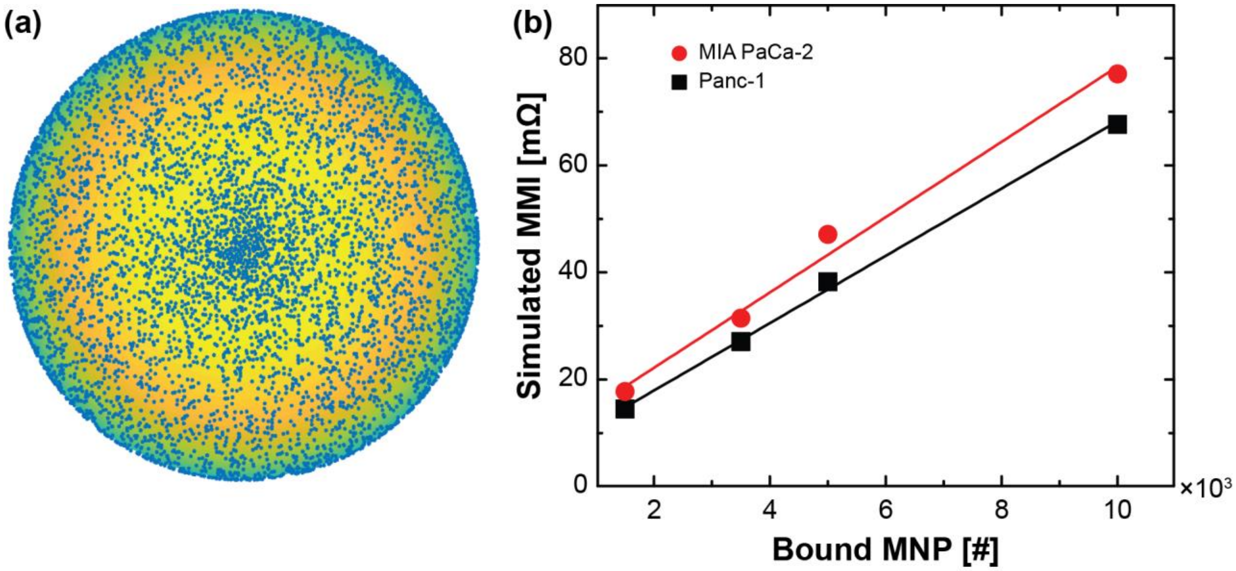

Figure 4.10 Simulated MMI vs. amount of bound MNPs

(a) Illustration from the simulated result of 10,000 random-distributed 200-nm MNPs on a Panc-1 cell (b) Simulated magnetic signal vs. number of bound MNPs to both Panc-1 and MiaPaCa-2.

different linkers, the anti-EGFR aptamer and antibody. Taken together, the data validates our proposed method against an optical FCM that is regarded as the gold-standard instrument.

4.6 Summary

An aptamer-based MFC used for cellular detection is presented in this chapter. Followed by the techniques described in Chapter 3, we utilized the MFC embedded with the PEMF to detect aptamer-decorated pancreatic cancer cells. Cellular phenotype was characterized to design the microfluidics accordingly and estimate the MMI prior to running MFC measurements. In the model study, EGFR-overexpressed Panc-1 cells were used to establish validity of cancerous measurements via the controlled experiment, the enumeration of positive samples is 10-fold higher than false positives. The EGFR expressions among Panc-1 and MIA PaCa-2 are discussed and compared with aptamer and antibody, magnetic signal shares high correlation (R^2=98.43%) with fluorescence intensity. At the time of writing this dissertation, the MFC system is being imiproved to diverify its applications, the matrix insensitivity and whole blood detection should be verified and established soon.

Chapter 4, in part, is currently being prepared for submission for publication of the material from Chih-Cheng Huang, Partha Ray, Matthew Chan, Xiahan Zhou, and Drew A. Hall. The dissertation author was the primary investigator and author of these papers.

Chapter 5. GMR BIOSENSORS FOR TIME-DOMAIN MAGNETORELAXOMETRY

5.1 Introduction

Among the many magnetic sensors available today, MR-based devices standout for PoC applications. In addition to the inherent advantages of magnetic biosensing, MR biosensors can be operated at room temperature, have high low-field sensitivity, and have comparably high transduction efficiency. These MR-based sensors operate on a quantum mechanical effect (either spin-dependent scattering or tunneling) where the resistance is proportional to the magnetic field with MR ratios ranging from 5% to >200% for modern devices[21,96].

Previously, these MR biosensors utilized static magnetometry where one detects the MNP's stray field in response to a DC or fixed frequency AC magnetic field. However, this technique requires a homogeneous magnetic field, complex readout electronics, and substantial signal processing to extract the minute signal of interest, all of which are challenging to do in a power constrained, remote PoC environment. An alternative

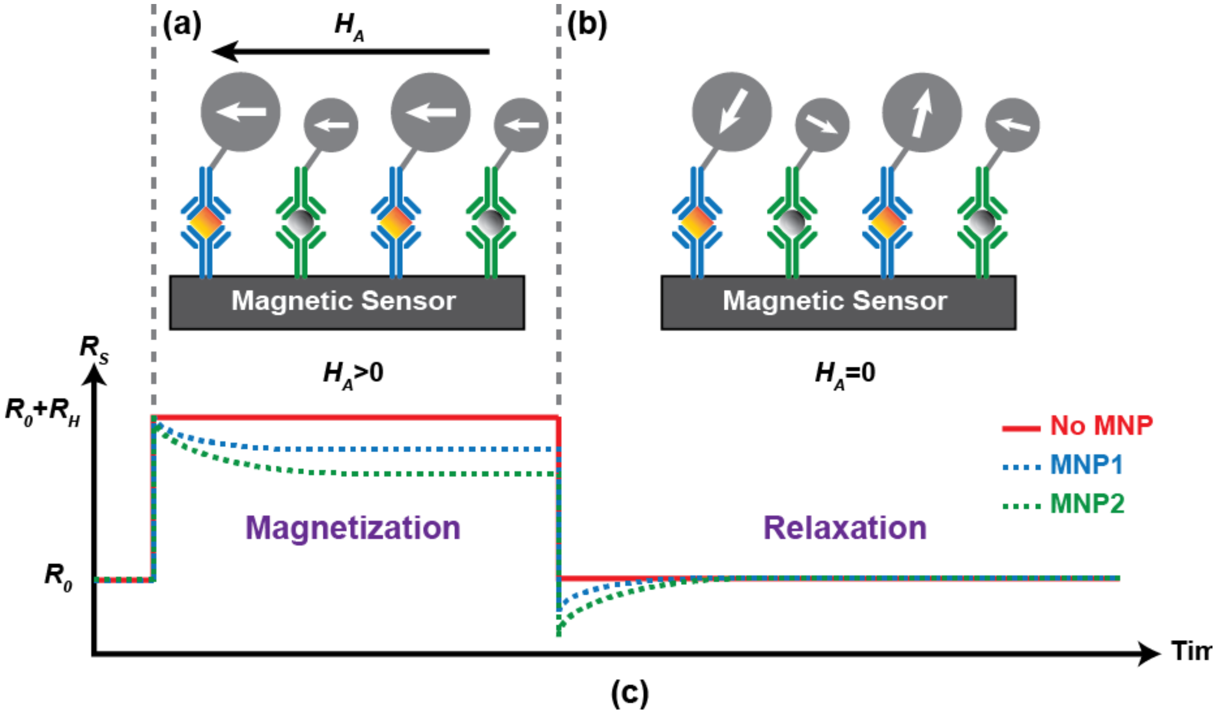

Figure 5.1 Illustration of time-domain MRX

(a) Magnetization phase (field $\boldsymbol{H_A}$>0) where the MNP magnetic moments are aligned to the applied field. (b) Relaxation phase (field $\boldsymbol{H_A}$=0) where the MNP magnetic moments gradually randomize. (c) The corresponding resistance of an MR sensor in response to the external magnetic field with and without MNPs.

approach is based on MRX where one detects the relaxation signature in response to a pulsed magnetic field. This technique removes the need for a homogenous magnetic field and requires comparably simpler readout electronics and signal processing. Figure 5.1 illustrates how this technique is applied for magnetic biosensing. In the absence of an external magnetic field, the magnetic moment of the superparamagnetic MNPs tethered to the surface of the sensor are randomly oriented resulting in zero net field. Then, $\boldsymbol{H_A}$ (defined in Chapter 2) is applied that magnetizes and aligns all the MNPs. The stray field from the MNP opposes the applied field resulting in a small change in resistance in the underlying MR sensor (Figure 5.1a). Note, this is the region of operation for static magnetometry. However, in MRX, the applied magnetic field is then switched off and the sensors monitored as the MNPs gradually relax to their equilibrium state (Figure 5.1b).

This relaxation occurs due to Néel and Brownian relaxation. Néel relaxation is the result of internal magnetic domain movement within the MNP whereas Brownian relaxation is the rigid rotation of the entire MNP. Since the MNPs are tethered to the surface of the sensor via antibodies or other molecular recognition elements, the relaxation process is predominantly Néel based. This relaxation signal can be either measured in the frequency- or time-domain. The frequency-domain technique uses a continuous AC magnetic field to measure the in-phase and out-of-phase component of the susceptibility whereas the time-domain technique measures the temporal response due to a pulsed magnetic field. In a PoC setting, the time-domain technique generally leads to a simpler implementation, however requires careful understanding of the factors that influence the signal, which has limited progress in the past.

In this chapter, we propose a novel time-domain MRX-based GMR biosensor[11] to observe Néel relaxation of tethered MNPs. To investigate this, we designed an ultrafast electromagnet with a switching time less than 5 µs (slew rate >1,000 T/s), which is much faster than the state-of-the-art with a 400 µs switching time (slew rate of 37 T/s)[97], to minimize the deadzone. Low-noise readout electronics were designed to capture the relaxation signal. The effect of the $\boldsymbol{H_A}$ and magnetization time (t_{mag}) were explored to understand their influence on the relaxation process. The results show excellent agreement with the empirical trend describing the relaxation based on natural-log behavior. We use these findings to optimize the system and perform a proof-of-principle magnetic immunoassay, which is to the best of our knowledge, the first time that GMR sensors have been reported for an MRX bioassay.

5.2 Materials and Methods

5.2.1 GMR Sensor Chips and Magnetic Nanoparticles

GMR sensor chips were purchased from MagArray. Each GMR chip has 80 individually addressable sensors arranged in 8×10 matrix with a R_0 of 1729 Ω and an MR ratio of 11.5%. The sensors do have hysteresis and anisotropy; however, this does not affect the proposed MRX measurement technique since the field is always swept along the same path and the resistance differential is measured. The magnetic particles used in all experiments were coated with streptavidin and purchased from Ocean NanoTech (#SHS-30-01), Micromod Partikeltechnologie GmbH (Nanomag®-D 130 nm, #09-19-132), and Thermo fisher Scientific (Dynabeads® MyOne™ Streptavidin T1, #65601).

5.2.2 Signal Modelling

To calculate the MNPs' average field on a GMR sensor, we adopted the model described in Chapter 2. Assuming MNPs are Langevin spheres in the field regime (2 – 100 Oe), MNPs have linear superparamagnetic response and give rise to a dipole field. The volume susceptibilities of SHS-30, Nanomag-D 130 nm, and MyOne at room temperature are 3.60, 4.44, and 1.38 (SI unit, dimensionless), respectively[98–100]. Here, we consider only the $\langle \boldsymbol{H_s} \rangle$ on the sensor from MNPs being magnetized by the $\langle \boldsymbol{H_A} \rangle$ as shown in Eq. 2.1. We neglect the component along long-axis ($\boldsymbol{x}$) of the sensor due to insensitivity of long-axis field, and only consider the total $\langle \boldsymbol{H_s} \rangle$ along the short-axis ($\boldsymbol{y}$):

$$\langle \boldsymbol{H_s} \rangle_{\boldsymbol{y}} = \sum_{i=1}^{n} \overline{\boldsymbol{H_b}}_{y}^{i} = \frac{\chi H_y \boldsymbol{R_B}^{\boldsymbol{3}}}{3l \cdot w \cdot th} \sum_{i=1}^{n} \int_{\frac{-t}{2}}^{\frac{t}{2}} \int_{\frac{-w}{2}}^{\frac{w}{2}} \int_{\frac{-l}{2}}^{\frac{l}{2}} \left[\frac{3(y-y_i)^2}{r^5} - \frac{1}{r^3} \right] dxdydz. \qquad 5.1$$

To extract the t_c, a MATLAB script was written that incorporates these equations, critical volume approximation[63], and the signal transduction to calculate the corresponding resistance change as:

$$\Delta R(t) = \mp S_0 \langle \boldsymbol{H_s} \rangle_y \, ln\left(1 + \frac{t_c}{t}\right). \tag{5.2}$$

5.2.3 Measurement Setup

The measurement setup consisted of a computer running MATLAB, a field programmable gate array (FPGA) (Opal Kelly XEM6310) to control the timing, a power amplifier (Kepco BOP 36-12ML), a custom designed coil driver and Helmholtz electromagnet, and custom designed readout electronics (Figure 5.2). The computer can digitally adjust both the magnetic field and magnetization time through the FPGA. The current from the sensors was integrated and then digitized using a National Instruments data acquisition card (NI PCIe-6351). To remove DC offset, temperature drift, 1/*f* and other correlated noises, and circuit non-linearity, a correlated double sampling (CDS) technique

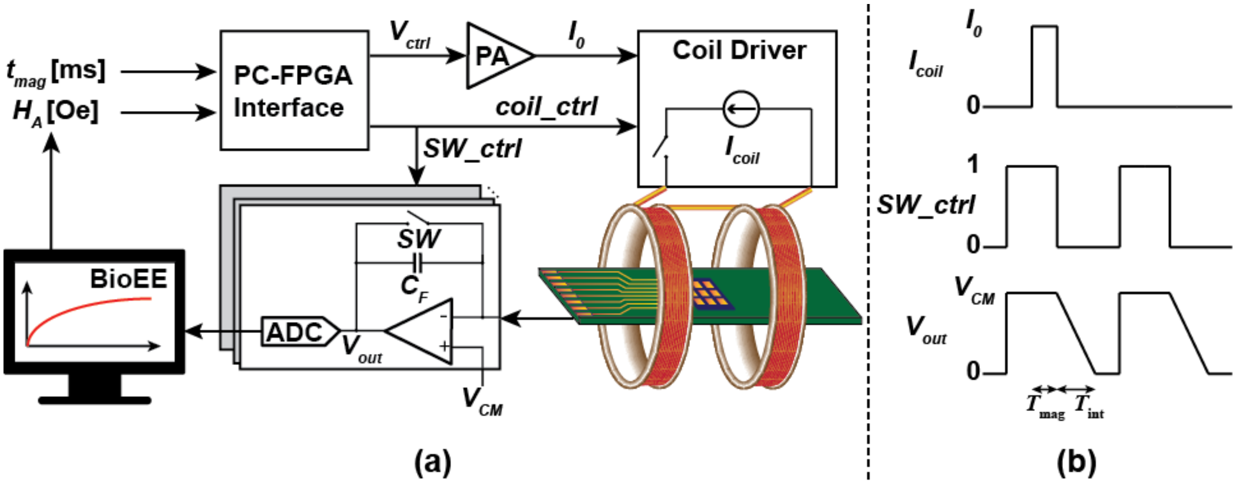

Figure 5.2 Simplified schematic of measurement system

Table 5.1 Summary of MNP concentrations

Cmpany	MNPs	Original Concentration	Concentrated Ratio	Final Concentration
Ocean NanoTechnology	SHS-30	33.9 nM	2×	67.8 nM
Micromod	Nanomag-D 130 nm	4.82 nM	5×	24.1 nM
Thermo Fisher Scientific	MyOne T1	14.1 pM	100×	1.41 nM

is used where the sensor is sampled two different times: once with the magnetic field and once without the magnetic field. The CDS technique eliminates the need for magnetic shielding, which is extensively used to minimize magnetic noise, circuit non-linearity, and hysteresis[97]. The extracted signal (ΔV_{out}) can be written as:

$$\Delta V_{\mathrm{out}} = V_{\mathrm{out|field}} - V_{\mathrm{out|no\ field}} \cong \frac{V_{bias}}{R_0^2 \cdot C_F} \int \Delta R(t) dt, \quad 5.3$$

where V_{bias} is the bias voltage (0.5 V), C_F is the integration capacitor, and ΔR is the MR signal due to the MNP. Multiple measurements were averaged to reduce the white noise and further improve the SNR.

5.2.4 Magnetic Nanoparticle Handling and Coverage Analysis

MNPs were washed with DI water before using, the resulting elimination of salt concentration improved the accuracy of coverage analysis. The MNP coverages were analyzed by MRX signals and scanning electron microscope (SEM) images, respectively. A FFT bandpass filter was applied during image processing to increase the contrast between MNPs and sensor substrate through software ImageJ. The MNP concentration was increased to modulate the surface coverage (Table 5.1).

5.2.5 Bioassay

The GMR sensors were functionalized with 99% (3-Aminopropyl)triethoxysilane (APTES) (Sigma Aldrich, #440140) for 1 hour at 37°C, followed by Biotin (Thermo Fisher Scientific, #21312) incubated for 1 hour at 37°C, and then coated with 2% bovine serum albumin (BSA) (Thermo Fisher Scientific, #37525,) for 30 min at room temperature. The reference sensors were covered with epoxy and part of sensors had only BSA without biotin as negative controls. The measurements were conducted with magnetometry to ensure the efficacy of MNPs binding via biotin-streptavidin interaction, followed by 1× PBS washing 3 times to remove unbound MNPs, and then performed MRX to detect the MNPs' relaxation signal via specific binding.

5.3 System Overview

The measurement setup consisted of an 8×10 GMR sensor array (MagArray Technologies, Inc.) placed inside an electromagnet (custom designed) connected to readout circuitry (custom designed) as shown in Figure 5.3. Due to the correlated double sampling technique, no magnetic shielding was required. Each sensor contained multiple GMR stripes to increase the surface area while maintaining the high aspect ratio of each stripe needed to keep the sensing layer stable with a R_0 of 1.7 kΩ and a MR ratio of 11.5% (Figure 5.3c). Streptavidin-coated MNPs (SHS-30-01, Ocean NanoTechnologies) were drop-casted on the sensors in the presence of an alternating field (50 Oe at 200 Hz) and allowed to dry before the experimental investigation of characteristic time, coverage, and

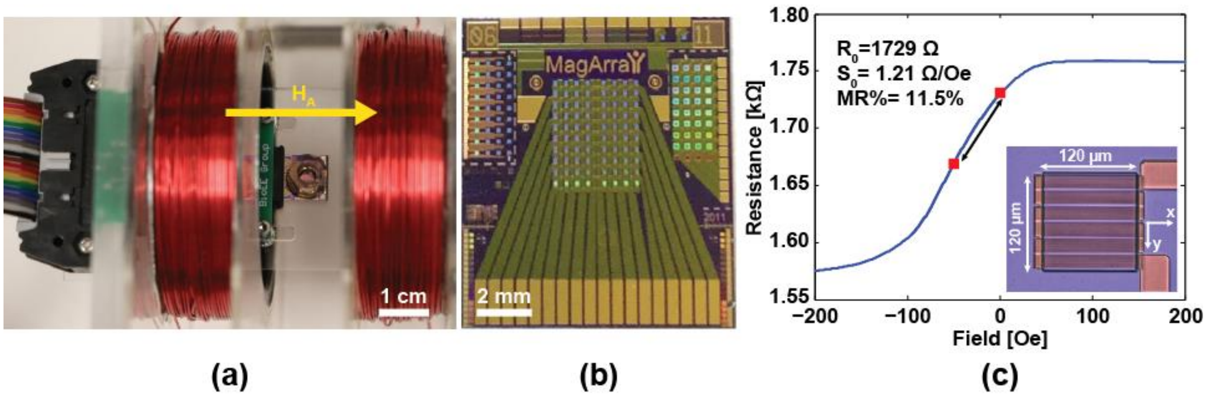

Figure 5.3 MRX system setup

(a) Simplified measurement setup with electromagnet, sensor array. (b) Photograph of GMR sensor array. (c) Optical microscopy image of a GMR sensor and measured magnetoresistance curve.

signal dependency (over applied field and magnetization time). Prior to drop-casting, select sensors were covered with epoxy to prevent the MNPs from being in close enough proximity to the sensor (~200 nm) to create a detectable signal. These epoxy-coated sensors were used as negative controls (reference sensors) while all others were active sensors with MNPs. For magnetic immunoassay experiments, the reference sensors were coated with BSA while active sensors were functionalized with biotin which facilitated binding with the MNPs through the high affinity streptavidin-biotin interaction. With the above setup and experimental procedures, we successfully monitored the relaxation process of MNPs. The active sensors exhibited a natural log-like response with a characteristic time of $3.3t_{mag}$ while the reference sensors showed no response. Next, we extended the investigation to extract the MNP coverage and confirmed it with SEM analysis. The measured signal was found to be proportional to the MNP concentration. To improve the empirical and theoretical study of time-domain MRX, we investigated the signal dependency on the applied field, magnetization time, and MNP size/composition. The results showed that other contributors (*i.e.* temperature and MNP core size) need to also be considered. The measurements of different MNPs showed that each has a unique

t_c roughly proportional with the core volume. Lastly, we performed a magnetic immunoassay to demonstrate the feasibility of this approach.

5.4 Investigation of Characteristic Time

Once the MNP is magnetized and the field is removed, there is insufficient energy to keep the moment of the MNP fixed. There are two mechanisms by which this loss of energy, or relaxation process, can occur. With two competing processes, the relaxation time will depend on the faster of the two mechanisms. Néel relaxation follows an exponential decay relationship when the MNPs are monodisperse[62,63,101,102], and depends on the core volume and anisotropy of the MNP as described in Eq. 2.5. However, this relationship becomes natural log-like when considering particle-particle interactions and the size/shape distributions of the MNPs[62,63,101–105]. The time-course magnetization during relaxation can be empirically described by the following equation in which is the extension of Eq. 2.7:

$$M_N(t) = \kappa \alpha M_0 \, ln\left(1 + \frac{t_c}{t}\right), \qquad 5.4$$

where κ is the surface coverage, α is a constant related to the magnetic viscosity. It has been previously reported that $t_c \approx t_{mag}$ when the applied field is relatively small (H_A=0.1 Oe)[62]. However, this has not been measured for more moderate magnetic fields that are appropriate for MR-based biosensing (20 – 100 Oe).

To measure the relaxation response, we restricted the particles to Néel relaxation by drop-casting a fixed volume of MNPs on the surface of the MR sensors and allowed them to dry while applying a magnetic field (50 Oe at 200 Hz). In such a configuration, the particles are rigidly attached and cannot undergo Brownian relaxation serving as a model system for the MIA. Moreover, the MNPs preferentially migrate into the trenches (the area between the stripes of GMR) in the presence of external field during the drying process, which significantly enhances the sensor response when MNPs are located close to the edge of trenches[106,107]. In these experiments, we followed the time-domain MRX procedure previously described (Figure 5.1). The H_A was set to 50 Oe and pulsed for a duration of 100 ms. The field was subsequently collapsed in under 10 µs. The resulting resistance of the MR sensors was measured by applying a constant voltage across the sensors and integrating the current (described in the Methods section). The integrators were synchronized to start integrating after the electromagnet was turned off. The sensor array contained both active sensors (*n*=29) and reference sensors (*n*=20) that were coated with a thick epoxy to prevent the MNPs from being near the MR sensor thus quenching the relaxation signal.

The reference sensors all showed near zero signal, as expected, whereas the active sensors all exhibited a characteristic MRX signal with an amplitude ranging from 2 mV to 15 mV (Figure 5.4a) due to the uncontrolled coverage on each sensor. When normalized by scaling the amplitudes to be the same (Figure 5.4b), it is readily apparent that each sensor is measuring the same process, just scaled by the surface coverage. From the fitted data, we found that t_c=3.3t_{mag}=330 ms for H_A=50 Oe and t_{mag}=100 ms (Figure 5.4c). Using magnetic modeling to simulate the response of this system with the same t_c, we found that the simulation results are in good agreement with the measured data. As will be shown later, t_c can be used as a unique magnetic signature for each type of MNP.

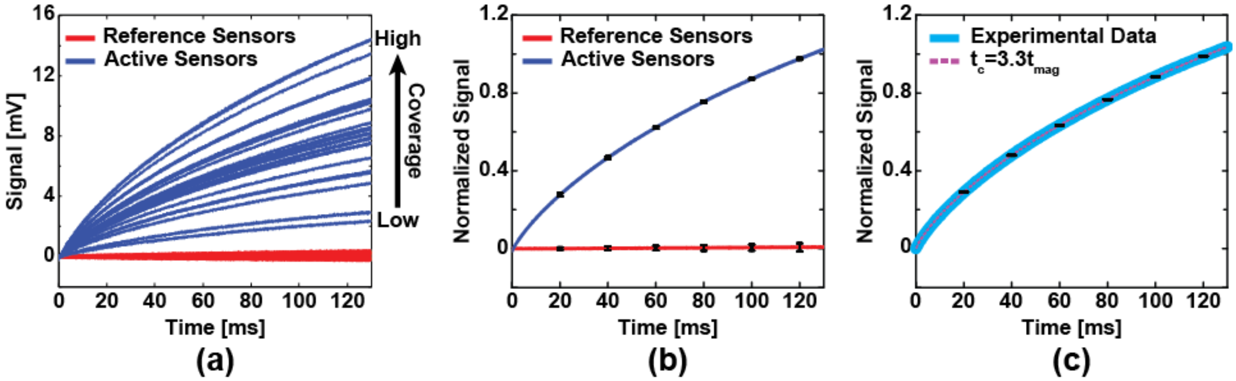

Figure 5.4 MRX measurements

(a) Measured MRX signals from active sensors (blue, *n*=29) and reference sensors (red, *n*=20). The different amplitudes indicate non-uniform MNP coverage. (b) Normalized relaxation signals demonstrating the homogeneous relaxation behavior. The curves are the mean signal of reference sensors and active sensors, respectively. Error bars are ±1σ. (c) Comparison between experimental data and simulation exhibits good consistency of the characteristic time of $3.3t_{mag}$. Error bars are ±1σ.

5.5 Coverage Extraction

After verifying the natural log behavior of the relaxation signal and measuring the corresponding characteristic time, we investigated the signal dependency on the MNP coverage. For the detection of biomolecules labeled by MNPs, extraction of the MNP coverage is required to quantitatively retrieve the concentration of analytes and further deduce the ligand-receptor interaction such as binding affinity and kinetics. In this section, we conducted the proof-of-principle experiments, extracting the coverage of MNPs in the absence of probe molecules (*i.e.*, surface immobilization). For a single MNP, the signal would be highly dependent on the location within the sensor[107], however with moderate surface coverage, the signal per MNP is roughly constant and independent of location other than if it is on top of the sensor or in the trench next to it[108,109]. Previously we were only able to calculate the relative MNP coverage based on the signal amplitude. To precisely extract the coverage parameter κ in Equation 5.4, we applied different MNP concentrations and imaged the sensors using a SEM after MRX measurements (Figure

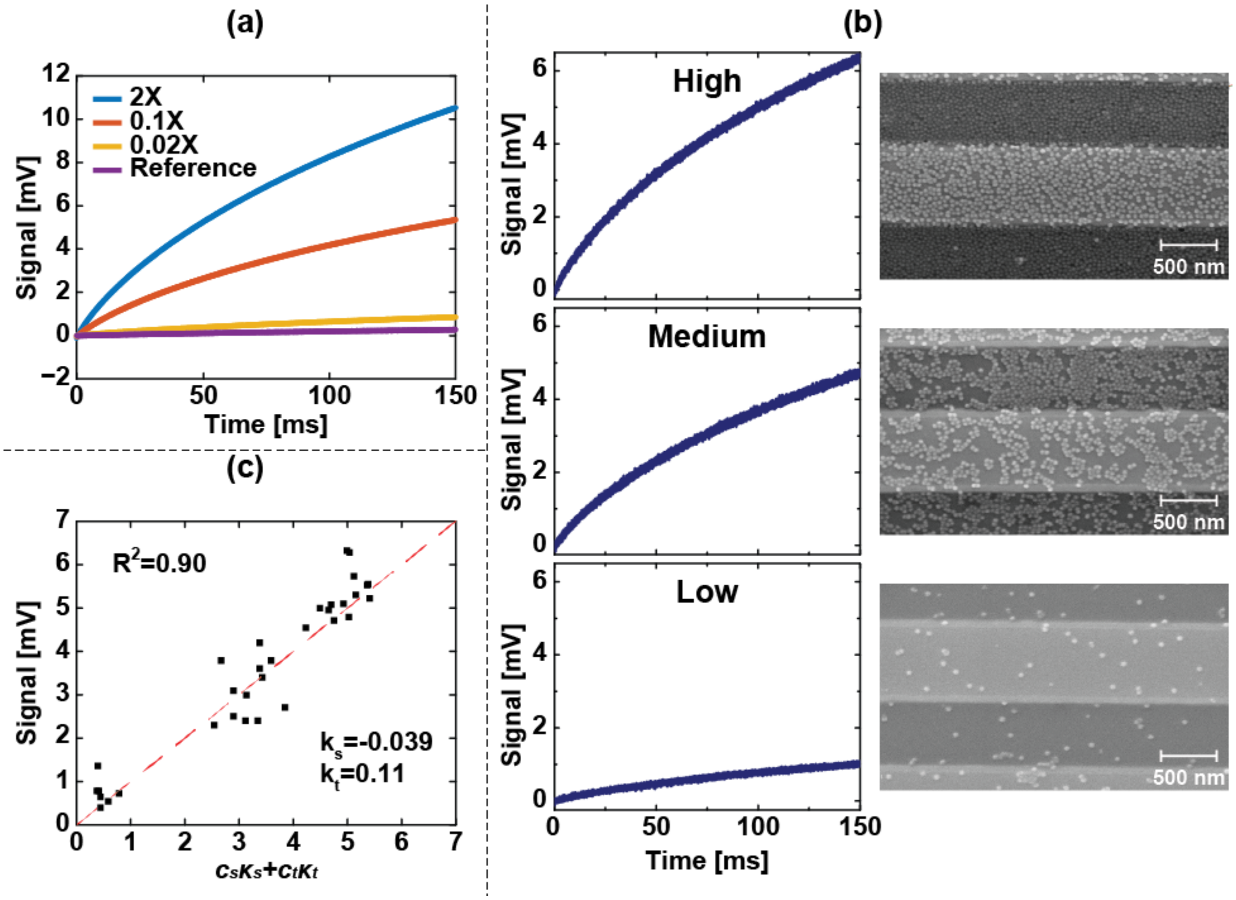

Figure 5.5 Signal dependence on MNP coverage

(a) Average signal under different MNP concentrations. (b) Measured relaxation signals and the corresponding SEM images. The three representative sensors, varied from low to high coverage of MNPs, exhibited high signal dependency over coverage. (c) Extraction of surface coverage showed different signal dependency on stripe coverage and trench coverage. The fitted coefficients C_s and C_t are -0.039 and 0.11, respectively.

5.5). The number of MNPs on the sensor was calculated from the SEM images and compared with the corresponding measured MRX curve. The signal is dependent on the concentration of MNPs as shown in Figure 5.5a, and the average signal at t=150 ms is 0.86 mV, 5.34 mV, and 10.51 mV for 0.02×, 0.1×, and 2× concentration of SHS-30 MNPs, respectively. It is important to note that the ratio of average signals between 0.02× and 0.1× ($Signal_{0.02\times}/Signal_{0.1\times}$ =0.16) is similar to the ratio of their concentrations ($Conc_{0.02\times}/Conc_{0.1\times}$ =0.2); however, this linear concentration dependency didn't adequately represent the signal with higher MNP concentration (2×) since multi-layer MNP structures were formed at this high of concentration. Furthermore, high MNP concentration is not a realistic scenario for bioassays where a monolayer is the theoretical limit due to the surface ligand binding. Consequently, we focused on the 0.02× and 0.1× MNP concentrations to extract the coverage where the signal per particle is linear and the coverage is still monolayer (Figure 5.5b). Since the design of the sensor geometry results in different signal dependent on the MNP position (*i.e.*, on the stripe vs. trench)[106], the total coverage over sensor area is not sufficient to address and extract the information of MNP coverage. Instead, the coverage should be evaluated with covered area over the GMR stripes and trenches (area between adjacent stripes), respectively. Equation 5.4 is modified accordingly to account for this dependence:

$$Signal(t) = (C_s k_s + C_t k_t) \int \ln\left(1 + \frac{t_c}{t}\right) dt, \tag{5.5}$$

where C_s and C_t are dimensionless coefficients containing the magnetic viscosity and signal per particle on the sensor and trench, respectively, and k_s and k_t are the stripe and trench coverage in terms of percentage. From the measured data, we found that C_s=-0.039±0.02 and C_t=0.11±0.018 (Figure 5.5c). The inequality of C_s and C_t proves the positional dependence and reaffirms the previously reported result that the MNPs in the trenches contributed to signal more than the MNPs on the stripes[107]. The correlation between signal and extracted coverage coefficients exhibited strong consistency (R^2=0.90) as shown in Figure 5.5c.

5.6 Signal Dependence on External Field and Magnetization Time

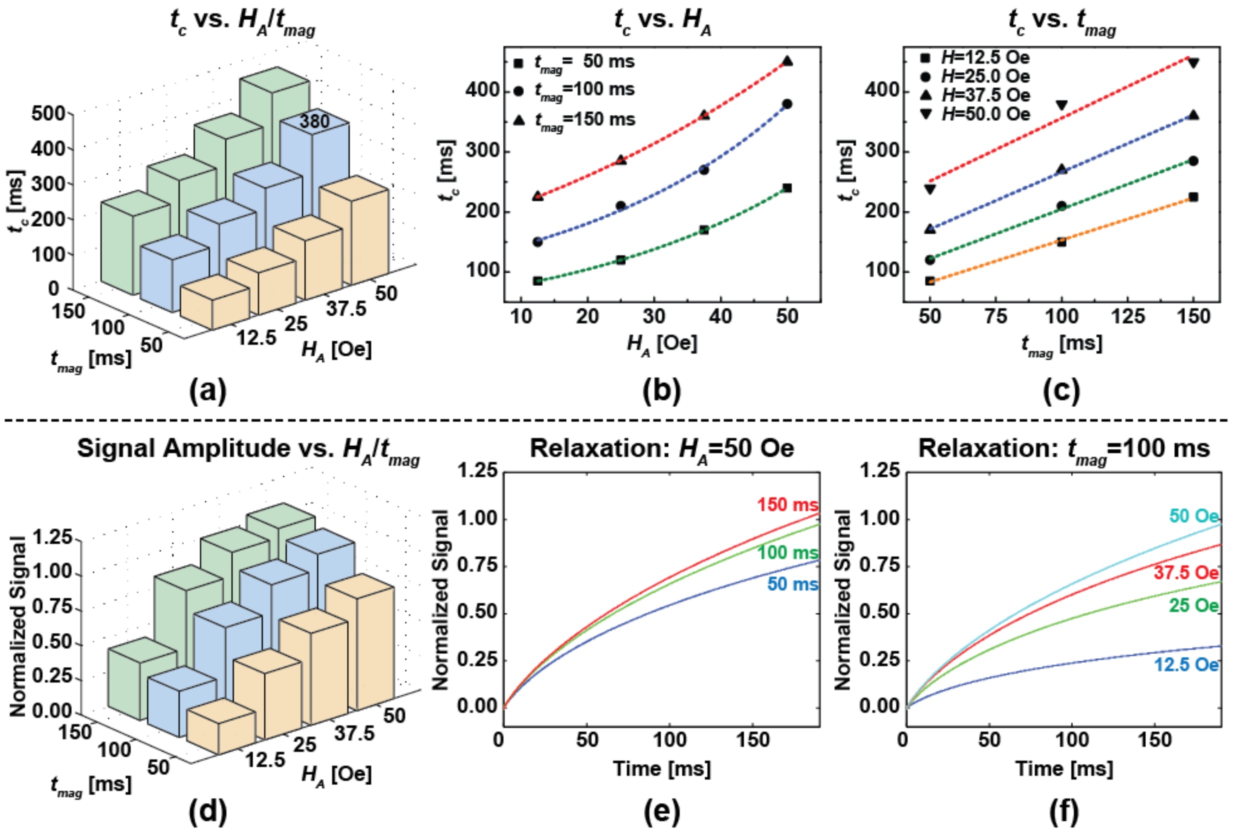

Figure 5.6 Signal dependence on applied field and magnetization time

Measurement results showing: (a) t_c dependency on H_A and t_{mag}, (b) the dependence of H_{A} on t_c, (c) the dependence of t_{mag} on t_c, (d) the (normalized) signal amplitude dependency on H_A and t_{mag} (e) relaxation signal under H_A=50 Oe with increasing t_{mag} (f) relaxation signal under t_{mag}=100 ms with increasing H_A.

Subsequently, we extended the experiment to measure the signal dependency on H_A and t_{mag} to optimize the time-domain MRX response. As expected, t_c has strong dependence on H_A and t_{mag} (Figure 5.6a), varying from 85 ms to 450 ms in the given range of H_A and t_{mag}. Based on our results, t_c has quasi-linear relationship with t_{mag}, while exponentially dependent on H_A (Figure 5.6b,c). The underlying theory still needs to be investigated to validate this observation. It should be noted that the extracted t_c=380 ms at H_A=50 Oe and t_{mag}=100 ms is not the same as previously measured (t_c=330 ms). We believe that this discrepancy is a result of different measurement temperatures (particularly here where the electromagnet was running for an extended duration resulting in an elevated temperature). Nevertheless, the signal amplitude followed the trend of t_c, as expected, when sweeping H_A and t_{mag} (Figure 5.6a). The normalized data, which were processed to remove the coverage, showed a positive correlation with the H_A and t_{mag} (Figure 5.6b,c). In terms of signal amplitude (Figure 5.6d,e,f), it shows diminishing returns when increasing H_A and t_{mag}, *i.e.* the increasing trend of signal is not as obvious as t_c with increasing H_A and t_{mag}.

5.7 Characteristics of Time-domain Magnetorelaoxmetry

Based on the previous sections, we can enhance the signal through increasing the external field, magnetization time, as well as higher MNP concentration. In this experiment, we fixed H_A=75 Oe and t_{mag}=150 ms and investigated the signal from different MNPs. According to the literature and datasheets[98–100], the mean core size is 7.7 nm, 12 nm, and 30 nm for MyOne, Nanomag-D, and SHS-30, respectively. The normalized signals, which eliminate the effects of coverage, exhibited characteristic signatures unique to each MNP (Figure 5.7a) and the extracted characteristic times of these three MNPs varied from 270

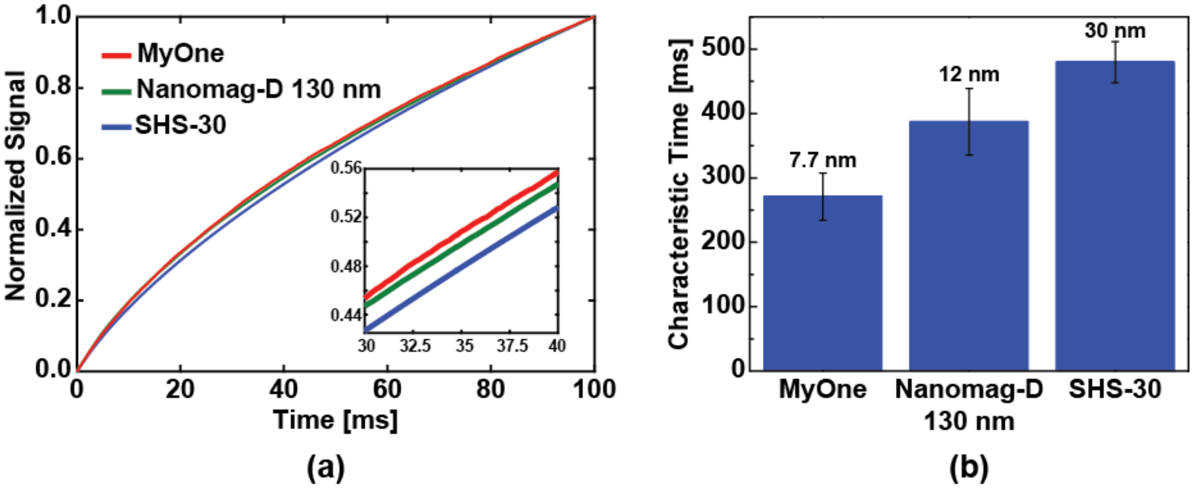

Figure 5.7 MRX of commercial MNPs

(a) Measured relaxation curves for different MNP and (b) the extracted characteristic time annotated with the core size of the MNP. Measurements repeated on multiple sensors (*n*=62, 45, 49, respectively.) Error bars are ±1σ.

ms to 480 ms (Figure 5.7b). The measurements were conducted under the same ambient temperature, hence the differences in the normalized signal must be rooted from the different characteristic times. These results agree with the increased Néel relaxation time as described in Equation Figure 5.7 where the time is dependent on the core volume. While time-domain MRX was substantially limited by the deadzone time (switching time) of the magnetic field in the early work[62,102], here we have dramatically improved the time-domain MRX system with GMR sensors and successfully detected three kinds of MNPs.

5.8 Progress toward Magnetic Immunoassay

To demonstrate MRX as a biosensing technique, we performed an immunoassay and compared the results to the conventional magnetometry approach. In this experiment, the active sensors were functionalized with biotin whereas reference sensors were functionalized with BSA. The protocol used to functionalize the sensors is described in the Methods section. It should be noted that this protocol was designed specifically for the SHS-30 MNPs that have a zeta potential between -40 to -20 mV[77,110]. To compare both techniques, MRX measurements were taken before and after adding the streptavidin-coated MNPs to the assay. The assay was monitored in real-time using conventional magnetometry[25] (Figure 5.8a). As expected, the streptavidin-conjugated MNPs bound to the biotin on the surface of the active sensors. The reference sensors showed no signal, indicating no specific binding. The corresponding coverage maps are shown in Figure 5.8b and Figure 5.8c for magnetometry and MRX, respectively. Both coverage maps show a high degree of similarity, confirming the validity of the proposed technique. Since the noise is uncorrelated in the MRX measurements, repeated measurements can be used to improve the signal to noise ratio at the expense of an increased measurement time. This

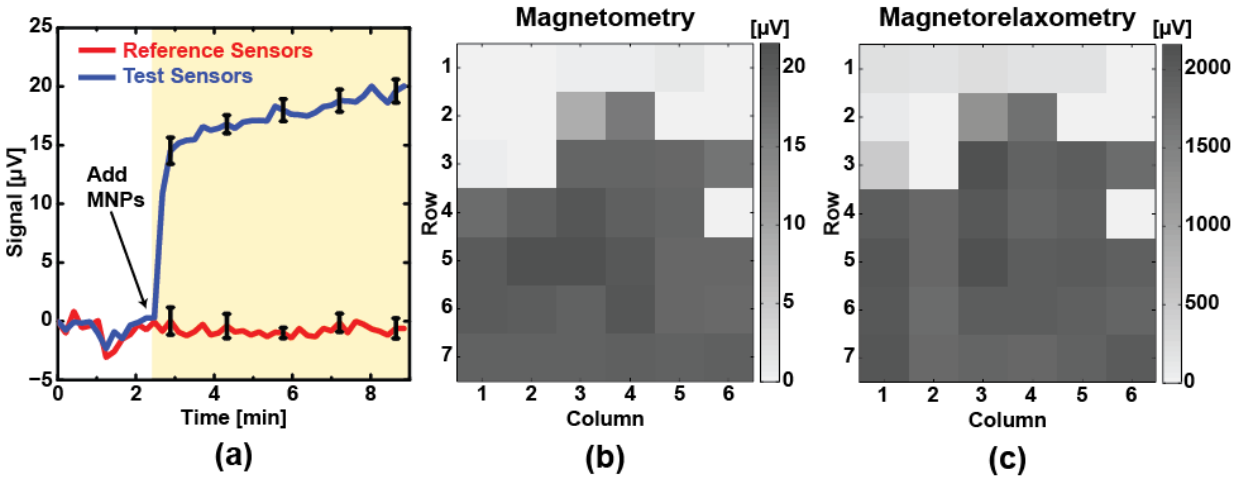

Figure 5.8 Bioassay: magnetometry vs. MRX

(a) Measured real-time magnetic immunoassay based on magnetometry, the curves are the mean signals of reference sensors (red, *n*=8) and active sensors (blue, *n*=25), respectively. Error bars represent ±1σ. Corresponding coverage map for (b) magnetometry and (c) magnetorelaxometry.

proof-of-principle experiment demonstrates the potential of utilizing the proposed time-domain MRX for *in-vitro* diagnostics.

5.9 Summary

Unlike the traditional magnetomertry which only measures the magnetic field, spin relaxometry (*i.e.*, electron spin and nuclear spin) measures the temporal magnetic response arising from the unique atomic structure. Early development on magnetic relaxation for biomedical applications focused on nuclear magnetic resonance (NMR) based on nuclear spin relaxation[111,112]. With the endeavor of miniaturization of NMR devices[113–116], relaxometry-based microchips have drawn attention recently and are moving toward molecular/cellular diagnostics using electron spin relaxation (ESR). However, both NMR and ESR typically require large magnets to generate the polarizing field limiting their miniaturization. With the state-of-the-art semiconductor technologies, MR-based biochips have the merits of low cost, integration of lab-on-a-chip, integrated electromagnets, and CMOS compatibility that can be further applied in PoC settings using MRX. Although MRX has been investigated for two decades, the lack of systematic study of MNP characteristics for temporal measurement has prevented time-domain MRX from being a reliable biosensing technique. Previously, the deadzone time restrained time-domain MRX from surface immunoassays, urging MRX toward frequency-domain measurements with homogeneous assays. Frequency-domain MRX has established the excellence in the homogeneous assay recently[34,117], however, its high dependence on hydrodynamic volume decreases the distinguishability between analytes and homogeneous assay increases the distance between analytes and sensor surface that would remarkably diminish the magnetic signal ($\propto {}^{1}/_{d^3}$). Due to the above challenges in MRX, there is an urgent need to re-innovate time-domain MRX in unprocessed samples without the loss of magnetic sensitivity. Some of the advanced works substantially improved the temporal limit of MRX by using Hall-effect and inductive microchips with a high sampling-rate ADC to capture the dynamic response[36,37,118–120], yet the realization on bioassay using time-domain GMR MRX hasn't been reported to date.

In this work, we successfully demonstrated a time-domain MRX for biotin-streptavidin assay using GMR biosensors to investigate the temporal relaxation of commercial MNPs. The experimental investigation was designed on a theoretical basis, from the investigation of Néel relaxation of dry MNPs which is prohibited from Brownian relaxation, coverage correlation that demonstrated unequal contribution of signal from stripes and trenches, extraction of characteristic time of different MNPs that proved the feasibility of distinguishing various MNPs in an assay, to the first realization using GMR on time-domain bio-MRX. In summary, the systematic investigation of our work on time-domain MRX enable us to perform bio-MRX with GMR biosensors.

Chapter 5 is a reprint of the material as it appears in *Scientific Reports* **7**, 45493 (2017), “Giant Magnetoresistive Biosensors for Time-Domain Magnetorelaxometry: A Theoretical Investigation and Progress Toward an Immunoassay,” from Chih-Cheng Huang, Xiahan Zhou, and Drew A. Hall. The dissertation author was the primary investigator and author of these papers.

Chapter 6. SUMMARY

6.1 Summary of Dissertation

This dissertation describes innovations made to MFC and time-domain MRX that integrate GMR biosensors with MF and high-slew-rate coils, respectively. The following is a summary of the key points and results presented in the dissertation.

Chapter 3 describes GMR-based MFC to leverage the best scenario for future cancerous detection, the multi-stripe layout generates a characteristic signature that is detected using MF and allowed discrimination between different types of magnetic labels. We characterized the system operation by altering microfluidic dimension and investigating hydrodynamic force with both computational simulation and experimental measurements. A couple methods of signal processing were deployed to evaluate and improve the credibility of detection efficiency, the MF validifies the 5-fold improvement in minimum SRN requirement. Coupled with cross-sensor correlation technique, the enumeration between optical observation and filtered electrical readout can be up to around 90% correlation with 5σ thresholding. Furthermore, the ROC curve reinforces the potential for future application with 95% accuracy in biomimetic model. In brief, this GMR-based MFC offers an alternative to optical FCM with increased portability and rapid "*sample-to-answer*" measurement capability. This work, in part, was published in IEEE Sensors Conference, and in part is currently being submitted for publication.

Chapter 4 presents the aptamer-based MFC for the cellular detection. Followed by the techniques which is described in Chapter 2, we utilized comparable microfluidics embedded with MF to detect aptamer-decorated pancreatic cancer cells. In the model study, EGFR-overexpressed Panc-1 cells were used to establish validity of cancerous measurements, the total counting owns 89.85% accuracy of true positives. The characteristics shows similar signal distribution across MFC and Coulter Counter while the distribution shifts after 5-hour measurement among different matrix. The EGFR expressions among Panc-1 and MIA PaCa-2 are discussed and compared with aptamer and antibody, magnetic signal shares high correlation (R^2=98.43%) with fluorescence intensity. This work in part is currently being submitted for publication.

Chapter 5 presents a novel time-domain MRX using GMR biosensors that observe Néel relaxation of tethered MNPs. To investigate this, we designed an ultrafast electromagnet with a switching time less than 5 µs (slew rate >1,000 T/s), which is much faster than the state-of-the-art with a 400 µs switching time (slew rate of 37 T/s), to minimize the deadzone. Low-noise readout electronics were designed to capture the relaxation signal. The effect of the applied magnetic field amplitude and magnetization time were explored to understand their influence on the relaxation process. The results show excellent agreement with the empirical trend describing the relaxation based on natural-log behavior. We use these findings to optimize the system and perform a proof-of-principle magnetic immunoassay, which is to the best of our knowledge, the first time that GMR sensors have been reported for an MRX bioassay. This work was published in Scientific Reports.

6.2 Areas for Future Work

Both the MFC project and MRX project presented in this dissertation can be further expanded upon in a few ways:

Regarding the MFC, its applications can be extended in the following directions: 1) B-cell malignancy diagnosis: B-cell lymphoma cells frequently shed off their cell membranes, forming the lymphoglandular bodies, which are used by cytologists as an indicator of lymphoid malignancy. Lymphoglandular bodies are essentially cell debris and they cannot be detected by currently available FCMs or ELISA which require specimen preparation or cell lysis, while MFC is expected to overcome this kind of restriction; 2) CTC detection: as the high throughput measurements have been proofed with our MFC, the CTC detection is expected to work with our technique and can be utilized on early cancer diagnosis; 3) Integration of magnetic sorting: as it can filter the specific cells with targeted biomarkers to perform the whole function like what commercial FCMs do.

While MRX is a relatively unexplored area, its potential development for next-generation biosensing is fascinating. Specifically: 1) Assay development: as the proof-of-concept bioassay has been done with biotin-streptavidin, the applications for other immunoassays are expected; 2) Signal dependence on temperature: as we investigated and discussed the effect of applied field, magnetization time, and coverage on MRX signal, temperature was an uncontrollable variable during measurements. To systematically elucidate the mechanism of time-domain MRX, a well-controlled temperature chamber should be built for further study; 3) Multiplex immunoassay: followed by elucidation of temperature effect, the well-established time-domain MRX is expected to perform multiplex assay by tethering MNPs with different characteristic times that locate in the different order of time window. 4) Realization of miniaturization: as the external field source is the biggest hindrance for portability of magnetic biosensors, the removal of Helmholtz coils can tremendously reduce the size of MRX devices. To achieve this, a couple of strategies can be applied. The first one is using on-chip integrated wires, but heating issues might emerge. The second one is utilizing self-field from bias current through sensors, and the electron scattering within nano thin film would be the next challenge. The third one is integrating RF-coils and in-plane coils, heating is expected to be less and it can be extended to frequency domain such as Brownian relaxation, NMR, and even hyperthermia (for on-chip mechanical cell lysis). Conclusively, there’s plenty of room at the bottom as the applications of time-domain MRX have not been totally unveiled.

APPENDIX A: ABBREVIATION LEXICON

Abbreviation	**Translation**
ADC	analog-to-digital converter
APTES	(3-Aminopropyl)triethoxysilane
BSA	bovine serum albumin
CDS	correlated double sampling
CMOS	complementary metal-oxide-semiconductor
CTC	circulating tumor cells
DMEM	Dulbecco's modified Eagle medium
DTW	dynamic time warping
ECL	enhanced chemiluminescence
EDMF	energy-detection matched filters
EGFR	epidermal growth factor receptor
ELISA	enzyme-linked-immunosorbent assays
ESR	nuclear magnetic resonance
FACS	fluorescence-activated cell sorting
FBS	fetal bovine serum
FCM	flow cytometer; flow cytometry
FET	field effect transistor
FFT	fast Fourier transform
FPGA	field programmable gate array
FSC	forward scatter
GAPDH	glyceraldehyde-3-phosphate dehydrogenase
GMR	giant magnetoresistive; giant magnetoresistance
LOD	limit of detection
MF	matched filtering
MFC	magnetic flow cytometer; magnetic flow cytometry
MFI	mean fluorescence intensity
MIA	magnetic immunoassay
MMI	mean magnetic intensity
MNP	magnetic nanoparticle
MR	magnetoresistive; magnetoresistance
MRX	magnetorelaxometry; magnetorelaxation
NCD	noncommunicable disease
NMR	nuclear magnetic resonance

OM	optical microscope
PAGE	polyacrylamide gel electrophoresis
PCB	printed circuit board
PDMS	poly(dimethylsiloxane)
PE	phycoerythrin
PEMF	previous-event matched filters
PoC	point-of-care
PTFE	poly(tetrafluoroethylene)
ROC	receiver operator characteristic
RIPA	radioimmunoprecipitation assay
SA-PE	streptavidin-phycoerythrin
SDS-PAGE	sodium dodecyl sulfate-polyacrylamide gel electrophoresis
SEM	scanning electron microscope
SMF	simulation-based matched filters
SNR	signal-to-noise ratio
SQUID	superconducting quantum interference device
SSC	side scatter
TIA	transimpedance amplifier
ToF	time-of-flight
WHO	World Health Organization

APPENDIX B: LIST OF SYMBOLS

Symbol	**Quantity/Translation/Definition**
A	Hamaker constant
$\boldsymbol{B}$	magnetic flux density
C_D	drag coefficient defined by the size and shape of MNP
C_F	integration capacitor
C_s	a dimensionless coefficient containing the magnetic viscosity and signal per particle on the sensor
C_t	a dimensionless coefficient containing the magnetic viscosity and signal per particle on the trench
f	frequency of the alternating magnetic field
f_B	Brownian frequency
$\boldsymbol{F_D}$	drag force
$\boldsymbol{F_{el}}$	electro-repulsive force
$\boldsymbol{F_G}$	gravity
$\boldsymbol{F_{lang}}$	Langevin force
$\boldsymbol{F_M}$	Magnetic force
$\boldsymbol{F_{VDW}}$	Van der Waals force
$\boldsymbol{g}$	gravitational acceleration
H_0	stray field generated by MNPs at the time when turning off the external field
$\boldsymbol{H_A}$	applied field
$\boldsymbol{H_s}$	average field that works on the free layer
I	input current
K	anisotropy constant of MNPs
k_B	Boltzmann's constant
k_s	the stripe coverage in terms of percentage
k_t	the trench coverage in terms of percentage
l	sensor length
M_N	magnetization of the MNPs due to Néel relaxation
M_B	magnetization of the MNPs due to Brownian relaxation
M_0	magnetization of the MNPs at the time when turning off the external magnetic field
$\boldsymbol{r}$	distance between the MNP and the point of free layer
R_0	nominal resistance

R_p	MNP radius
S_0	sensitivity defined as $\partial R/\partial H$ (Ω/Oe)
t	time after turning off the field
T	Kelvin temperature
t_c	characteristic time of Néel relaxation
th	free layer thickness
t_{mag}	magnetization time
V_{bias}	bias voltage
V_c	core volume of an MNP
V_h	hydrodynamic volume of the MNP or magnetic bead
$\boldsymbol{v_m}$	medium velocity
$\boldsymbol{v_p}$	MNP's velocity
V_p	MNP's volume
w	sensor width
$\boldsymbol{x}$	in-plane axes
$\boldsymbol{y}$	in-plane axes
$\boldsymbol{z}$	out-of-plane axis
α	a constant related to the magnetic viscosity
ΔR	MR signal due to the MNP
ΔV_B	voltage variation of the MNPs due to Brownian relaxation
ΔV_N	voltage variation of the MNPs due to Néel relaxation
ΔV_{out}	extracted voltage
ε_0	permittivity of free space
ε_r	relative permittivity
η	dynamic viscosity of the liquid
κ	surface coverage
λ	Debye–Hückel length
ρ_m	density of the medium
ρ_p	density of the MNP
τ_0	attempt time (usually approximated as 10^{-9} sec)
τ_B	Brownian relaxation time
τ_{eff}	effective relaxation time
τ_N	Néel relaxation time
χ	volume susceptibility (dimensionless)
χ_0	DC susceptibility
χ_c	complex susceptibility
χ_m	volume susceptibility of medium

χ'	in-phase susceptibility
χ''	out-of-phase susceptibility
χ_∞	susceptibility at high frequency
ψ_p	surface potential of the MNP
ψ_s	surface potential of the sensor substrate

BIBLIOGRAPHY

(1) March 29; 2016. Transforming health: Shifting from reactive to proactive and predictive care https://www.marsdd.com/news/transforming-health-shifting-from-reactive-to-proactive-and-predictive-care/ (accessed Dec 2, 2019).

(2) United Nations; Department of Economics and Social Affairs; Population Division. *World Population Ageing, 2017 Highlights*; 2017.

(3) Kwon, L.; Long, K. D.; Wan, Y.; Yu, H.; Cunningham, B. T. Medical Diagnostics with Mobile Devices: Comparison of Intrinsic and Extrinsic Sensing. *Biotechnol. Adv.* **2016**, *34* (3), 291–304. https://doi.org/10.1016/j.biotechadv.2016.02.010.

(4) Zhu, H.; O. Isikman, S.; Mudanyali, O.; Greenbaum, A.; Ozcan, A. Optical Imaging Techniques for Point-of-Care Diagnostics. *Lab. Chip* **2013**, *13* (1), 51–67. https://doi.org/10.1039/C2LC40864C.

(5) Afsahi, S.; Lerner, M. B.; Goldstein, J. M.; Lee, J.; Tang, X.; Bagarozzi, D. A.; Pan, D.; Locascio, L.; Walker, A.; Barron, F.; Goldsmith, B. R. Novel Graphene-Based Biosensor for Early Detection of Zika Virus Infection. *Biosens. Bioelectron.* **2018**, *100*, 85–88. https://doi.org/10.1016/j.bios.2017.08.051.

(6) Wang, Y.-L.; Huang, C.-C.; Kang, Y.-W. Incorporation of Ligand–Receptor Binding-Site Models and Transistor-Based Sensors for Resolving Dissociation Constants and Number of Binding Sites. *IET Nanobiotechnol.* **2014**, *8* (1), 10–17. https://doi.org/10.1049/iet-nbt.2013.0031.

(7) Huang, C.-C.; Lee, G.-Y.; Chyi, J.-I.; Cheng, H.-T.; Hsu, C.-P.; Hsu, Y.-R.; Hsu, C.-H.; Huang, Y.-F.; Sun, Y.-C.; Chen, C.-C.; Li, S.-S.; Andrew Yeh, J.; Yao, D.-J.; Ren, F.; Wang, Y.-L. AlGaN/GaN High Electron Mobility Transistors for Protein–Peptide Binding Affinity Study. *Biosens. Bioelectron.* **2013**, *41*, 717–722. https://doi.org/10.1016/j.bios.2012.09.066.

(8) Aronoff-Spencer, E.; Venkatesh, A. G.; Sun, A.; Brickner, H.; Looney, D.; Hall, D. A. Detection of Hepatitis C Core Antibody by Dual-Affinity Yeast Chimera and Smartphone-Based Electrochemical Sensing. *Biosens. Bioelectron.* **2016**, *86*, 690–696. https://doi.org/10.1016/j.bios.2016.07.023.

(9) Jiang, H.; Sun, A.; Venkatesh, A. G.; Hall, D. A. An Audio Jack-Based Electrochemical Impedance Spectroscopy Sensor for Point-of-Care Diagnostics. *IEEE Sens. J.* **2017**, *17* (3), 589–597. https://doi.org/10.1109/JSEN.2016.2634530.

(10) Jiang, H.; Zhou, X.; Kulkarni, S.; Uranian, M.; Seenivasan, R.; Hall, D. A. A Sub-1 MW Multiparameter Injectable BioMote for Continuous Alcohol Monitoring. In *2018 IEEE Custom Integrated Circuits Conference (CICC)*; 2018; pp 1–4. https://doi.org/10.1109/CICC.2018.8357045.

(11) Huang, C.-C.; Zhou, X.; Hall, D. A. Giant Magnetoresistive Biosensors for Time-Domain Magnetorelaxometry: A Theoretical Investigation and Progress Toward an Immunoassay. *Sci. Rep.* **2017**, *7*, srep45493. https://doi.org/10.1038/srep45493.

(12) Huang, C.-C.; Zhou, X.; Ying, D.; Hall, D. A. A GMR-Based Magnetic Flow Cytometer Using Matched Filtering. In *2017 IEEE SENSORS*; 2017; pp 1–3. https://doi.org/10.1109/ICSENS.2017.8233892.

(13) Zhou, X.; Sveiven, M.; Hall, D. A. A CMOS Magnetoresistive Sensor Front-End With Mismatch-Tolerance and Sub-Ppm Sensitivity for Magnetic Immunoassays. *IEEE Trans. Biomed. Circuits Syst.* **2019**, *13* (6), 1254–1263. https://doi.org/10.1109/TBCAS.2019.2949725.

(14) Zhou, X.; Sveiven, M.; Hall, D. A. 11.4 A Fast-Readout Mismatch-Insensitive Magnetoresistive Biosensor Front-End Achieving Sub-Ppm Sensitivity. In *2019 IEEE International Solid- State Circuits Conference - (ISSCC)*; 2019; pp 196–198. https://doi.org/10.1109/ISSCC.2019.8662440.

(15) Zhou, X.; Huang, C.; Hall, D. A. Giant Magnetoresistive Biosensor Array for Detecting Magnetorelaxation. *IEEE Trans. Biomed. Circuits Syst.* **2017**, *11* (4), 755–764. https://doi.org/10.1109/TBCAS.2017.2682080.

(16) Zhou, X.; Huang, C.-C.; Hall, D. A. Magnetoresistive Biosensors for Quantitative Proteomics. In *Biosensing and Nanomedicine X*; International Society for Optics and Photonics, 2017; Vol. 10352, p 103520F. https://doi.org/10.1117/12.2276933.

(17) Adem, S.; Jain, S.; Sveiven, M.; Zhou, X.; O'Donoghue, A. J.; Hall, D. A. Giant Magnetoresistive Biosensors for Real-Time Quantitative Detection of Protease Activity. *Sci. Rep.* **2020**, *10* (1), 7941. https://doi.org/10.1038/s41598-020-62910-2.

(18) Vashist, S. K.; Luppa, P. B.; Yeo, L. Y.; Ozcan, A.; Luong, J. H. T. Emerging Technologies for Next-Generation Point-of-Care Testing. *Trends Biotechnol.* **2015**, *33* (11), 692–705. https://doi.org/10.1016/j.tibtech.2015.09.001.

(19) Zhu, H.; Mavandadi, S.; Coskun, A. F.; Yaglidere, O.; Ozcan, A. Optofluidic Fluorescent Imaging Cytometry on a Cell Phone. *Anal. Chem.* **2011**, *83* (17), 6641–6647. https://doi.org/10.1021/ac201587a.

(20) Fernandes, E.; Martins, V. C.; Nóbrega, C.; Carvalho, C. M.; Cardoso, F. A.; Cardoso, S.; Dias, J.; Deng, D.; Kluskens, L. D.; Freitas, P. P.; Azeredo, J. A Bacteriophage Detection Tool for Viability Assessment of Salmonella Cells. *Biosens. Bioelectron.* **2014**, *52*, 239–246. https://doi.org/10.1016/j.bios.2013.08.053.

(21) Freitas, P. P.; Cardoso, F. A.; Martins, V. C.; Martins, S. a. M.; Loureiro, J.; Amaral, J.; Chaves, R. C.; Cardoso, S.; Fonseca, L. P.; Sebastião, A. M.; Pannetier-Lecoeur, M.; Fermon, C. Spintronic Platforms for Biomedical Applications. *Lab. Chip* **2012**, *12* (3), 546–557. https://doi.org/10.1039/C1LC20791A.

(22) Gaster, R. S.; Hall, D. A.; Nielsen, C. H.; Osterfeld, S. J.; Yu, H.; Mach, K. E.; Wilson, R. J.; Murmann, B.; Liao, J. C.; Gambhir, S. S.; Wang, S. X. Matrix-Insensitive Protein Assays Push the Limits of Biosensors in Medicine. *Nat. Med.* **2009**, *15* (11), 1327–1332. https://doi.org/10.1038/nm.2032.

(23) Osterfeld, S. J.; Yu, H.; Gaster, R. S.; Caramuta, S.; Xu, L.; Han, S.-J.; Hall, D. A.; Wilson, R. J.; Sun, S.; White, R. L.; Davis, R. W.; Pourmand, N.; Wang, S. X. Multiplex Protein Assays Based on Real-Time Magnetic Nanotag Sensing. *Proc. Natl. Acad. Sci.* **2008**, *105* (52), 20637–20640. https://doi.org/10.1073/pnas.0810822105.

(24) Wang, Y.; Wang, W.; Yu, L.; Tu, L.; Feng, Y.; Klein, T.; Wang, J.-P. Giant Magnetoresistive-Based Biosensing Probe Station System for Multiplex Protein Assays. *Biosens. Bioelectron.* **2015**, *70*, 61–68. https://doi.org/10.1016/j.bios.2015.03.011.

(25) Hall, D. A.; Gaster, R. S.; Lin, T.; Osterfeld, S. J.; Han, S.; Murmann, B.; Wang, S. X. GMR Biosensor Arrays: A System Perspective. *Biosens. Bioelectron.* **2010**, *25* (9), 2051–2057. https://doi.org/10.1016/j.bios.2010.01.038.

(26) Hall, D. A.; Gaster, R. S.; Osterfeld, S. J.; Murmann, B.; Wang, S. X. GMR Biosensor Arrays: Correction Techniques for Reproducibility and Enhanced Sensitivity. *Biosens. Bioelectron.* **2010**, *25* (9), 2177–2181. https://doi.org/10.1016/j.bios.2010.01.039.

(27) Wang, W.; Wang, Y.; Tu, L.; Feng, Y.; Klein, T.; Wang, J.-P. Magnetoresistive Performance and Comparison of Supermagnetic Nanoparticles on Giant Magnetoresistive Sensor-Based Detection System. *Sci. Rep.* **2014**, *4*. https://doi.org/10.1038/srep05716.

(28) Baselt, D. R.; Lee, G. U.; Natesan, M.; Metzger, S. W.; Sheehan, P. E.; Colton, R. J. A Biosensor Based on Magnetoresistance Technology. *Biosens. Bioelectron.* **1998**, *13* (7–8), 731–739. https://doi.org/10.1016/S0956-5663(98)00037-2.

(29) Schotter, J.; Kamp, P. B.; Becker, A.; Pühler, A.; Reiss, G.; Brückl, H. Comparison of a Prototype Magnetoresistive Biosensor to Standard Fluorescent DNA Detection. *Biosens. Bioelectron.* **2004**, *19* (10), 1149–1156. https://doi.org/10.1016/j.bios.2003.11.007.

(30) Shoshi, A.; Schotter, J.; Schroeder, P.; Milnera, M.; Ertl, P.; Charwat, V.; Purtscher, M.; Heer, R.; Eggeling, M.; Reiss, G.; Brueckl, H. Magnetoresistive-Based Real-Time Cell Phagocytosis Monitoring. *Biosens. Bioelectron.* **2012**, *36* (1), 116–122. https://doi.org/10.1016/j.bios.2012.04.002.

(31) Shen, W.; Liu, X.; Mazumdar, D.; Xiao, G. In Situ Detection of Single Micron-Sized Magnetic Beads Using Magnetic Tunnel Junction Sensors. *Appl. Phys. Lett.* **2005**, *86* (25), 253901. https://doi.org/10.1063/1.1952582.

(32) Shen, W.; Schrag, B. D.; Carter, M. J.; Xiao, G. Quantitative Detection of DNA Labeled with Magnetic Nanoparticles Using Arrays of MgO-Based Magnetic Tunnel Junction Sensors. *Appl. Phys. Lett.* **2008**, *93* (3), 033903. https://doi.org/10.1063/1.2963970.

(33) Koets, M.; van der Wijk, T.; van Eemeren, J. T. W. M.; van Amerongen, A.; Prins, M. W. J. Rapid DNA Multi-Analyte Immunoassay on a Magneto-Resistance Biosensor. *Biosens. Bioelectron.* **2009**, *24* (7), 1893–1898. https://doi.org/10.1016/j.bios.2008.09.023.

(34) Rizzi, G.; Westergaard Østerberg, F.; Dufva, M.; Fougt Hansen, M. Magnetoresistive Sensor for Real-Time Single Nucleotide Polymorphism Genotyping. *Biosens. Bioelectron.* **2014**, *52*, 445–451. https://doi.org/10.1016/j.bios.2013.09.026.

(35) Reisbeck, M.; Helou, M. J.; Richter, L.; Kappes, B.; Friedrich, O.; Hayden, O. Magnetic Fingerprints of Rolling Cells for Quantitative Flow Cytometry in Whole Blood. *Sci. Rep.* **2016**, *6*, 32838. https://doi.org/10.1038/srep32838.

(36) Liu, P.; Skucha, K.; Megens, M.; Boser, B. A CMOS Hall-Effect Sensor for the Characterization and Detection of Magnetic Nanoparticles for Biomedical Applications. *IEEE Trans. Magn.* **2011**, *47* (10), 3449–3451. https://doi.org/10.1109/TMAG.2011.2158600.

(37) Skucha, K.; Gambini, S.; Liu, P.; Megens, M.; Kim, J.; Boser, B. E. Design Considerations for CMOS-Integrated Hall-Effect Magnetic Bead Detectors for Biosensor Applications. *J. Microelectromechanical Syst.* **2013**, *22* (6), 1327–1338. https://doi.org/10.1109/JMEMS.2013.2259615.

(38) Kötitz, R.; Fannin, P. C.; Trahms, L. Time Domain Study of Brownian and Néel Relaxation in Ferrofluids. *J. Magn. Magn. Mater.* **1995**, *149* (1–2), 42–46. https://doi.org/10.1016/0304-8853(95)00333-9.

(39) Wang, H.; Chen, Y.; Hassibi, A.; Scherer, A.; Hajimiri, A. A Frequency-Shift CMOS Magnetic Biosensor Array with Single-Bead Sensitivity and No External Magnet; 2009; pp 438-439,439a. https://doi.org/10.1109/ISSCC.2009.4977496.

(40) Ludwig, F.; Mäuselein, S.; Heim, E.; Schilling, M. Magnetorelaxometry of Magnetic Nanoparticles in Magnetically Unshielded Environment Utilizing a Differential Fluxgate Arrangement. *Rev. Sci. Instrum.* **2005**, *76* (10), 106102. https://doi.org/10.1063/1.2069776.

(41) Miller, M. M.; Prinz, G. A.; Cheng, S.-F.; Bounnak, S. Detection of a Micron-Sized Magnetic Sphere Using a Ring-Shaped Anisotropic Magnetoresistance-Based Sensor: A Model for a Magnetoresistance-Based Biosensor. *Appl. Phys. Lett.* **2002**, *81* (12), 2211–2213. https://doi.org/10.1063/1.1507832.

(42) Besse, P.-A.; Boero, G.; Demierre, M.; Pott, V.; Popovic, R. Detection of a Single Magnetic Microbead Using a Miniaturized Silicon Hall Sensor. *Appl. Phys. Lett.* **2002**, *80* (22), 4199–4201. https://doi.org/10.1063/1.1483909.

(43) Graham, D. L.; Ferreira, H.; Bernardo, J.; Freitas, P. P.; Cabral, J. M. S. Single Magnetic Microsphere Placement and Detection On-Chip Using Current Line Designs with Integrated Spin Valve Sensors: Biotechnological Applications. *J. Appl. Phys.* **2002**, *91* (10), 7786–7788. https://doi.org/10.1063/1.1451898.

(44) Helou, M.; Reisbeck, M.; Tedde, S. F.; Richter, L.; Bär, L.; Bosch, J. J.; Stauber, R. H.; Quandt, E.; Hayden, O. Time-of-Flight Magnetic Flow Cytometry in Whole Blood with Integrated Sample Preparation. *Lab Chip* **2013**, *13* (6), 1035–1038. https://doi.org/10.1039/C3LC41310A.

(45) Issadore, D.; Chung, J.; Shao, H.; Liong, M.; Ghazani, A. A.; Castro, C. M.; Weissleder, R.; Lee, H. Ultrasensitive Clinical Enumeration of Rare Cells Ex Vivo Using a Micro-Hall Detector. *Sci. Transl. Med.* **2012**, *4* (141), 141ra92-141ra92. https://doi.org/10.1126/scitranslmed.3003747.

(46) Lin, G.; Karnaushenko, D. D.; Bermúdez, G. S. C.; Schmidt, O. G.; Makarov, D. Magnetic Suspension Array Technology: Controlled Synthesis and Screening in Microfluidic Networks. *Small* **2016**, *12* (33), 4553–4562. https://doi.org/10.1002/smll.201601166.

(47) Loureiro, J.; Andrade, P. Z.; Cardoso, S.; Silva, C. L. da; Cabral, J. M.; Freitas, P. P. Magnetoresistive Chip Cytometer. *Lab Chip* **2011**, *11* (13), 2255–2261. https://doi.org/10.1039/C0LC00324G.

(48) Murali, P.; Niknejad, A. M.; Boser, B. E. CMOS Microflow Cytometer for Magnetic Label Detection and Classification. *IEEE J. Solid-State Circuits* **2016**, *PP* (99), 1–13. https://doi.org/10.1109/JSSC.2016.2621036.

(49) Reisbeck, M.; Richter, L.; Helou, M. J.; Arlinghaus, S.; Anton, B.; van Dommelen, I.; Nitzsche, M.; Baßler, M.; Kappes, B.; Friedrich, O.; Hayden, O. Hybrid Integration of Scalable Mechanical and Magnetophoretic Focusing for Magnetic Flow Cytometry. *Biosens. Bioelectron.* **2018**, *109*, 98–108. https://doi.org/10.1016/j.bios.2018.02.046.

(50) Tang, H.; Venkatesh, S.; Lin, Z.; Lu, X.; Saeidi, H.; Rather, G. M.; Bertino, J. R.; Lin, C.; Javanmard, M.; Sengupta, K. 2D Magnetic Sensor Array for Real-Time Cell Tracking and Multi-Site Detection with Increased Robustness and Flow-Rate. In *2019 IEEE Custom Integrated Circuits Conference (CICC)*; 2019; pp 1–4. https://doi.org/10.1109/CICC.2019.8780363.

(51) Fernandes, A. C.; Duarte, C. M.; Cardoso, F. A.; Bexiga, R.; Cardoso, S.; Freitas, P. P. Lab-on-Chip Cytometry Based on Magnetoresistive Sensors for Bacteria Detection in Milk. *Sensors* **2014**, *14* (8), 15496–15524. https://doi.org/10.3390/s140815496.

(52) Lin, G.; Makarov, D.; Melzer, M.; Si, W.; Yan, C.; Schmidt, O. G. A Highly Flexible and Compact Magnetoresistive Analytic Device. *Lab Chip* **2014**, *14* (20), 4050–4058. https://doi.org/10.1039/C4LC00751D.

(53) Lin, G.; Makarov, D.; Medina-Sánchez, M.; Guix, M.; Baraban, L.; Cuniberti, G.; Schmidt, O. G. Magnetofluidic Platform for Multidimensional Magnetic and Optical Barcoding of Droplets. *Lab Chip* **2014**, *15* (1), 216–224. https://doi.org/10.1039/C4LC01160K.

(54) Vila, A.; Martins, V. C.; Chícharo, A.; Rodriguez-Abreu, C.; Fernandes, A. C.; Cardoso, F. A.; Cardoso, S.; Rivas, J.; Freitas, P. Customized Design of Magnetic Beads for Dynamic Magnetoresistive Cytometry. *IEEE Trans. Magn.* **2014**, *50* (11), 1–4. https://doi.org/10.1109/TMAG.2014.2324411.

(55) Wang, S. X.; Li, G. Advances in Giant Magnetoresistance Biosensors With Magnetic Nanoparticle Tags: Review and Outlook. *IEEE Trans. Magn.* **2008**, *44* (7), 1687–1702. https://doi.org/10.1109/TMAG.2008.920962.

(56) Loureiro, J.; Fermon, C.; Pannetier-Lecoeur, M.; Arrias, G.; Ferreira, R.; Cardoso, S.; Freitas, P. P. Magnetoresistive Detection of Magnetic Beads Flowing at High Speed in Microfluidic Channels. *IEEE Trans. Magn.* **2009**, *45* (10), 4873–4876. https://doi.org/10.1109/TMAG.2009.2026287.

(57) Hall, D. A. GMR Spin-Valve Biochips and Interface Electronics for Ultrasensitive in-Vitro Diagnostics. PhD Thesis, Stanford University, 2011.

(58) Guanxiong Li; Wang, S. X. Analytical and Micromagnetic Modeling for Detection of a Single Magnetic Microbead or Nanobead by Spin Valve Sensors. *IEEE Trans. Magn.* **2003**, *39* (5), 3313–3315. https://doi.org/10.1109/TMAG.2003.816760.

(59) Debye, P. *Polar Molecules*; Chemical Catalog Company: New York, 1929.

(60) Néel, L. Théorie Du Traînage Magnétique Des Substances Massives Dans Le Domaine de Rayleigh. *J. Phys. Radium* **1950**, *11* (2), 49–61. https://doi.org/10.1051/jphysrad:0195000110204900.

(61) Brown, W. F. Thermal Fluctuations of a Single-Domain Particle. *Phys. Rev.* **1963**, *130* (5), 1677–1686. https://doi.org/10.1103/PhysRev.130.1677.

(62) Kötitz, R.; Weitschies, W.; Trahms, L.; Semmler, W. Investigation of Brownian and Néel Relaxation in Magnetic Fluids. *J. Magn. Magn. Mater.* **1999**, *201* (1–3), 102–104. https://doi.org/10.1016/S0304-8853(99)00065-7.

(63) Chantrell, R. W.; Hoon, S. R.; Tanner, B. K. Time-Dependent Magnetization in Fine-Particle Ferromagnetic Systems. *J. Magn. Magn. Mater.* **1983**, *38* (2), 133–141. https://doi.org/10.1016/0304-8853(83)90037-9.

(64) Østerberg, F. W.; Rizzi, G.; Zardán Gómez de la Torre, T.; Strömberg, M.; Strømme, M.; Svedlindh, P.; Hansen, M. F. Measurements of Brownian Relaxation of Magnetic Nanobeads Using Planar Hall Effect Bridge Sensors. *Biosens. Bioelectron.* **2013**, *40* (1), 147–152. https://doi.org/10.1016/j.bios.2012.07.002.

(65) Østerberg, F. W.; Rizzi, G.; Hansen, M. F. On-Chip Measurements of Brownian Relaxation vs. Concentration of 40 Nm Magnetic Beads. *J. Appl. Phys.* **2012**, *112* (12), 124512. https://doi.org/10.1063/1.4769796.

(66) Hung, T. Q.; Oh, S.; Jeong, J.-R.; Kim, C. Spin-Valve Planar Hall Sensor for Single Bead Detection. *Sens. Actuators Phys.* **2010**, *157* (1), 42–46. https://doi.org/10.1016/j.sna.2009.11.033.

(67) Tu, B. D.; Hung, T. Q.; Thanh, N. T.; Danh, T. M.; Duc, N. H.; Kim, C. Planar Hall Bead Array Counter Microchip with NiFe/IrMn Bilayers. *J. Appl. Phys.* **2008**, *104* (7), 074701. https://doi.org/10.1063/1.2988297.

(68) Jennings, C. D.; Foon, K. A. Recent Advances in Flow Cytometry: Application to the Diagnosis of Hematologic Malignancy. *Blood* **1997**, *90* (8), 2863–2892.

(69) Perfetto, S. P.; Chattopadhyay, P. K.; Roederer, M. Seventeen-Colour Flow Cytometry: Unravelling the Immune System. *Nat. Rev. Immunol.* **2004**, *4* (8), 648–655. https://doi.org/10.1038/nri1416.

(70) Malcovati, L.; Germing, U.; Kuendgen, A.; Della Porta, M. G.; Pascutto, C.; Invernizzi, R.; Giagounidis, A.; Hildebrandt, B.; Bernasconi, P.; Knipp, S.; Strupp, C.; Lazzarino, M.; Aul, C.; Cazzola, M. Time-Dependent Prognostic Scoring System for Predicting Survival and Leukemic Evolution in Myelodysplastic Syndromes. *J. Clin. Oncol.* **2007**, *25* (23), 3503–3510. https://doi.org/10.1200/JCO.2006.08.5696.

(71) Herzenberg, L. A.; Parks, D.; Sahaf, B.; Perez, O.; Roederer, M.; Herzenberg, L. A. The History and Future of the Fluorescence Activated Cell Sorter and Flow Cytometry: A View from Stanford. *Clin. Chem.* **2002**, *48* (10), 1819–1827.

(72) Loureiro, J.; Ferreira, R.; Cardoso, S.; Freitas, P. P.; Germano, J.; Fermon, C.; Arrias, G.; Pannetier-Lecoeur, M.; Rivadulla, F.; Rivas, J. Toward a Magnetoresistive Chip Cytometer: Integrated Detection of Magnetic Beads Flowing at Cm/s Velocities in Microfluidic Channels. *Appl. Phys. Lett.* **2009**, *95* (3), 034104. https://doi.org/10.1063/1.3182791.

(73) Gaster, R. S.; Xu, L.; Han, S.-J.; Wilson, R. J.; Hall, D. A.; Osterfeld, S. J.; Yu, H.; Wang, S. X. Quantification of Protein Interactions and Solution Transport Using High-Density GMR Sensor Arrays. *Nat. Nanotechnol.* **2011**, *6* (5), 314–320. https://doi.org/10.1038/nnano.2011.45.

(74) Begum, N.; Ulanova, L.; Wang, J.; Keogh, E. Accelerating Dynamic Time Warping Clustering with a Novel Admissible Pruning Strategy. In *Proceedings of the 21th ACM SIGKDD International Conference on Knowledge Discovery and Data Mining*;

KDD ’15; Association for Computing Machinery: Sydney, NSW, Australia, 2015; pp 49–58. https://doi.org/10.1145/2783258.2783286.

(75) Mueen, A.; Keogh, E. Extracting Optimal Performance from Dynamic Time Warping. In *Proceedings of the 22nd ACM SIGKDD International Conference on Knowledge Discovery and Data Mining*; KDD ’16; Association for Computing Machinery: San Francisco, California, USA, 2016; pp 2129–2130. https://doi.org/10.1145/2939672.2945383.

(76) Vullings, H. J. L. M.; Verhaegen, M. H. G.; Verbruggen, H. B. Automated ECG Segmentation with Dynamic Time Warping. In *Proceedings of the 20th Annual International Conference of the IEEE Engineering in Medicine and Biology Society. Vol.20 Biomedical Engineering Towards the Year 2000 and Beyond (Cat. No.98CH36286)*; 1998; pp 163–166 vol.1. https://doi.org/10.1109/IEMBS.1998.745863.

(77) De Palma, R.; Liu, C.; Barbagini, F.; Reekmans, G.; Bonroy, K.; Laureyn, W.; Borghs, G.; Maes, G. Magnetic Particles as Labels in Bioassays: Interactions between a Biotinylated Gold Substrate and Streptavidin Magnetic Particles. *J. Phys. Chem. C* **2007**, *111* (33), 12227–12235. https://doi.org/10.1021/jp0725681.

(78) Liu, C.; Stakenborg, T.; Peeters, S.; Lagae, L. Cell Manipulation with Magnetic Particles toward Microfluidic Cytometry. *J. Appl. Phys.* **2009**, *105* (10), 102014. https://doi.org/10.1063/1.3116091.

(79) Wirix-Speetjens, R.; Fyen, W.; Kaidong Xu; Jo De Boeck; Borghs, G. A Force Study of On-Chip Magnetic Particle Transport Based on Tapered Conductors. *IEEE Trans. Magn.* **2005**, *41* (10), 4128–4133. https://doi.org/10.1109/TMAG.2005.855345.

(80) Key Statistics for Pancreatic Cancer https://www.cancer.org/cancer/pancreatic-cancer/about/key-statistics.html (accessed May 5, 2020).

(81) Ray, P.; Cheek, M. A.; Sharaf, M. L.; Li, N.; Ellington, A. D.; Sullenger, B. A.; Shaw, B. R.; White, R. R. Aptamer-Mediated Delivery of Chemotherapy to Pancreatic Cancer Cells. *Nucleic Acid Ther.* **2012**, *22* (5), 295–305. https://doi.org/10.1089/nat.2012.0353.

(82) Baldrich, E.; Restrepo, A.; O’Sullivan, C. K. Aptasensor Development: Elucidation of Critical Parameters for Optimal Aptamer Performance. *Anal. Chem.* **2004**, *76* (23), 7053–7063. https://doi.org/10.1021/ac049258o.

(83) Cho, H.; Yeh, E.-C.; Sinha, R.; Laurence, T. A.; Bearinger, J. P.; Lee, L. P. Single-Step Nanoplasmonic VEGF165 Aptasensor for Early Cancer Diagnosis. *ACS Nano* **2012**, *6* (9), 7607–7614. https://doi.org/10.1021/nn203833d.

(84) Farokhzad, O. C.; Cheng, J.; Teply, B. A.; Sherifi, I.; Jon, S.; Kantoff, P. W.; Richie, J. P.; Langer, R. Targeted Nanoparticle-Aptamer Bioconjugates for Cancer

Chemotherapy in Vivo. *Proc. Natl. Acad. Sci.* **2006**, *103* (16), 6315–6320. https://doi.org/10.1073/pnas.0601755103.

(85) Iliuk, A. B.; Hu, L.; Tao, W. A. Aptamer in Bioanalytical Applications. *Anal. Chem.* **2011**, *83* (12), 4440–4452. https://doi.org/10.1021/ac201057w.

(86) Song, S.; Wang, L.; Li, J.; Fan, C.; Zhao, J. Aptamer-Based Biosensors. *TrAC Trends Anal. Chem.* **2008**, *27* (2), 108–117. https://doi.org/10.1016/j.trac.2007.12.004.

(87) Torres-Chavolla, E.; Alocilja, E. C. Aptasensors for Detection of Microbial and Viral Pathogens. *Biosens. Bioelectron.* **2009**, *24* (11), 3175–3182. https://doi.org/10.1016/j.bios.2008.11.010.

(88) Wang, W.; Chen, C.; Qian, M.; Zhao, X. S. Aptamer Biosensor for Protein Detection Using Gold Nanoparticles. *Anal. Biochem.* **2008**, *373* (2), 213–219. https://doi.org/10.1016/j.ab.2007.11.013.

(89) Willner, I.; Zayats, M. Electronic Aptamer-Based Sensors. *Angew. Chem. Int. Ed.* **2007**, *46* (34), 6408–6418. https://doi.org/10.1002/anie.200604524.

(90) Bompiani, K. M.; Monroe, D. M.; Church, F. C.; Sullenger, B. A. A High Affinity, Antidote-Controllable Prothrombin and Thrombin-Binding RNA Aptamer Inhibits Thrombin Generation and Thrombin Activity. *J. Thromb. Haemost.* **2012**, *10* (5), 870–880. https://doi.org/10.1111/j.1538-7836.2012.04679.x.

(91) Huang, C.-C.; Chan, M.; Zhou, X.; Hall, D. A. A Magnetic Flow Cytometer Using Matched Filtering. 18.

(92) Momen-Heravi, F.; Balaj, L.; Alian, S.; Trachtenberg, A. J.; Hochberg, F. H.; Skog, J.; Kuo, W. P. Impact of Biofluid Viscosity on Size and Sedimentation Efficiency of the Isolated Microvesicles. *Front. Physiol.* **2012**, *3*. https://doi.org/10.3389/fphys.2012.00162.

(93) Gilmour, A. M.; Abdulkhalek, S.; Cheng, T. S. W.; Alghamdi, F.; Jayanth, P.; O'Shea, L. K.; Geen, O.; Arvizu, L. A.; Szewczuk, M. R. A Novel Epidermal Growth Factor Receptor-Signaling Platform and Its Targeted Translation in Pancreatic Cancer. *Cell. Signal.* **2013**, *25* (12), 2587–2603. https://doi.org/10.1016/j.cellsig.2013.08.008.

(94) Magadala, P.; Amiji, M. Epidermal Growth Factor Receptor-Targeted Gelatin-Based Engineered Nanocarriers for DNA Delivery and Transfection in Human Pancreatic Cancer Cells. *AAPS J.* **2008**, *10* (4). https://doi.org/10.1208/s12248-008-9065-0.

(95) Olszewski-Hamilton, U.; Hamilton, G. Dependence of Relative Expression of NTR1 and EGFR on Cell Density and Extracellular PH in Human Pancreatic Cancer Cell Lines. *Cancers* **2011**, *3* (1), 182–197. https://doi.org/10.3390/cancers3010182.

(96) Ikeda, S.; Hayakawa, J.; Lee, Y. M.; Matsukura, F.; Ohno, Y.; Hanyu, T.; Ohno, H. Magnetic Tunnel Junctions for Spintronic Memories and Beyond. *IEEE Trans. Electron Devices* **2007**, *54* (5), 991–1002. https://doi.org/10.1109/TED.2007.894617.

(97) Denoual, M.; Saez, S.; Kauffman, F.; Dolabdjian, C. Magnetorelaxometry Using Improved Giant MagnetoResistance Magnetometer. *Sens. Actuators Phys.* **2010**, *159* (2), 184–188. https://doi.org/10.1016/j.sna.2010.03.029.

(98) Ahrentorp, F.; Astalan, A. P.; Jonasson, C.; Blomgren, J.; Qi, B.; Mefford, O. T.; Yan, M.; Courtois, J.; Berret, J.-F.; Fresnais, J.; Sandre, O.; Dutz, S.; Müller, R.; Johansson, C. Sensitive High Frequency AC Susceptometry in Magnetic Nanoparticle Applications; AIP Publishing, 2010; Vol. 1311, pp 213–223. https://doi.org/10.1063/1.3530015.

(99) Bryant, H. C.; Adolphi, N. L.; Huber, D. L.; Fegan, D. L.; Monson, T. C.; Tessier, T. E.; Flynn, E. R. Magnetic Properties of Nanoparticles Useful for SQUID Relaxometry in Biomedical Applications. *J. Magn. Magn. Mater.* **2011**, *323* (6), 767–774. https://doi.org/10.1016/j.jmmm.2010.10.042.

(100) Fonnum, G.; Johansson, C.; Molteberg, A.; Mørup, S.; Aksnes, E. Characterisation of Dynabeads® by Magnetization Measurements and Mössbauer Spectroscopy. *J. Magn. Magn. Mater.* **2005**, *293* (1), 41–47. https://doi.org/10.1016/j.jmmm.2005.01.041.

(101) Johnson, C.; Adolphi, N. L.; Butler, K. L.; Lovato, D. M.; Larson, R.; Schwindt, P. D. D.; Flynn, E. R. Magnetic Relaxometry with an Atomic Magnetometer and SQUID Sensors on Targeted Cancer Cells. *J. Magn. Magn. Mater.* **2012**, *324* (17), 2613–2619. https://doi.org/10.1016/j.jmmm.2012.03.015.

(102) Adolphi, N. L.; Huber, D. L.; Jaetao, J. E.; Bryant, H. C.; Lovato, D. M.; Fegan, D. L.; Venturini, E. L.; Monson, T. C.; Tessier, T. E.; Hathaway, H. J.; Bergemann, C.; Larson, R. S.; Flynn, E. R. Characterization of Magnetite Nanoparticles for SQUID-Relaxometry and Magnetic Needle Biopsy. *J. Magn. Magn. Mater.* **2009**, *321* (10), 1459–1464. https://doi.org/10.1016/j.jmmm.2009.02.067.

(103) Street, R.; Woolley, J. C. A Study of Magnetic Viscosity. *Proc. Phys. Soc. Sect. A* **1949**, *62* (9), 562–572. https://doi.org/10.1088/0370-1298/62/9/303.

(104) Wohlfarth, E. P. The Coefficient of Magnetic Viscosity. *J. Phys. F Met. Phys.* **1984**, *14* (8), L155. https://doi.org/10.1088/0305-4608/14/8/005.

(105) Berkov, D. V.; Kötitz, R. Irreversible Relaxation Behaviour of a General Class of Magnetic Systems. *J. Phys. Condens. Matter* **1996**, *8* (9), 1257–1266. https://doi.org/10.1088/0953-8984/8/9/016.

(106) Bechstein, D. J. B.; Lee, J.-R.; Ooi, C. C.; Gani, A. W.; Kim, K.; Wilson, R. J.; Wang, S. X. High Performance Wash-Free Magnetic Bioassays through

Microfluidically Enhanced Particle Specificity. *Sci. Rep.* **2015**, *5* (1), 1–11. https://doi.org/10.1038/srep11693.

(107) Lee, J.-R.; Sato, N.; Bechstein, D. J. B.; Osterfeld, S. J.; Wang, J.; Gani, A. W.; Hall, D. A.; Wang, S. X. Experimental and Theoretical Investigation of the Precise Transduction Mechanism in Giant Magnetoresistive Biosensors. *Sci. Rep.* **2016**, *6*, 18692. https://doi.org/10.1038/srep18692.

(108) Li, G.; Wang, S. X.; Sun, S. Model and Experiment of Detecting Multiple Magnetic Nanoparticles as Biomolecular Labels by Spin Valve Sensors. *IEEE Trans. Magn.* **2004**, *40* (4), 3000–3002. https://doi.org/10.1109/TMAG.2004.830626.

(109) Li, G.; Sun, S.; Wang, S. X. Spin Valve Biosensors: Signal Dependence on Nanoparticle Position. *J. Appl. Phys.* **2006**, *99* (8), 08P107. https://doi.org/10.1063/1.2170052.

(110) De Palma, R.; Peeters, S.; Van Bael, M. J.; Van den Rul, H.; Bonroy, K.; Laureyn, W.; Mullens, J.; Borghs, G.; Maes, G. Silane Ligand Exchange to Make Hydrophobic Superparamagnetic Nanoparticles Water-Dispersible. *Chem. Mater.* **2007**, *19* (7), 1821–1831. https://doi.org/10.1021/cm0628000.

(111) Bloembergen, N.; Purcell, E. M.; Pound, R. V. Relaxation Effects in Nuclear Magnetic Resonance Absorption. *Phys. Rev.* **1948**, *73* (7), 679–712. https://doi.org/10.1103/PhysRev.73.679.

(112) Perez, J. M.; Josephson, L.; O'Loughlin, T.; Högemann, D.; Weissleder, R. Magnetic Relaxation Switches Capable of Sensing Molecular Interactions. *Nat. Biotechnol.* **2002**, *20* (8), 816–820. https://doi.org/10.1038/nbt720.

(113) Lee, H.; Sun, E.; Ham, D.; Weissleder, R. Chip–NMR Biosensor for Detection and Molecular Analysis of Cells. *Nat. Med.* **2008**, *14* (8), 869–874. https://doi.org/10.1038/nm.1711.

(114) Sun, N.; Liu, Y.; Lee, H.; Weissleder, R.; Ham, D. CMOS RF Biosensor Utilizing Nuclear Magnetic Resonance. *IEEE J. Solid-State Circuits* **2009**, *44* (5), 1629–1643. https://doi.org/10.1109/JSSC.2009.2017007.

(115) Lei, K. M.; Heidari, H.; Mak, P. I.; Law, M. K.; Maloberti, F.; Martins, R. P. A Handheld High-Sensitivity Micro-NMR CMOS Platform With B-Field Stabilization for Multi-Type Biological/Chemical Assays. *IEEE J. Solid-State Circuits* **2016**, *PP* (99), 1–14. https://doi.org/10.1109/JSSC.2016.2591551.

(116) Sun, N.; Yoon, T. J.; Lee, H.; Andress, W.; Weissleder, R.; Ham, D. Palm NMR and 1-Chip NMR. *IEEE J. Solid-State Circuits* **2011**, *46* (1), 342–352. https://doi.org/10.1109/JSSC.2010.2074630.

(117) Gandhi, S.; Arami, H.; Krishnan, K. M. Detection of Cancer-Specific Proteases Using Magnetic Relaxation of Peptide-Conjugated Nanoparticles in Biological

Environment. *Nano Lett.* **2016**, *16* (6), 3668–3674. https://doi.org/10.1021/acs.nanolett.6b00867.

(118) Sideris, C.; Hajimiri, A. Design and Implementation of an Integrated Magnetic Spectrometer for Multiplexed Biosensing. *IEEE Trans. Biomed. Circuits Syst.* **2013**, *7* (6), 773–784. https://doi.org/10.1109/TBCAS.2013.2297514.

(119) Liu, P. P.; Skucha, K.; Duan, Y.; Megens, M.; Kim, J.; Izyumin, I. I.; Gambini, S.; Boser, B. Magnetic Relaxation Detector for Microbead Labels. *IEEE J. Solid-State Circuits* **2012**, *47* (4), 1056–1064. https://doi.org/10.1109/JSSC.2012.2185339.

(120) Gambini, S.; Skucha, K.; Liu, P. P.; Kim, J.; Krigel, R. A 10 KPixel CMOS Hall Sensor Array With Baseline Suppression and Parallel Readout for Immunoassays. *IEEE J. Solid-State Circuits* **2013**, *48* (1), 302–317. https://doi.org/10.1109/JSSC.2012.2224531.